The Role of Collagen Cross-linking in Craniofacial and Long Bone Mineralization and Healing

by

Genevieve E. Romanowicz

A dissertation submitted in partial fulfillment
of the requirements for the degree of
Doctor of Philosophy
(Oral Health Sciences)
in the University of Michigan
2021

Doctoral Committee:

Professor David H. Kohn, Chair
Professor Karl Jepsen
Professor Yuji Mishina
Professor James Simmer

Genevieve E. Romanowicz

geromano@umich.edu

ORCID iD: 0000-0002-4483-7895

Dedication

To Karl, KJ and Jim Jam.

Acknowledgements

It has been a long road, but I have many who have helped me along the way. Thank you to my advisor, David Kohn, for your unwavering support and constant push to do my best, think independently, challenge the status quo, and to ensure I always do a power analysis. Your many "Dave-isms" will follow me as I move on in my career and I am sure I will be better for it. I would like to thank my committee members, Karl Jepsen, Yuji Mishina, and James Simmer for sharing your lab spaces, equipment, thoughtful guidance, and willingness to always write a letter of support when needed. I would also like to thank and acknowledge my funding sources – National Institute of Health, Rackham Graduate School and the School of Dentistry, University of Michigan.

Thank you to Ken Kozloff for sharing the nanoindenter with me and Hsiao Sung for surgery training. I could not have done the bulk of this work without your support. Thank you to Gurjit Mandair for the guidance with the Raman spectroscopy. Numerous core personnel have been essential to my work: Wendy Feng (Natural Products Core), Chris Strayhorn (UMSOD Histology Core), and last but not least, Michelle Lynch (UMSOD MicroCT Core). Michelle not only provided numerous guidance on work, but also some great laughs and friendship along the way.

Thank you to the Kohn Lab (past and present) – Erin McNerny, Janani Ramaswamy, Harsha Ramaraju, Joe Gardinier, Michael Friedman, Gurjit Mandair, Morgan Bolger, Sam McGoldrick, Merjem Mededovic, Eric Madsen, Tom Davidson, Lizhong Zhang, Ben Bielajew, Aidan Terhune, and Ben Sexton. You helped make every aspect (good or bad) enjoyable by being willing to help, listen, laugh, bring baked goods, play Sporcle Trivia, etc. You were there every step of the way in dealing with the chaos of COVID, the lab move, and always listened to me complain. A special thank you to Morgan who always was a sounding board and helped me to figure out some of the worst sticking points in much of the technique development as well as endured days of mouse surgeries. I could not have asked for a better lab group!

Thank you to all those in the Office of Research (Kimberly Smith, Amy Watson, Pat Schultz and Manette London), Biological and Materials Science and Prosthodontics (Erin Semmens, Kerry Boyd, Deb Keedy, and Joel Clendenin), and Grants and Contracts (Janet Sloan) who have helped make the logistics of life so much easier. And a special thank you to Kimberly who has been a mom-figure and friend along the way. Thank you to Jan Hu and Vesa Kaartinen for guidance as program directors or whenever I needed assistance on my F30 or award applications and for all your advice over time. Even if it was "no one will read your dissertation, so make it short" (Vesa). As for dental school training, I have too many people to thank for helping me to make it through it all. I would especially like to thank Ann Somppi and Mark Snyder for your friendship, guidance, and support during my clinical training as well as for your understanding as I pursued my dream, albeit different than what you are used to. You made many accommodations and always made me smile along the way. You will always be the best part of my memories of 3Blue.

Thank you to the many friends I made along the way. I was lucky enough to have several endure a similar amount of time including Yasmine Doleyres and Ke'ale Louie. While times were tough, I am glad I was able to share them with you both. Your current success and happiness now give me hope for life after graduate school. Thank you to all the OHS Buddies, past and present, who were a major support system through everything.

Most of all, I need to thank my family. I could not be doing what I am doing without their unwavering love and support. To my parents, John and Lynn Gierke, who raised me to be curious and independent and supported me with many trips to help out. To my in-laws, Karl and Marie Romanowicz, who never failed to make a trip to visit or help at home while I was away at a conference. And thank you to all for being amazing grandparents and taking the boys for fun vacations every summer so that we could get work done. Thank you to our two boys, Karl and James, for understanding that mommy "will always be in school" and being very patient to get your vacation to the ocean (which we will do, as promised). And mostly, thank you my husband, Karl, for being supportive from the beginning. Including taking the chance on coming here, taking a chance on our next moves, and putting up with the chaos of raising two kids while both pursuing a PhD. I couldn't ask for anyone better at my side and can't wait to see where life takes us next.

Table of Contents

Dedication ii

Acknowledgements iii

List of Tables x

List of Figures xi

Abstract xiii

Chapter 1. Advancements in Composition and Structural Characterization of Bone to Inform Mechanical Outcomes and Modelling 1

1.1 Introduction 1

1.2 Whole Bone Level 2

1.3 Structure & Geometry 3

1.3.1 Porosity 3

1.3.2 Osteocytes and the Lacuna-Canalicular Network 3

1.4 Composition 4

1.4.1 Enzymatic Cross-Links 5

1.4.2 Non-Enzymatic Cross-Links & Advanced Glycation End Products (AGEs) 6

1.4.3 Mineral 7

1.5 Genetic Manipulations of Bone Composition and Structure 8

1.6 Summary 9

1.7 Acknowledgements 10

1.8 References 13

Chapter 2. Hypothesis, Study Aims and Organization of Dissertation 19

2.1 Study Rationale 19

2.2 Hypothesis and Aims 20

2.2.1 Global Hypothesis: 20

2.2.2 Hypothesis 1: 20

2.2.3 Hypothesis 2: 20

2.2.4 Hypothesis 3: 21

2.3 Summary and Organization of Dissertation 22

2.4 References 23

Chapter 3. Collagen Cross-link Profiles Differ Between Craniofacial and Long Bones Driving Altered Mineralization Response to Perturbed Collagen 25

3.1 Introduction 25

3.2 Methods 27

3.2.1 Animals 27

3.2.2 MicroCT 27

3.2.3 Collagen Cross-link Analysis 28

3.2.4 Histomorphometry 29

3.2.5 Raman Spectroscopy 30

3.2.6 Nanoindentation 30

3.2.7 Statistics 31

3.3 Results 31

3.3.1 Mineral Apposition Rate and Total Mineral Density (TMD) are Anatomical Site-dependent 31

3.3.2 Tissue Level Young's Modulus and Hardness Were Higher Mandible as Compared to the Femur but Were Not Altered by BAPN Treatment 33

3.3.3 Collagen Cross-links Differ Between the Mandible and Femur and are Altered Differently with BAPN Treatment 33

3.3.4 BAPN Causes Mineral Differences in the Femur and Matrix Differences in the Mandible 34

3.4 Discussion 35

3.5 Conclusions 38

3.6 Acknowledgements 39

3.7 Author Contributions 39

3.8 References 48

Chapter 4. Sub-critical Defect Healing is Anatomical Site-Dependent as Well as Cellular and Mechanical Response to Beta-aminopropionitrile 52

4.1 Introduction 52

4.2 Methods 53

4.2.1 Animals 53

4.2.2 MicroCT 54

4.2.3 Histomorphometry and Immunohistochemistry 54

4.2.4 Nanoindentation 56

4.2.5 Statistics 56

4.3 Results 57

4.3.1 BAPN Alters LOX Expression and Collagen Fibers Differently in Femoral and Maxillary Osseous Wound Sites 57

4.3.2 Viscoelastic Properties are Altered in Defect Sites Compared to Existing Bone with BAPN Treatment 58

4.3.3 Delayed Healing Rate in Maxilla Compared to Femur, Yet Healing Rate is Not Changed with BAPN Treatment 59

4.3.4 Femur Osteoclast Numbers Initially Reduced with BAPN, then Increased at Day 14 59

4.4 Discussion 60

4.5 Acknowledgements 62

4.6 Author Contributions 63

4.7 References 76

Chapter 5. Discovery of a Novel Serum Detectable Bone Collagen Cross-link 79

5.1 Introduction 79

5.2 Methods 81

5.2.1 Serum Samples 81

5.2.2 Protein Quantification, Depletion and Visualization 81

5.2.3 Cross-link Quantification via LC-MS 82

5.3 Results 83

5.3.1 Depletion of High Molecular Weight Proteins from Serum was Required to Detect Collagen Cross-Links via LC-MS 83

5.3.2 Novel Detection of DHLNL and HLNL in Mouse and Human Serum 84

5.4 Discussion 85

5.5 Conclusions 87

5.6 Acknowledgements 88

5.7 Author Contributions 88

5.8 References 97

Chapter 6. Conclusions and Future Directions 100

6.1 Bone Matrix Composition and Response to Cross-link Perturbation are Anatomically Site-Dependent 100

6.2 Craniofacial and Long Bone have Altered Healing Rates and Osteoclast Response to BAPN 101

6.3 LOX as a Therapeutic Target in Healing 102

6.4 Craniofacial and Long Bone Mechanical Response to BAPN 103

6.5 Serum Detectible Collagen Cross-links Specificity to bone to Translate to a Minimally Invasive Indicator of Bone Quality 104

6.6 Assay of Hydroxylation Status and Implications for Serum Detectable Cross-links Profiles in Additional Tissues (Systemic and Local) 106

6.7 Concluding Remarks 107

6.8 References 108

List of Tables

Table 3.1 Cross-links of interest with respective chemical formulas, molecular mass, and accurate masses of [M+H]+ charged ions of cross-links.. 40

Table 3.2 Direct measures of collagen cross-link profile from mandibles and femurs as measured by LC-MS. 44

Table 3.3S Supplemental summary table of tissue level mechanical data, histomorphometry, and MicoCT. 47

Table 4.1 Birefringent analysis of red and green channels using CT-FIRE for the femoral and maxillary defects. 68

Table 5.1 Cross-links of interest with respective chemical formulas, molecular mass, and accurate masses of [M+H]+ charged ions of cross-links.. 91

Table 5.2 Summary of serum detectible collagen cross-links in mouse and human serum. 96

List of Figures

Figure 1.1 Three-dimensional model of tooth and periodontal ligament movement (A), isolated to a two dimensional map (B), histological staining at the same region (C). 11

Figure 1.2 Simplified collagen cross-linking pathways for both enzymatic cross-link and advanced glycation end product (AGE) formation. 12

Figure 3.1 Dynamic histomorphometry of the mandible and femur. 41

Figure 3.2 MicroCT and tissue level mechanics between bone compartments. 42

Figure 3.3 Differences in collagen cross-link profiles between bones. 43

Figure 3.4 BAPN significantly reduced the mature cross-links in the mandible but not the femur. 45

Figure 3.5. Numerous site-specific compositional differences between the mandible and femur were seen in mineral and matrix as measured via Raman Spectroscopy. 46

Figure 4.1 Schematic of experimental design (A) 2 treatments (Phosphate buffered saline (PBS) or 350 mg/kg beta-aminoproprionitrile (BAPN)) and two end points (7 day or 14 day post surgery). 64

Figure 4.2 Equation used to calculate a fit of the Burgers model to the experimental data for extraction of viscoelastic properties of the bone at either the defect location or intracortical location. 65

Figure 4.3 Immunohistochemistry depicting lysyl oxidase (LOX) enzyme positive bone areas in the maxillary and femoral defects with phosphate buffered saline (PBS) or beta-aminoproprionitrile (BAPN). 66

Figure 4.4 Representative images of the workflow for birefringent analysis of the Picrosirius Red histological sections. 67

Figure 4.5 Nanoindentation was used to determine the Young's modulus, stiffness, hardness, and viscoelastic creep properties of new, healing bone (defect), compared to the adjacent, non-defect bone (intracortical) that was unaffected by surgery or by beta-aminoproprionitrile (BAPN) treatment. 69

Figure 4.6 Viscoelastic measures were extracted from the Burger's model to estimate creep behavior..... 70

Figure 4.7 Representative images (TOP LEFT - FEMUR, AND RIGHT - MAXILLA) of microCT 3D images of the defects at day 7 and 14 for control (PBS) and beta-aminoproprionitrile (BAPN) groups. 72

Figure 4.8 Representative images (TOP LEFT - FEMUR, AND BOTTOM LEFT - MAXILLA) of tartrate resistant alkaline phosphatase (TRAP) staining to highlight osteoclasts in the healing defects at day 7 and 14 for the control (PBS) and beta-aminoproprionitrile (BAPN) treatment groups..... 73

Figure 4.9S1 Representative images (TOP LEFT - FEMUR, AND BOTTOM LEFT - MAXILLA) of Masson's trichrome staining to highlight collagen in the healing defects at day 7 and 14 for both the control (PBS) and beta-aminoproprionitrile (BAPN) groups..... 74

Figure 4.10S2 Non-defect sites (pre-maxillary suture or distal femur trabeculae) of tartrate resistant alkaline phosphatase (TRAP) staining to highlight osteoclasts and masons trichrome staining to highlight collagen for the defects at day 7 and 14 for both the control (PBS) and beta-aminoproprionitrile (BAPN) groups were quantified for changes to osteoclasts, osteoblasts and % empty lacunae. 75

Figure 5.1 Bone collagen serum formation markers are considered to be cleavage products at the N- and C- terminal regions of type I collagen where cross-linking occurs.. 89

Figure 5.2 Schematic highlighting the workflow optimized for measuring mature and immature collagen cross-links from serum using ultra-high performance liquid chromatography with tandem mass spectrometry (LC-MS). 90

Figure 5.3 Protein precipitation of mouse serum enhances mass spectrometry signal for the internal standard, pyridoxine. 92

Figure 5.4 Protein precipitation depleted most of the protein in the high molecular weight (HMW) (> 65 kD) fraction. 93

Figure 5.5 Quantification of cross-link standards. 94

Figure 5.6 Chromatograms of cross-links in mouse and human serum. 95

Abstract

Compromised collagen and mineral can lead to decreases in bone quantity and quality in a variety of diseases that differentially affect craniofacial and long bones. Since bone is a composite - with mineral lending stiffness and collagen lending toughness - maintaining balance of both constituents is critical to the physical integrity and sustained function of bone. Experimental models of perturbed collagen cross-links utilize beta-aminoproprionitrile (BAPN), a dose-dependent inhibitor of the lysyl oxidase enzyme that catalyzes formation of the enzymatic collagen cross-links – pyridinolines and pyrroles (mature) as well as aldimines (immature). The ratios of immature to mature cross-links correlate with bone strength and toughness in long bones. However, a full cross-link profile of craniofacial bone and distinction between craniofacial and long bones have not been investigated. Likewise, site-specific compositional and mechanical consequences of collagen perturbation are lacking. The central hypothesis of this thesis is that collagen cross-linking inhibition compromises bone quality in a bone-specific manner (long bone or craniofacial bone) in normal growth (aim 1) and in osseous wound healing (aim 2), and that a full panel of bone cross-links can be detected in serum (aim 3).

During normal growth in the mouse femur and mandible, bone composition (mineral and collagen) showed an anatomical dependence including ~30% higher carbonation in the femur and ~67% higher mature/immature collagen ratio in the mandible. A highly sensitive liquid chromatography/mass spectrometry method was developed which allowed for discovery of the advanced glycation end-product, carboxymethyl-lysine (CML) in mouse bones for the first time. Accumulation of CML was bone dependent, with ~22X higher levels in the mandible than the femur. BAPN caused a significant increase in carbonation (4.4%) in the femur, but no change in the mandible and no change in tissue level mechanics. BAPN significantly decreased mandibular mature cross-links (~22-38% for subsets of mature cross-links) but not in the femur. This altered response to BAPN highlights the need to further understand how altered collagen differentially affects composition in craniofacial and long bones.

To study the effects of BAPN on bone healing and mechanical properties, sub-critical osseous defects were created in the femur and maxilla of mice subjected to collagen perturbation via BAPN. BAPN decreased tissue level mechanics (stiffness, hardness, and Young's modulus, viscoelastic properties) in newly formed bone differently between the maxilla and femur. Yet, there was no change in bone volume with BAPN, only differences in healing between the femur (~60% increase in bone volume between 7-14 days) and maxilla (no significant change). BAPN initially decreased the number of osteoclasts in the femoral defect osteoclasts (7 days), then increased (14 days), with no change in the maxilla. This site-specific response of mechanics and osteoclasts to local changes in collagen matrix may make lysyl oxidase mediated collagen cross-linking a potential therapeutic target for controlling site specific osteoclast response.

Additionally, serum detectible cross-links were measured as a potential minimally invasive assay to assess direct bone cross-links. Described here is the first report of immature cross-links measured in both mouse and human serum, creating the most comprehensive bone collagen cross-link analysis in serum to date.

Overall, this thesis work has advanced the understanding the role of collagen cross-linking in mineralization during normal growth and healing, and the differential effects in craniofacial and long bone. Also established, was a new potential assay for measuring bone cross-links in serum.

Chapter 1.
Advancements in Composition and Structural Characterization of Bone to Inform Mechanical Outcomes and Modelling[1]

1.1 Introduction

The hierarchical nature of bone necessitates that structure-function relationships be defined across multiple length scales. The skeleton is constantly adapting to maintain mechanical function through structural and compositional changes triggered by biological signaling. Historically, modeling of structure-function relationships has been based on continuum mechanics, with less focus on physiologically-relevant nanostructural and compositional features. Advances in the ability to genetically or biochemically perturb bone composition as well as imaging modalities to visualize nano-scale architecture, embrace the potential to understand the relationship between bone biology, structure, composition and mechanics.

The foundation of bone mechanics is based on traditional mechanical testing procedures. However, most mechanical testing of bone assumes mechanical properties can be measured by modeling bone as an idealized geometry with homogenous, isotropic properties (i.e., three or four -point bending, torsion, fatigue) [1]. For example, fracture toughness of a rodent whole bone can be calculated by modeling the bone as a cylindrical tube, allowing for standard beam bending assumptions to be made [2]. As a biologic material, bone is not static, but constantly remodeling, changing dimensions, and altering material properties due to endogenous and exogenous influences. Therefore, it is critical for modeling of bone biomechanics to incorporate a hierarchical approach - taking into account how bones adapt to altered functional demands via changes in shape (length scale of mm), internal architecture (length scale of μm) and mineral or collagen changes (length scale of nm).

[1] Published as: Genevieve E. Romanowicz, Morgan W. Bolger, David H. Kohn; Advancements in composition and structural characterization of bone to inform mechanical outcomes and modelling. Current Opinion in Biomedical Engineering. 11 (2019), 76-84.

Biological influence is an added complexity to the structure-function analysis rubric, as genetic alterations manifest themselves throughout the hierarchy of bone composition and structure. Advancements in genetic manipulation of animal models allow researchers to investigate how changes in cellular behavior (osteoblast, osteocyte, osteoclast activity), propagate to changes in, composition (collagen, mineral, proteins, growth factors) and structure (porosity, lacuno-canalicular network), and ultimately to changes in mechanical function. The purpose of this review is to describe the multiple scales at which bone can be understood and characterized, highlighting new state-of-the-art techniques such that structural, compositional, and biological changes can be incorporated into biomechanical modeling.

1.2 Whole Bone Level

Understanding bone function on a bulk, mechanical scale has been limited by simplifying assumptions about the geometric shape and the resolution at which the tissue can be modeled and analyzed. Advanced computing and imaging technologies such as high-resolution peripheral quantitative computed tomography (HR-pQCT) and high-resolution magnetic resonance imaging (MRI), now allow for solid body objects to be created from scans of numerous skeletal tissues and used as input into multidimensional models to simulate physiologic loads. Such models are predictive of direct mechanical measures such as bone strength, but are less predictive of post-yield mechanics [3]. With the advent of imaging such as HR-pQCT and MRI, actual bone in-situ geometries and loading schemes can be studied, something not possible using traditional mechanical testing methods (samples trimmed to standard beams for mechanical testing). Enhanced in situ modeling lends itself to more accurate depictions of in vivo loading and understanding of biomechanical processes. More accurate modeling of complex geometries such as the bone/periodontal ligament/tooth unit [4], human vertebrae [5], the atlantoaxial joint [6] is now possible. Smaller scale features such as microcracks in trabecular struts and vasculature [7] can also be incorporated into whole bone mechanical models. For example, in the dentoalveolar joint, the forces modeled coupled with histological stains for vascular, neuronal, and osteoblastic tissues, allow for attribution of mechanical forces and tooth movement to bone resorption processes (Figure 1.1). Coupling of advanced imaging techniques of bone with local measures of cellular activity (ie. histology or gene expression) and mapping into whole bone mechanics [4]

will increase understanding of how local structural and matrix changes impact whole bone mechanics and function.

1.3 Structure & Geometry

To initially gain understanding of structure-function relationships in bone, morphological measures, such as external diameter [8], moment of inertia and trabecular network [9], were critical. Increasing resolution of imaging systems has allowed for the study of intracortical features such as porosity and the canalicular networks, leading to enhanced understanding of structural influences on mechanical properties.

1.3.1 Porosity

Advances in methods such as micro/nano-computed tomography have allowed for the nano-scale quantification of mineralized tissues [10] and rendering of 3D models of these tissue for finite element modeling [11,12]. A significant aspect of this approach is that a biological process such as modeling/remodeling of bone with age can be captured by quantifiable size and density changes in pore geometry. This pore information can be applied to multivariate models to predict whole bone strength [13] or employed in a computational model to determine correlations between porosity and strain energy density [11]. The use of nano-CT has allowed for increased resolution and definition of cortical pores and highlighted the regulation of human bone strength with age in phenotypic subsets of the population [13]. Therefore, porosity is an important factor to consider in overall structure of cortical tissues of long bones, and may be of interest in other bone sites.

1.3.2 Osteocytes and the Lacuna-Canalicular Network

Osteocytes are embedded in the mineralized matrix of bone and form a complex network between the lacunae they reside in and their interconnecting canaliculi. This fluid-filled network senses mechanical loads and transduces the mechanical signal to a biochemical signal that triggers bone turnover and adaptation. The surrounding mineralized matrix and nano-scale features of the osteocyte network make it difficult to study and image in three dimensions. However, recent advancements allow for more thorough visualization of the osteocyte lacuno-

canalicular network (LCN). Two dimensional visualization can be accomplished by resin casting of bone sections [14] or acid etching of embedded samples [15]. One method to visualize the three dimensional structure of the LCN is by staining bone sections with rhodamine, which will infiltrate internal network surfaces, including blood vessels, lacunae, and canaliculi. Confocal imaging, z-stacking and subsequent image processing allows for a resolution of 250-300 nm [16,17]. Use of third-harmonic generation imaging to visualize rhodamine infiltrated sections has had similar success [18,19]. Synchrotron nano computed tomography (SR-nanoCT) also been able to image the 3D network of the LCN after rigorous segmentation and reconstruction methods [20]. Ptychographic X-ray CT (PXCT) relies on diffraction and subsequent retrieval algorithms, and provides three dimensional images of the LCN and lacunae shape [21]. Three-dimensional images of the osteocyte LCN, like those obtained by SR-nanoCT, can also be used to model the mechanical loads put upon the network and better understand fluid shear and mechanosensing [22].

The complex geometry of the LCN output from two dimensional stacked, or three dimensional images can be difficult to subsequently characterize. Key parameters of the LCN include lacunar density, total number of osteocyte connections, lacuno-canalicular fraction or network parameters likes edge density, node degree, and centrality measures [23,24]. Future work should focus on determining which measures of the osteocyte LCN are most relevant to bone mechanosensing, composition, and mechanics. Being able to probe the properties of the LCN has promising implications for understanding how disease, age, and other physiologies influence loading adaptations.

1.4 Composition

Just as bone is often simplified into a beam or cylinder shape for mechanical testing, the composition of bone is often simplified as a two-phase composite, comprised of a stiff mineral component imbedded in a tensile polymeric or collagen matrix. Technological advances have allowed for better characterization of the mineral, collagen, interactions between the mineral and collagen, and cellular components of bone. Accounting for the ultrastructural features of mineral, collagen and other proteins advance the ability to link functional relevance of bone composition to disease.

1.4.1 Enzymatic Cross-Links

Collagen is a bio-polymer, which is assembled in type I collagen as fibrils and acquires post-translational, covalent modifications via the family of enzymes: lysyl hydroxylases (LH), lysyl oxidase (LOX), or via the formation of advanced glycation end products (AGEs such as pentosidine (PEN)) (Figure 1.2). These enzymes control tissue-specific patterning of the enzymatic cross-links. In bone, the predominant immature cross-links are the divalent cross-links, dihydroxylysinonorleucine (DHLNL), hydroxylysinonorleucine (HLNL). The predominant mature cross-links form spontaneously from either the DHLNL or HLNL with an available allysine or hydroxyallisine group (from which the immature cross-links form as well). These mature cross-links are the hydroxylysylpyridinoline (PYD), lysylpyridinoline (DPD), and pyrroles. The non-enzymatic AGEs form from an available lysine or hydroxylysine group via glycation or oxidative stress.

Intermolecular, lysyl-oxidase mediated, collagen cross-links stabilize type I collagen and contribute to mechanical properties of bone. Techniques to measure cross-links directly have relied on high performance liquid chromatography (HPLC), with a reverse phase ion-pairing column chemistry and fluorescent detection. Naturally fluorescing cross-links (PYD, DPD, PEN) can be easily detected, however, non-fluorescent species (DHLNL, HLNL) require derivatization by ninhydrin or o-pthalaldehyde for fluorescent detection [25]. This LC methodology has been translated to electrospray ionization mass spectrometry (ESI-MS) [26], which allows for comprehensive quantification of the enzymatic collagen cross-links without subsequent derivatization steps. Recently, a methodology was developed using a silica hydride column and ESI-MS friendly solvents that allowed for detection of reduced immature cross-links HLNL, DHLNL, and mature cross-link, PYD [27]. DPD, in addition to PYD, was measured with a similar methodology [28]. Coupling of mass spectrometry detection with LC methods allows for precise quantification of additional species (ie. proteins) in parallel with the enzymatic collagen cross-links, such as other AGEs besides PEN. Beyond LC, it may be possible to quantify proteins *in situ* using matrix-assisted laser desorption/ionization-imaging mass spectrometry (MALDI-IMS) [29].

These methodologies outlined above allow for characterization of the entire collagen cross-link profile with age, disease, or other physiological conditions to elucidate the relationship between composition and mechanics, which can subsequently be applied experimentally or to *in silico* predictive models of mechanics. For example, in a mouse model of lathyrism in which LOX is inhibited, bone fracture toughness, strength, and pyridinoline cross-link content are reduced [25]. Ratios reflecting relative cross-link maturity are positive regressors of fracture toughness, whereas quantities of mature pyridinoline cross-links are significant positive regressors of strength. Subjecting these mice to exercise promotes pyridinoline cross-linking, and the resulting increase in total mature cross-linking is sufficient to counteract the mechanical effects of cross-link inhibition [30].

In silico modeling of the collagen network in bone has been conducted using full atomistic simulations and finite element simulations. This approach is useful for controlled manipulations of theoretical conformations of collagen that can be confirmed experimentally. Recently, the use of 3D coarse-grained models simulated the mechanical behavior of collagen fibrils with enzymatic collagen cross-links [31]. This model was applied to collagen cross-links in human adult and child bone samples to predict fibril mechanical properties and found the increased number of immature enzymatic cross-links (HLNL, DHLNL) in young bone (5-16 years), was responsible for the increased elastic modulus and elastic work in bones from young vs. old individuals [32]. Being able to model how differing collagen cross-links affect the deformation of collagen fibrils is a step towards modeling how composition dictates bone mechanics. However, to advance such modeling even further, mineral, AGEs, and their interaction should also be considered.

1.4.2 Non-Enzymatic Cross-Links & Advanced Glycation End Products (AGEs)

Characterization of non-enzymatic collagen cross-links or advanced glycation end products (AGEs) relies on fluorescent detection of pentosidine as a surrogate marker for total AGE content or in a non-specific fluorometric assay [33]. To date, no complete profile of AGEs in bone has been done. Computational techniques using atomistic models of collagen fibrils have tried to identify other AGEs that may form in bone. Candidates identified include glucosepane and imidazolium cross-links [34,35]. Modeling the relative mechanical contribution of these

candidate AGEs showed a theoretical increase in moduli at low strains with variations between glucosepane and imidazolium cross-links depending on site [36]. Experimental confirmation of the results of these computational studies with established screening methodologies for AGEs [37] would advance understanding of the AGE profile in bone, relative abundance and contribution of AGEs to bone strength and toughness, especially in regards to pathologies which accumulate AGEs [33].

1.4.3 Mineral

Bone mineral is comprised of hydroxyapatite crystals with varying size, crystallinity and stoichiometry, depending on location, age, and disease. Characterization of bone mineral scales from bulk or regional bone mineral density measured using techniques such as microCT and dual x-ray absorptiometry (DEXA), to molecular composition at a micro-scale resolution using techniques such as Raman spectroscopy, Fourier transformation infrared technology (FTIR), quantitative backscattered electron microscopy (qBEI), as well as a combination of these technologies [38]. Combinations of techniques allow for a more comprehensive understanding of bone mineral at multiple structural scales.

Carbonation of hydroxyapatite is the primary compositional modification of bone mineral, and changes in percent carbonation are associated with changes in tissue location, age, maturity, and disease [39]. In addition to compositional changes, altered mineral orientation and crystallinity dictate mechanical properties [39–41], especially ductility [42]. Crystallinity is influenced by multiple factors including collagen (the scaffold in and around which crystallites form) and non-collagenous proteins (which provide nucleation sites for crystallite formation) [39]. Crystallinity, as measured via Raman spectroscopy, can be defined as the inverse of full width at half maximum (FWHM) of the 960 cm^{-1} phosphate (v1) peak, indicating more stoichiometric hydroxyapatite, or less carbonate substitutions with an increase in crystallinity. The phosphate peak can be compared to the carbonate peak at 1070 cm^{-1} to give a direct carbonate-to-phosphate ratio [43]. Additionally, crystallinity measured via FTIR can be described as the ratio of the 1020/1030 cm^{-1} bands and indicates crystal size, perfection, and maturation [44]. On a smaller scale than Raman or FTIR, qBEI can assess mineral nano-structure and distribution of spatial changes in mineral [45–47].

Understanding the crystalline phase of bone, including structure, composition, size, and orientation, is important for understanding mechanical function as well as cellular function. Cellular control of bone crystallinity is regulated by non-collagenous proteins such as biglycan [40] or fibrillin [48], or by upstream mechanical means, such as exercise [40,49,50]. Mechanical function measured by nanoindentation can be colocalized with compositional techniques such as Raman [51], or FT-IR. Nanoindentation has utility for measuring site-specific mechanical properties (hardness and Young's modulus) of bone as well as teeth [52] and can be performed on hydrated or dehydrated specimens and also coupled with fluorescence microscopy [30,53,54]. Atomic force microscopy (AFM) can be coupled with infrared spectroscopy (AFM-IR) to provide nanometer scale resolution in collagen topography and composition, mineral composition and ratios of mineral to collagen [55]. Sequential analysis of mineral composition and tissue level mechanical properties [56] allows for non-destructive mechanical and compositional measures at micron scales across bone or skeletal locations. Combining techniques such as these to investigate effects of genetic alterations on bone composition and mechanics will advance understanding of the local cellular influence on composition and, structure, and ultimately function.

1.5 Genetic Manipulations of Bone Composition and Structure

Identifying the cellular and genetic drivers for compositional and structural changes is crucial to understand why bone mechanics are altered in different pathologies. Technological advances in biology, most notably, Clustered Regularly Interspaced Palindromic Repeats (CRISPR)/CRISPR-associated protein (Cas) pathway (CRISPR/Cas9) [57] and transgenic Cre lines [58] allow for precise genetic manipulation. When coupled with compositional, structural, and mechanical characterization, researchers would have the tools to model skeletal phenotype from genotypic information. Using these technologies to generate mouse or other animal models which mirror human mutations opens the door to investigating specific skeletal phenotypes present in a clinical setting [59].

Mechanical phenotyping the skeleton of genetic knockouts allows for unbiased screening to identify new drivers or confirm those previously found. Databases like the Origins of Bone and Cartilage Disease collaboration project (OBCD, http://www.boneandcartilage.com) correlate

genetic regulation to bulk bone mechanical properties and mineralization information. This approach identified genetic mutations that had strong influence over mechanical properties [60]. This work has also highlighted dimorphisms in bone volume, size and weight by both sex and site [61]. Further investigating these skeletal phenotypes at a compositional and structural level may provide insight into how bone mechanics is impacted by specific mutations. For example, an analysis of a Smad3 (a mediator of TGF-beta signaling in bone) knockout was conducted using several compositional (Raman, X-ray tomography), structural, and mechanical (nanoindentation, three-point bending) techniques. With these methods, mineral content, cortical thickness and fracture toughness were most controlled by the Smad3 gene [62]. Often, genetic animal models investigate only bulk mechanical or mineralization, but do not attribute how the genetic regulators are affecting compositional changes. By using techniques to dissect the compositional changes in bone, including recently developed techniques highlighted in this review, it may be possible to model how specific genes are regulate the structure-function relationships in bone.

1.6 Summary

Biomechanics is at an exciting interface between classic mechanics, state of the art technology to characterize bone structure and composition at the micro- and nano-scales, and molecular tools to generate knockouts of virtually any gene. Future compositional analysis should be directed so that mineral, collagen, and structural parameters can be incorporated into simulated models of bone function. With technological advances, the ability to determine the biological drivers of structural and functional changes in bone becomes possible. Translation of clinical phenotypes to relevant animal models to better understand pathologies in human populations is a critical goal. Likewise, technologies used to characterize quality of bone should be pushed towards clinical translation with minimally invasive measures of bone architecture, mineral quantity, and tissue quality, that when combined with simulated models of bone mechanics, can be used to predict function and identify subjects at increased risk for fragility fractures.

1.7 Acknowledgements

I would like to thank my co-authors for this review: Morgan Bolger and David Kohn. This work was supported by the National Institutes of Health T32 DE007057-43, F30 DE028167-01A1, R01 AR065424. The authors have no declarations of interest.

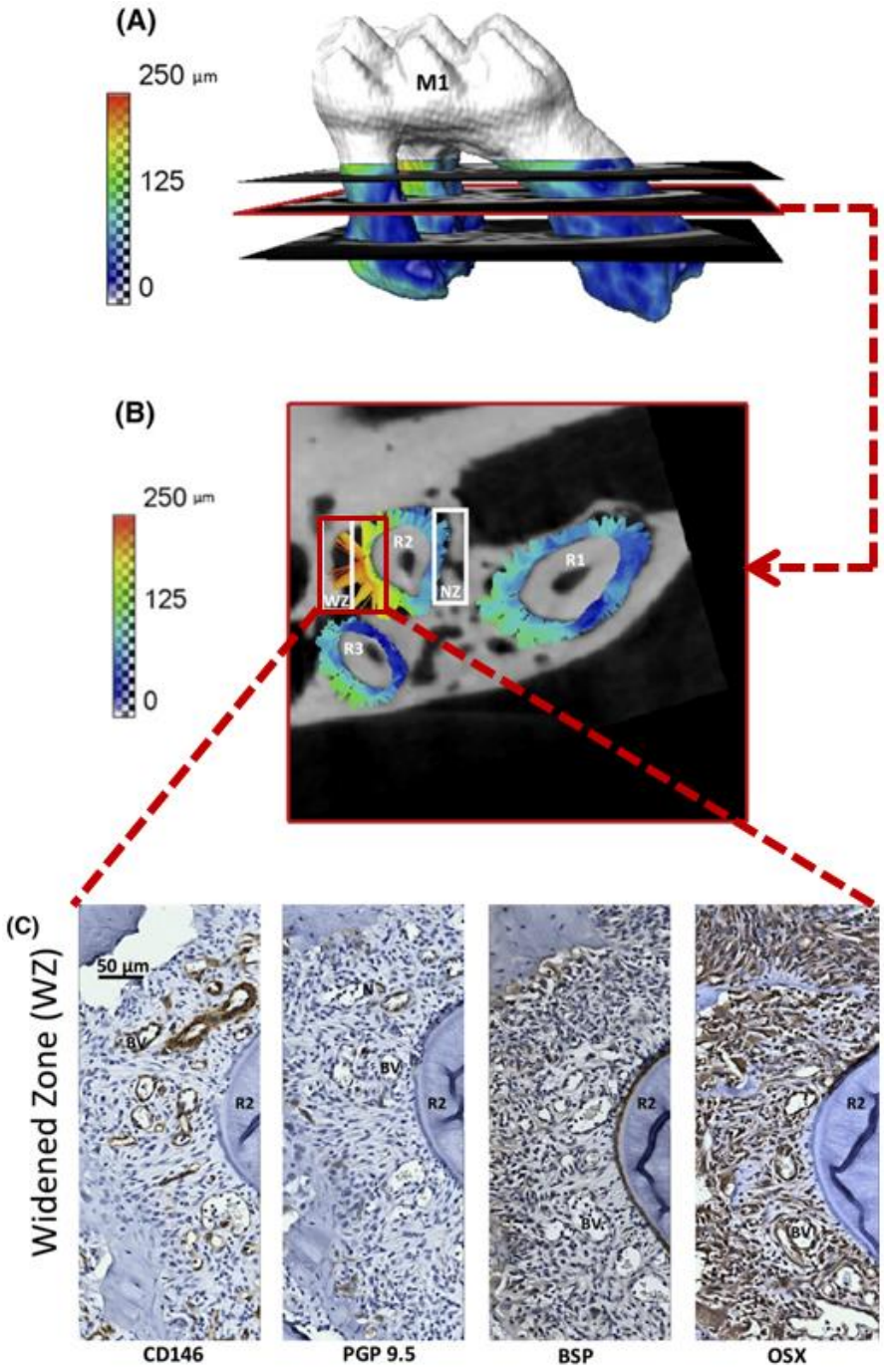

Figure 1.1 Three-dimensional model of tooth and periodontal ligament movement (A), isolated to a two dimensional map (B), histological staining at the same region (C). Modeling of forces and tissue movement experienced under loading of complex geometries such as the dentoalveolar joint has been made possible by increases in nano-scale resolution of imaging and high powered computer processing. These modeled forces can then be correlated to biological drivers by more traditional means such as histology and staining of proteins related to neurovasculature and osteoblasts (Adapted from [4], with permission).

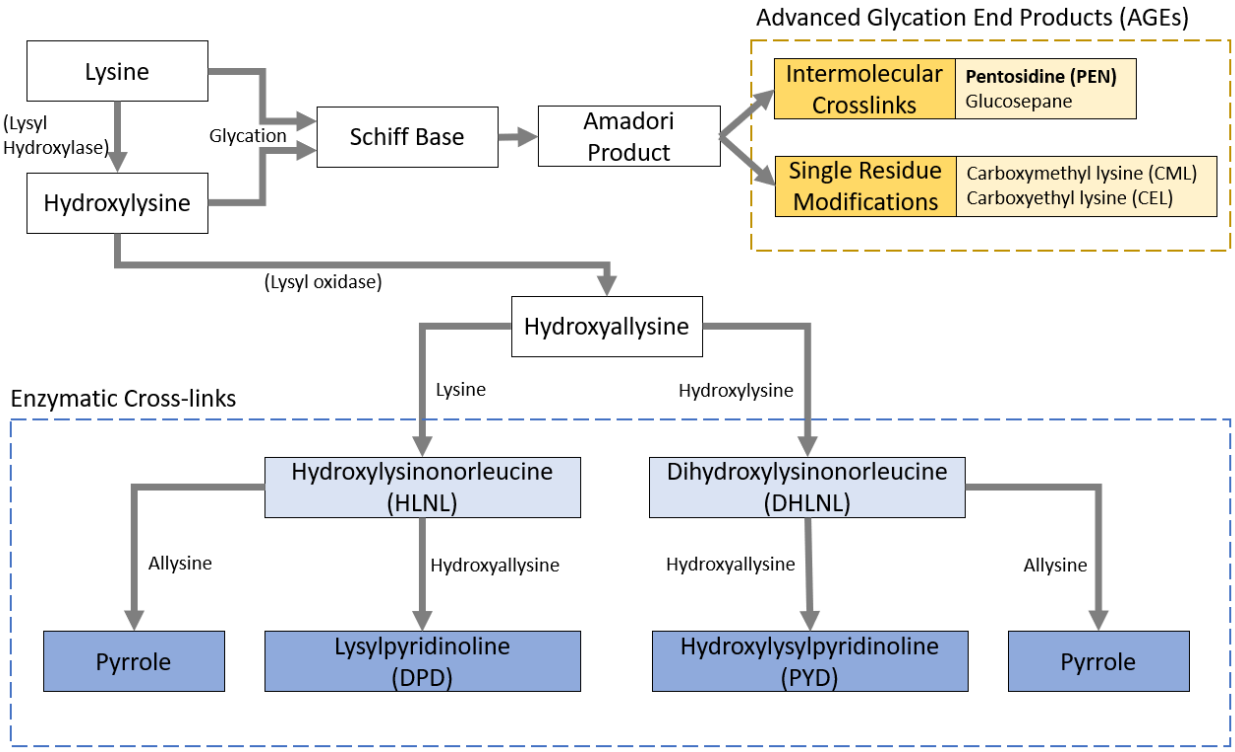

Figure 1.2 Simplified collagen cross-linking pathways for both enzymatic cross-link and advanced glycation end product (AGE) formation. Immature divalent enzymatic cross-links are simplified to their sodium borohydride reduced forms hydroxylysinonorleucine (HLNL) and dihydroxylysinonorleucine (DHLNL) (Adapted from [63], with permission)

1.8 References

[1] H. Beaupied, E. Lespessailles, C.-L. Benhamou, Evaluation of macrostructural bone biomechanics, Joint Bone Spine. 74 (2007) 233–239. doi:10.1016/j.jbspin.2007.01.019.

[2] R.O. Ritchie, K.J. Koester, S. Ionova, W. Yao, N.E. Lane, J.W. Ager, Measurement of the toughness of bone: a tutorial with special reference to small animal studies, Bone. 43 (2008) 798–812. doi:10.1016/j.bone.2008.04.027.

[3] C.S. Rajapakse, E.A. Kobe, A.S. Batzdorf, M.W. Hast, F.W. Wehrli, Accuracy of MRI-based finite element assessment of distal tibia compared to mechanical testing, Bone. 108 (2018) 71–78. doi:10.1016/j.bone.2017.12.023.

[4] L. Yang, M. Kang, R. He, B. Meng, A. Pal, L. Chen, A.H. Jheon, S.P. Ho, Microanatomical changes and biomolecular expression at the PDL-entheses during experimental tooth movement, J. Periodontal Res. 54 (2019) 251–258. doi:10.1111/jre.12625.

[5] M.C. Costa, G. Tozzi, L. Cristofolini, V. Danesi, M. Viceconti, E. Dall'Ara, Micro Finite Element models of the vertebral body: Validation of local displacement predictions, PloS One. 12 (2017) e0180151. doi:10.1371/journal.pone.0180151.

[6] S. Duan, L. Zhang, C. Lin, H. Zhong, Finite Element Modeling of Atlantoaxial Joint with the Vertebral Artery Based on CT Data, in: Atlantis Press, 2016. doi:10.2991/meici-16.2016.101.

[7] M.A. Hammond, J.M. Wallace, M.R. Allen, T. Siegmund, Mechanics of linear microcracking in trabecular bone, J. Biomech. 83 (2019) 34–42. doi:10.1016/j.jbiomech.2018.11.018.

[8] A.M. Parfitt, C.H. Mathews, A.R. Villanueva, M. Kleerekoper, B. Frame, D.S. Rao, Relationships between surface, volume, and thickness of iliac trabecular bone in aging and in osteoporosis. Implications for the microanatomic and cellular mechanisms of bone loss., J. Clin. Invest. 72 (1983) 1396–1409. https://www.ncbi.nlm.nih.gov/pmc/articles/PMC370424/ (accessed April 24, 2019).

[9] M. Hahn, M. Vogel, M. Pompesius-Kempa, G. Delling, Trabecular bone pattern factor--a new parameter for simple quantification of bone microarchitecture, Bone. 13 (1992) 327–330.

[10] C.L. Gregg, A.K. Recknagel, J.T. Butcher, Micro/nano-computed tomography technology for quantitative dynamic, multi-scale imaging of morphogenesis, Methods Mol. Biol. Clifton NJ. 1189 (2015) 47–61. doi:10.1007/978-1-4939-1164-6_4.

[11] L.P. Bakalova, C.M. Andreasen, J.S. Thomsen, A. Brüel, E.-M. Hauge, B.J. Kiil, J.-M. Delaisse, T.L. Andersen, M.E. Kersh, Intracortical Bone Mechanics Are Related to Pore

Morphology and Remodeling in Human Bone, J. Bone Miner. Res. 33 (2018) 2177–2185. doi:10.1002/jbmr.3561.

[12] G.M. Campbell, J.A. Peña, S. Giravent, F. Thomsen, T. Damm, C.-C. Glüer, J. Borggrefe, Assessment of Bone Fragility in Patients With Multiple Myeloma Using QCT-Based Finite Element Modeling, J. Bone Miner. Res. Off. J. Am. Soc. Bone Miner. Res. 32 (2017) 151–156. doi:10.1002/jbmr.2924.

[13] E.M. Bigelow, D.M. Patton, F.S. Ward, A. Ciarelli, M. Casden, A. Clark, R.W. Goulet, M.D. Morris, S.H. Schlecht, G.S. Mandair, T.L. Bredbenner, D.H. Kohn, K.J. Jepsen, External Bone Size Is a Key Determinant of Strength-Decline Trajectories of Aging Male Radii, J. Bone Miner. Res. 0 (n.d.) e3661. doi:10.1002/jbmr.3661.

[14] U.E. Pazzaglia, T. Congiu, The cast imaging of the osteon lacunar-canalicular system and the implications with functional models of intracanalicular flow, J. Anat. 222 (2013) 193–202. doi:10.1111/joa.12004.

[15] T. Lampi, H. Dekker, C.M.T. Bruggenkate, E.A.J.M. Schulten, J.J.W. Mikkonen, A. Koistinen, A.M. Kullaa, Acid-etching technique of non-decalcified bone samples for visualizing osteocyte-lacuno-canalicular network using scanning electron microscope, Ultrastruct. Pathol. 42 (2018) 74–79. doi:10.1080/01913123.2017.1384418.

[16] M. Kerschnitzki, W. Wagermaier, P. Roschger, J. Seto, R. Shahar, G.N. Duda, S. Mundlos, P. Fratzl, The organization of the osteocyte network mirrors the extracellular matrix orientation in bone, J. Struct. Biol. 173 (2011) 303–311. doi:10.1016/j.jsb.2010.11.014.

[17] M. Kerschnitzki, P. Kollmannsberger, M. Burghammer, G.N. Duda, R. Weinkamer, W. Wagermaier, P. Fratzl, Architecture of the osteocyte network correlates with bone material quality, J. Bone Miner. Res. 28 (2013) 1837–1845. doi:10.1002/jbmr.1927.

[18] R. Genthial, E. Beaurepaire, M.-C. Schanne-Klein, F. Peyrin, D. Farlay, C. Olivier, Y. Bala, G. Boivin, J.-C. Vial, D. Débarre, A. Gourrier, Label-free imaging of bone multiscale porosity and interfaces using third-harmonic generation microscopy, Sci. Rep. 7 (2017). doi:10.1038/s41598-017-03548-5.

[19] R. Genthial, M. Gerbaix, D. Farlay, L. Vico, E. Beaurepaire, D. Débarre, A. Gourrier, Third harmonic generation imaging and analysis of the effect of low gravity on the lacuno-canalicular network of mouse bone, PLOS ONE. 14 (2019) e0209079. doi:10.1371/journal.pone.0209079.

[20] M.A. Zuluaga, M. Orkisz, P. Dong, A. Pacureanu, P.-J. Gouttenoire, F. Peyrin, Bone canalicular network segmentation in 3D nano-CT images through geodesic voting and image tessellation, Phys. Med. Biol. 59 (2014) 2155–2171. doi:10.1088/0031-9155/59/9/2155.

[21] A. Ciani, H. Toumi, S. Pallu, E.H.R. Tsai, A. Diaz, M. Guizar-Sicairos, M. Holler, E. Lespessailles, C.M. Kewish, Ptychographic X-ray CT characterization of the osteocyte

lacuno-canalicular network in a male rat's glucocorticoid induced osteoporosis model, Bone Rep. 9 (2018) 122–131. doi:10.1016/j.bonr.2018.07.005.

[22] P. Varga, B. Hesse, M. Langer, S. Schrof, N. Männicke, H. Suhonen, A. Pacureanu, D. Pahr, F. Peyrin, K. Raum, Synchrotron X-ray phase nano-tomography-based analysis of the lacunar–canalicular network morphology and its relation to the strains experienced by osteocytes in situ as predicted by case-specific finite element analysis, Biomech. Model. Mechanobiol. 14 (2015) 267–282. doi:10.1007/s10237-014-0601-9.

[23] P.R. Buenzli, N.A. Sims, Quantifying the osteocyte network in the human skeleton, Bone. 75 (2015) 144–150. doi:10.1016/j.bone.2015.02.016.

[24] P. Kollmannsberger, M. Kerschnitzki, F. Repp, W. Wagermaier, R. Weinkamer, P. Fratzl, The small world of osteocytes: connectomics of the lacuno-canalicular network in bone, New J. Phys. 19 (2017) 073019. doi:10.1088/1367-2630/aa764b.

[25] E.M.B. McNerny, B. Gong, M.D. Morris, D.H. Kohn, Bone fracture toughness and strength correlate with collagen cross-link maturity in a dose-controlled lathyrism mouse model, J. Bone Miner. Res. Off. J. Am. Soc. Bone Miner. Res. 30 (2015) 455–464. doi:10.1002/jbmr.2356.

[26] E. Gineyts, O. Borel, R. Chapurlat, P. Garnero, Quantification of immature and mature collagen crosslinks by liquid chromatography-electrospray ionization mass spectrometry in connective tissues, J. Chromatogr. B Analyt. Technol. Biomed. Life. Sci. 878 (2010) 1449–1454. doi:10.1016/j.jchromb.2010.03.039.

[27] R. Naffa, G. Holmes, M. Ahn, D. Harding, G. Norris, Liquid chromatography-electrospray ionization mass spectrometry for the simultaneous quantitation of collagen and elastin crosslinks, J. Chromatogr. A. 1478 (2016) 60–67. doi:10.1016/j.chroma.2016.11.060.

[28] R. Naffa, S. Watanabe, W. Zhang, C. Maidment, P. Singh, P. Chamber, M.T. Matyska, J.J. Pesek, Rapid analysis of pyridinoline and deoxypyridinoline in biological samples by liquid chromatography with mass spectrometry and a silica hydride column, J. Sep. Sci. 0 (n.d.). doi:10.1002/jssc.201801292.

[29] Y. Fujino, T. Minamizaki, H. Yoshioka, M. Okada, Y. Yoshiko, Imaging and mapping of mouse bone using MALDI-imaging mass spectrometry, Bone Rep. 5 (2016) 280–285. doi:10.1016/j.bonr.2016.09.004.

[30] E.M.B. McNerny, J.D. Gardinier, D.H. Kohn, Exercise increases pyridinoline cross-linking and counters the mechanical effects of concurrent lathyrogenic treatment, Bone. 81 (2015) 327–337. doi:10.1016/j.bone.2015.07.030.

[31] B. Depalle, Z. Qin, S.J. Shefelbine, M.J. Buehler, Influence of cross-link structure, density and mechanical properties in the mesoscale deformation mechanisms of collagen fibrils, J. Mech. Behav. Biomed. Mater. 52 (2015) 1–13. doi:10.1016/j.jmbbm.2014.07.008.

[32] B. Depalle, A.G. Duarte, I.A.K. Fiedler, L. Pujo-Menjouet, M.J. Buehler, J.-P. Berteau, The different distribution of enzymatic collagen cross-links found in adult and children bone result in different mechanical behavior of collagen, Bone. 110 (2018) 107–114. doi:10.1016/j.bone.2018.01.024.

[33] D. Vashishth, Advanced Glycation End-products and Bone Fractures, IBMS BoneKEy. 6 (2009) 268–278. doi:10.1138/20090390.

[34] T.A. Collier, A. Nash, H.L. Birch, N.H. de Leeuw, Intra-molecular lysine-arginine derived advanced glycation end-product cross-linking in Type I collagen: A molecular dynamics simulation study, Biophys. Chem. 218 (2016) 42–46. doi:10.1016/j.bpc.2016.09.003.

[35] A. Gautieri, A. Redaelli, M.J. Buehler, S. Vesentini, Age- and diabetes-related nonenzymatic crosslinks in collagen fibrils: Candidate amino acids involved in Advanced Glycation End-products, Matrix Biol. 34 (2014) 89–95. doi:10.1016/j.matbio.2013.09.004.

[36] T.A. Collier, A. Nash, H.L. Birch, N.H. de Leeuw, Effect on the mechanical properties of type I collagen of intra-molecular lysine-arginine derived advanced glycation end-product cross-linking, J. Biomech. 67 (2018) 55–61. doi:10.1016/j.jbiomech.2017.11.021.

[37] P.J. Thornalley, S. Battah, N. Ahmed, N. Karachalias, S. Agalou, R. Babaei-Jadidi, A. Dawnay, Quantitative screening of advanced glycation endproducts in cellular and extracellular proteins by tandem mass spectrometry, Biochem. J. 375 (2003) 581–592. doi:10.1042/BJ20030763.

[38] H.B. Hunt, E. Donnelly, Bone quality assessment techniques: geometric, compositional, and mechanical characterization from macroscale to nanoscale, Clin. Rev. Bone Miner. Metab. 14 (2016) 133–149. doi:10.1007/s12018-016-9222-4.

[39] Adele Boskey, Bone mineral crystal size, Osteoporos. Int. J. Establ. Result Coop. Eur. Found. Osteoporos. Natl. Osteoporos. Found. USA. 14 Suppl 5 (2003) S16-20; discussion S20-21. doi:10.1007/s00198-003-1468-2.

[40] J.M. Wallace, K. Golcuk, M.D. Morris, D.H. Kohn, Inbred strain-specific effects of exercise in wild type and biglycan deficient mice, Ann. Biomed. Eng. 38 (2010) 1607–1617. doi:10.1007/s10439-009-9881-0.

[41] J.M. Wallace, K. Golcuk, M.D. Morris, D.H. Kohn, Inbred strain-specific response to biglycan deficiency in the cortical bone of C57BL6/129 and C3H/He mice, J. Bone Miner. Res. Off. J. Am. Soc. Bone Miner. Res. 24 (2009) 1002–1012. doi:10.1359/jbmr.081259.

[42] J.S. Yerramshetty, O. Akkus, The associations between mineral crystallinity and the mechanical properties of human cortical bone, Bone. 42 (2008) 476–482. doi:10.1016/j.bone.2007.12.001.

[43] M.D. Morris, G.S. Mandair, Raman assessment of bone quality, Clin. Orthop. 469 (2011) 2160–2169. doi:10.1007/s11999-010-1692-y.

[44] E.P. Paschalis, E. DiCarlo, F. Betts, P. Sherman, R. Mendelsohn, A.L. Boskey, FTIR microspectroscopic analysis of human osteonal bone, Calcif. Tissue Int. 59 (1996) 480–487. doi:10.1007/BF00369214.

[45] F. He, A.E. Chiou, H.C. Loh, M. Lynch, B.R. Seo, Y.H. Song, M.J. Lee, R. Hoerth, E.L. Bortel, B.M. Willie, G.N. Duda, L.A. Estroff, A. Masic, W. Wagermaier, P. Fratzl, C. Fischbach, Multiscale characterization of the mineral phase at skeletal sites of breast cancer metastasis, Proc. Natl. Acad. Sci. 114 (2017) 10542–10547. doi:10.1073/pnas.1708161114.

[46] J.D. Gardinier, S. Al-Omaishi, M.D. Morris, D.H. Kohn, PTH signaling mediates perilacunar remodeling during exercise, Matrix Biol. J. Int. Soc. Matrix Biol. 52–54 (2016) 162–175. doi:10.1016/j.matbio.2016.02.010.

[47] J.D. Gardinier, S. Al-Omaishi, N. Rostami, M.D. Morris, D.H. Kohn, Examining the influence of PTH(1-34) on tissue strength and composition, Bone. 117 (2018) 130–137. doi:10.1016/j.bone.2018.09.019.

[48] N.B. Kavukcuoglu, E. Arteaga-Solis, S. Lee-Arteaga, F. Ramirez, A.B. Mann, Nanomechanics and Raman spectroscopy of fibrillin 2 knock-out mouse bones, J. Mater. Sci. 42 (2007) 8788–8794. doi:10.1007/s10853-007-1918-x.

[49] M.A. Hammond, J.M. Wallace, Exercise prevents β-aminopropionitrile-induced morphological changes to type I collagen in murine bone, BoneKEy Rep. 4 (2015) 645. doi:10.1038/bonekey.2015.12.

[50] D.H. Kohn, N.D. Sahar, J.M. Wallace, K. Golcuk, M.D. Morris, Exercise Alters Mineral and Matrix Composition in the Absence of Adding New Bone, Cells Tissues Organs. 189 (2009) 33–37. doi:10.1159/000151452.

[51] M. Raghavan, N.D. Sahar, D.H. Kohn, M.D. Morris, Age-specific profiles of tissue-level composition and mechanical properties in murine cortical bone, Bone. 50 (2012) 942–953. doi:10.1016/j.bone.2011.12.026.

[52] G. Sereda, A. VanLaecken, J.A. Turner, Monitoring demineralization and remineralization of human dentin by characterization of its structure with resonance-enhanced AFM-IR chemical mapping, nanoindentation, and SEM, Dent. Mater. 35 (2019) 617–626. doi:10.1016/j.dental.2019.02.007.

[53] B.P. Sinder, W.R. Lloyd, J.D. Salemi, J.C. Marini, M.S. Caird, M.D. Morris, K.M. Kozloff, Effect of anti-sclerostin therapy and osteogenesis imperfecta on tissue-level properties in growing and adult mice while controlling for tissue age, Bone. 84 (2016) 222–229. doi:10.1016/j.bone.2016.01.001.

[54] S. Blouin, N. Fratzl-Zelman, A. Roschger, W.A. Cabral, K. Klaushofer, J.C. Marini, P. Fratzl, P. Roschger, Cortical bone properties in the Brtl/+ mouse model of Osteogenesis imperfecta as evidenced by acoustic transmission microscopy, J. Mech. Behav. Biomed. Mater. 90 (2019) 125–132. doi:10.1016/j.jmbbm.2018.10.010.

[55] L. Imbert, S. Gourion-Arsiquaud, E. Villarreal-Ramirez, L. Spevak, H. Taleb, M.C.H. van der Meulen, R. Mendelsohn, A.L. Boskey, Dynamic structure and composition of bone investigated by nanoscale infrared spectroscopy, PloS One. 13 (2018) e0202833. doi:10.1371/journal.pone.0202833.

[56] X. Bi, C.A. Patil, C.C. Lynch, G.M. Pharr, A. Mahadevan-Jansen, J.S. Nyman, Raman and mechanical properties correlate at whole bone- and tissue-levels in a genetic mouse model, J. Biomech. 44 (2011) 297–303. doi:10.1016/j.jbiomech.2010.10.009.

[57] B.O. Williams, M.L. Warman, Perspective: CRISPR/Cas9 technologies, J. Bone Miner. Res. Off. J. Am. Soc. Bone Miner. Res. 32 (2017) 883–888. doi:10.1002/jbmr.3086.

[58] S.L. Dallas, Y. Xie, L.A. Shiflett, Y. Ueki, Mouse Cre Models for the Study of Bone Diseases, Curr. Osteoporos. Rep. 16 (2018) 466–477. doi:10.1007/s11914-018-0455-7.

[59] I. Schrauwen, A.P. Giese, A. Aziz, D.T. Lafont, I. Chakchouk, R.L.P. Santos-Cortez, K. Lee, A. Acharya, F.S. Khan, A. Ullah, D.A. Nickerson, M.J. Bamshad, G. Ali, S. Riazuddin, M. Ansar, W. Ahmad, Z.M. Ahmed, S.M. Leal, FAM92A Underlies Nonsyndromic Postaxial Polydactyly in Humans and an Abnormal Limb and Digit Skeletal Phenotype in Mice, J. Bone Miner. Res. Off. J. Am. Soc. Bone Miner. Res. 34 (2019) 375–386. doi:10.1002/jbmr.3594.

[60] J.H.D. Bassett, A. Gogakos, J.K. White, H. Evans, R.M. Jacques, A.H. van der Spek, S.M.G. Project, R. Ramirez-Solis, E. Ryder, D. Sunter, A. Boyde, M.J. Campbell, P.I. Croucher, G.R. Williams, Rapid-Throughput Skeletal Phenotyping of 100 Knockout Mice Identifies 9 New Genes That Determine Bone Strength, PLOS Genet. 8 (2012) e1002858. doi:10.1371/journal.pgen.1002858.

[61] D.W. Rowe, D.J. Adams, S.-H. Hong, C. Zhang, D.-G. Shin, C. Renata Rydzik, L. Chen, Z. Wu, G. Garland, D.A. Godfrey, J.P. Sundberg, C. Ackert-Bicknell, Screening Gene Knockout Mice for Variation in Bone Mass: Analysis by μCT and Histomorphometry, Curr. Osteoporos. Rep. 16 (2018) 77–94. doi:10.1007/s11914-018-0421-4.

[62] G. Balooch, M. Balooch, R.K. Nalla, S. Schilling, E.H. Filvaroff, G.W. Marshall, S.J. Marshall, R.O. Ritchie, R. Derynck, T. Alliston, TGF-beta regulates the mechanical properties and composition of bone matrix, Proc. Natl. Acad. Sci. U. S. A. 102 (2005) 18813–18818. doi:10.1073/pnas.0507417102.

[63] M. Saito, K. Marumo, Collagen cross-links as a determinant of bone quality: a possible explanation for bone fragility in aging, osteoporosis, and diabetes mellitus, Osteoporos. Int. J. Establ. Result Coop. Eur. Found. Osteoporos. Natl. Osteoporos. Found. USA. 21 (2010) 195–214. doi:10.1007/s00198-009-1066-z.

Chapter 2.
Hypothesis, Study Aims and Organization of Dissertation

2.1 Study Rationale

Maintaining the physical integrity of biological tissues such as bone, is critical to their sustained function. Many systemic conditions such as osteogenesis imperfecta[1], diabetes[2], rheumatoid arthritis[3] and nutritional deficiencies[4] exhibit compositional changes in both the collagen and mineral components of bone, which compromise function. In experimental models of perturbed collagen cross-links, the mechanical strength and toughness correlate to the cross-link profile[4][5]. Therefore, it is possible that compositional changes contribute to altered structure and function and compromise bone quality in patients suffering from a variety of systemic conditions[1][2][3][6]. Most structure/composition-function studies in bone have been performed on long bones, but only a limited number of studies have analyzed craniofacial bone. Yet, differential changes to mineral density exist between craniofacial and long bones[7]. It is unknown if such differences are driven by differences in embryonic origin[8], turnover rate[9], loading[10][11], or composition of the bone. Limited studies report anatomical differences such as between the mandible and femur for direct measures of collagen[12][13] or in combination with mineral composition and tissue level mechanics. Understanding these mechanical and compositional changes is important for understanding baseline and pathological progression in a variety of diseases which may affect the long bones differently than craniofacial bones. I hypothesize that cross-links will drive altered mechanical properties, mineralization and healing dependent on anatomical site.

Type I collagen is a bio-polymer, which is assembled collagen as fibrils and acquires post-translational, covalent modifications via the enzymes lysyl hydroxylase (LH) and lysyl oxidase (LOX) or via the non-enzymatic pathway with advanced glycation end products (AGEs). These enzymes control tissue specific patterning of the enzymatic cross-links. Thus far, the contribution of collagen cross-links to mechanical properties, mineralization, and healing

between craniofacial and long bone has not been measured but may contribute to site specific response to disease states.

2.2 Hypothesis and Aims

2.2.1 Global Hypothesis:

My central hypothesis is that collagen cross-linking inhibition compromises bone quality in both situations of (1) normal growth and (2) osseous healing, dependent on bone (long bone or craniofacial bone) and (2) that bone cross-link changes can be detected via a full panel in serum.

2.2.2 Hypothesis 1: Altered collagen cross-linking reduces mineral quality in a mineral apposition rate and anatomical site dependent manner.

Aim 1. Define the role of collagen cross-links in craniofacial and long bone mineralization and quality.

To determine the differential effect of cross-link inhibition on craniofacial bone, vs. long bone, femora and mandibles were isolated from 8 week old mice (growing mice to incorporate BAPN treatment) that have been treated with BAPN or control PBS, for 28 days. Direct measures of the collagen cross-links were performed on the femur and mandible by Ultra-high performance liquid chromatography with tandem mass spectrometry (LC-MS). Mineral apposition rate was determined from dynamic histomorphometry. Mineral composition (via Raman spectroscopy) and quantity (via microCT) were measured. Nanoindentation was used to determine mechanical properties co-localized to the Raman measures. The resulting mechanical and compositional information was then used to explain observed anatomical site dependent changes with BAPN and further our understanding of the influence of collagen cross-linking on bone formation during growth. These compositional (or nano-scale structural changes), could ultimately affect the long-term function of both the femur and mandible.

2.2.3 Hypothesis 2: Perturbed collagen via BAPN impairs the quality of bone healing and is dependent on anatomical site due to differences in LOX activity and healing rate.

Aim 2. Determine the effect of impaired collagen cross-links on bone quality during osseous wound healing in a subcritical defect model and establish differential healing between

craniofacial and long bones. To determine the effects of enzymatic cross-links on bone quality following osseous wound healing, daily subcutaneous injections of BAPN (350 mg/kg for 7d) were administered to C57Bl/6 male mice to deplete enzymatic collagen cross-links systemically. Subcritical osseous defects (0.43 mm) were then created bilaterally, in both the maxilla and femur, and allowed to heal for 7 or 14 days. The maxilla and femur were processed for histomorphometry and immunohistochemistry. Osteoclasts and osteoblasts were enumerated as multinucleated cells that are tartrate-resistant acid phosphatase (TRAP) stained/bone surface and cuboidal cells/bone surface, respectively, to determine effects of BAPN treatment on these cells. Birefringence with polarized light was performed on Picrosirius stained slides to determine collagen organization. Immunohistochemistry for LOX was performed and quantified for the defect sites. Mechanical properties of the healing tissue were measured via nanoindentation including the extraction of viscoelastic properties using a fit to a Burger's model. MicroCT was used to assess healing (bone volume/total volume). Direct measures of the collagen cross-links will be made on mandibles by HPLC. The resulting histological, mechanical, and microCT information was then used to compare healing processes between the maxilla and femur with differential response to perturbed collagen via BAPN.

2.2.4 Hypothesis 3: Immature cross-links, dihydroxylysinorleucine and hydroxylysinorleucine, are detectible in serum at higher ratios than mature pyridinolines.

Aim 3. Determine the relationship of serum detectable bone markers to estimate bone quality measures. Mouse serum and human serum were depleted of high molecular weight proteins via acetonitrile protein precipitation. Ultra-high performance liquid chromatography with tandem mass spectrometry (LC-MS) was then used to quantify the serum detectible cross-links, including the immature cross-links: dihydroxylysinorleucine and hydroxylysinorleucine. The correlation of the full panel of serum detectible cross-links directly to bone will be completed. This new methodology is an important step to creating a serum assay that can detect bone related cross-link changes in a variety of diseases and conditions, and potentially to be used to assess bone quality.

2.3 Summary and Organization of Dissertation

In Chapter 1, a detailed presentation of the current state of the field with regards to analyzing and modeling complex hierarchical structure of bone is presented as well as future directions of the field. Chapter 3 demonstrates the bone dependent (mandible vs. femur) changes in collagen cross-links and mineralization during normal growth (Aim 1). Work in Aim 1 also identifies a new direct measure of the carboxy methyl-lysine (CML) cross-link in mouse bone as well as the bone-dependent accumulation of this cross-link. Chapter 4 furthers the work of Chapter 3 by pushing the biological system into a state of accelerated bone deposition in a subcritical defect model (Aim 2). Work in Aim 2 demonstrated that both healing and the quality of the healed bone depend on anatomical location (maxilla vs. femur). Chapter 4 addresses Aim 3 where the nuanced methods for the novel detection of immature cross-links are described as well as establishment of a full collagen cross-link panel in mouse and human serum, opening doors for the creation of a "liquid biopsy" of bone collagen cross-link profile to eventually work towards the possibility of better prediction of bone quality via minimally invasive techniques. Chapter 5 summarized the key findings and proposed future work to build on these discoveries. Overall, this work sought to understand the role of collagen cross-linking in mineralization processes during normal growth and healing as well as work to translate the knowledge gained into a clinically relevant question of how to detect bone collagen cross-links via serum.

2.4 References

1. Daley E, Streeten EA, Sorkin JD, Kuznetsova N, Shapses SA, Carleton SM, Shuldiner AR, Marini JC, Phillips CL, Goldstein SA, Leikin S, McBride DJ. Variable bone fragility associated with an Amish COL1A2 variant and a knock-in mouse model. Journal of Bone and Mineral Research. 2010;25(2):247–61.

2. Marin C, Papantonakis G, Sels K, van Lenthe GH, Falgayrac G, Vangoitsenhoven R, Van der Schueren B, Penel G, Luyten F, Vandamme K, Kerckhofs G. Unraveling the compromised biomechanical performance of type 2 diabetes- and Roux-en-Y gastric bypass bone by linking mechanical-structural and physico-chemical properties. Scientific Reports. Nature Publishing Group; 2018 Apr 12;8(1):5881.

3. Inzana JA, Maher JR, Takahata M, Schwarz EM, Berger AJ, Awad HA. Bone fragility beyond strength and mineral density: Raman spectroscopy predicts femoral fracture toughness in a murine model of rheumatoid arthritis. Journal of Biomechanics. 2013 Feb 22;46(4):723–30.

4. McNerny EMB, Gardinier JD, Kohn DH. Exercise increases pyridinoline cross-linking and counters the mechanical effects of concurrent lathyrogenic treatment. Bone. 2015 Dec 1;81:327–37.

5. McNerny EM, Gong B, Morris MD, Kohn DH. Bone Fracture Toughness and Strength Correlate With Collagen Cross-Link Maturity in a Dose-Controlled Lathyrism Mouse Model. Journal of Bone and Mineral Research. 2015;30(3):455–64.

6. Zofkova I, Davis M, Blahos J. Trace Elements Have Beneficial, as Well as Detrimental Effects on Bone Homeostasis. Physiol Res. 2017 Jun 30;391–402.

7. Lee C, Lee J-H, Han S-S, Kim YH, Choi Y-J, Jeon KJ, Jung HI. Site-specific and time-course changes of postmenopausal osteoporosis in rat mandible: comparative study with femur. Scientific Reports. Nature Publishing Group; 2019 Oct 2;9(1):14155.

8. Chung U, Kawaguchi H, Takato T, Nakamura K. Distinct osteogenic mechanisms of bones of distinct origins. Journal of Orthopaedic Science. 2004 Jul 1;9(4):410–4.

9. Huja SS, Fernandez SA, Hill KJ, Li Y. Remodeling dynamics in the alveolar process in skeletally mature dogs. The Anatomical Record Part A: Discoveries in Molecular, Cellular, and Evolutionary Biology. 2006;288A(12):1243–9.

10. Tsouknidas A, Jimenez-Rojo L, Karatsis E, Michailidis N, Mitsiadis TA. A Bio-Realistic Finite Element Model to Evaluate the Effect of Masticatory Loadings on Mouse Mandible-Related Tissues. Front. Physiol. Frontiers in Physiology. 2017 May 9; 8(273):1-8.

11. Edwards WB, Schnitzer TJ, Troy KL. Bone mineral and stiffness loss at the distal femur and proximal tibia in acute spinal cord injury. Osteoporos Int. 2014 Mar 1;25(3):1005–15.

12. Matsuura T, Tokutomi K, Sasaki M, Katafuchi M, Mizumachi E, Sato H. Distinct Characteristics of Mandibular Bone Collagen Relative to Long Bone Collagen: Relevance to Clinical Dentistry. BioMed Research International. 2014 April 10, Article ID 769414.

13. Sasaki M, Matsuura T, Katafuchi M, Tokutomi K, Sato H. Higher Contents of Mineral and Collagen but Lower of Hydroxylysine of Collagen in Mandibular Bone Compared with Those of Humeral and Femoral Bones in Human. Journal of Hard Tissue Biology. 2010;19(3):175–80.

Chapter 3.

Collagen Cross-link Profiles Differ Between Craniofacial and Long Bones Driving Altered Mineralization Response to Perturbed Collagen

3.1 Introduction

Complex structures, such as bone, rely on a multitude of structural properties to impart the high strength and resilience required for daily function. Bones are a composite material, primarily comprised of fibrillar type I collagen (organic phase, ~35-45% by volume), carbonated hydroxyapatite crystals (mineral phase, ~35-45% by volume), and water (~15-25% by volume)[1]. Compromises to either the amount or composition of collagen or mineral in bone can alter both homeostasis and healing. A variety of diseases exhibit features of altered collagen (cross-link ratios) and bone mineral density (BMD), impaired healing, and reduced bone strength (increased fragility)[2][3][4][5]. Changes to mineral density are observed in both the craniofacial and long bones (albeit at different rates) with disease[6]. The impact of systemic skeletal disease on composition may be site-specific, especially between craniofacial and long bones due to differences in embryonic origin[7], turnover rate[8], and loading[9][10]. Limited studies[11][12] report differences in direct measures of collagen between the mandible and femur and none in combination with mineral composition and tissue level mechanics. Yet, understanding these mechanical and compositional changes is important for understanding baseline and pathological progression in a variety of disease which affect the long bones differently than craniofacial bones.

Type I collagen is assembled as fibrils and acquires post-translational, covalent modifications via the family of enzymes lysyl hydroxylases (LH) and lysyl oxidase (LOX)[13][14], or via the formation of advanced glycation end products (AGEs) such as pentosidine (PEN) or carboxymethyl-lysine (CML)[15][16]. LH and LOX control tissue-specific patterning of the enzymatic cross-links[17][18]. In bone, the predominant immature enzymatic cross-links are the

divalent cross-links, dihydroxylysinonorleucine (DHLNL) and hydroxylysinonorleucine (HLNL) which form from available lysine and hydroxylysine groups. Mature cross-links form spontaneously from either the DHLNL or HLNL cross-links with an available allysine or hydroxyallysine group. The predominant mature cross-links are hydroxylysylpyridinoline (PYD), lysylpyridinoline (DPD), and pyrroles (Pyr). Similar to immature cross-links, the non-enzymatic AGEs also form from lysine and hydroxylysine side groups via glycation or oxidative stress. Some studies[12][19] have suggested that the cross-link profile of long bones differs from that of craniofacial bones, yet comprehensive profiles have not been established .

While individual type I collagen cross-links are similar between long bones and craniofacial bones, craniofacial bones have a higher turnover rate[8], with a higher collagen percentage by weight and a greater mineral content[12]. These differences are often not considered when studying diseases or therapies involving bone. However, if the composition (e.g. mineral/collagen ratio, % cross-links, cross-link profile) is inherently different between long and craniofacial bone, the respective tissues may resorb or form bone differently in response to disease, therapy or mechanical loading. The direct contribution of collagen cross-links to mechanical properties and mineralization at a tissue level has not been measured. Nor has the potential for altered collagen cross-linking to influence mineralization and tissue level mechanics. And lastly, the impact of highly different composition (mineral and collagen) between anatomical locations (such as between craniofacial and long bones) has not been measured. The central hypothesis of this aspect of the dissertation is that *altered collagen cross-linking reduces mineral quality in a mineral apposition rate and anatomical site (cross-link profile) dependent manner.* This hypothesis is tested by comparing the mandible to the femur in a model system that targets LOX mediated enzymatic cross-linking via inhibition by beta-aminoproprionitrile (BAPN)[20][21][22]. This model directly tests the effects of enzymatic cross-links on mineralization and tissue level mechanics as well as the effects of cross-link inhibition among several anatomical sites with inherently different collagen and mineral composition.

3.2 Methods

3.2.1 Animals

Details of the mouse experiment were previously reported[20] with analysis of the tibia only. This work adds intensive compositional, histomorphometric, and tissue level mechanical analysis of the femur and the mandible as well as liquid chromatography analysis of cross-links with mass spectrometry compared to fluorescent detection. In brief, all animal procedures were approved by the Institutional Animal Care & Use Committee (IACUC) at the University of Michigan. 5-week old, male C57Bl6 (Charles River) were weight matched and assigned to two treatment groups. Daily subcutaneous injections of sterile phosphate buffered saline (PBS) or 350 mg/kg (Beta-aminoproprionitrile fumarate salt, CAS: 2079-89-2, Sigma Aldrich, St. Louis, MO, USA) were administered over 21 days. Since BAPN only affects newly deposited tissue, growing mice were used for this study to generate a sufficient volume of cross-link inhibited tissue. To provide labelling for dynamic histomorphometric analysis and discriminating newly deposited tissue (cross-link deficient) from existing tissue (normal cross-links), weekly fluorochrome injections were administered – days 1 (alizarin complexone (Alizarin-3-methyl-iminodiacetic acid), 25 mg/kg, Sigma A3882), 7 (calcein, 15 mg/kg, Sigma C-0875), 13 (xylenol orange, 90 mg/kg, Sigma 398187) and 19 (tetracycline hydrochloride, 25 mg/kg, Sigma T3383). Mice were sacrificed at 8 weeks of age by CO_2 inhalation (experimental day 22). Both femora and mandibles were harvested, cleaned of soft tissue, and stored frozen in gauze soaked in calcium buffered PBS as previously reported[20][22].

3.2.2 MicroCT

Left hemi-mandibles (7-8/group) and left femora (6/group) were scanned by μCT over the entire length (μCT100 Scanco Medical, Bassersdorf, Switzerland). Scan settings were: voxel size 12 μm, 70 kVp, 114 μA, 0.5 mm AL filter, and integration time 500 ms. Scans were reoriented using Scanco IPL to obtain reproducible regions of interest (ROI). A 360 μm standard ROI was taken from the mid root of the first mandibular premolar for interradicular bone, and then rotated 90 degrees to achieve cortical bone sections at the buccal bone of the first molar. Femoral trabecular bone structure was analyzed using a 600 μm thick volume of interest 2.8 mm

below the distal end of the femoral epiphysis. Distal cortex was measured at 6 mm from the distal end of the epiphysis for a 360 μm thick volume. Bone volume/total volume (BV/TV), tissue mineral density (TMD) were calculated for the mandibular cortex, interradicular bone, femoral cortex and trabeculae. Trabecular number (Tb.N), spacing (Tb.Sp) and thickness (Tb.Th) were also calculated. The sites analyzed for microCT correspond to the ROI for Raman spectroscopy, histomorphometry, and nanoindentation analysis. All microCT analysis was performed using the manufacturer's evaluation software, and a fixed global threshold of 18% (180 on a grayscale of 0–1000) was used to segment bone from non-bone.

3.2.3 Collagen Cross-link Analysis

Sample preparation for direct measures of collagen cross-linking was conducted as previously described[20][22]. Direct cross-link analysis was performed using ultra-high performance liquid chromatography with tandem mass spectrometry (LC-MS) and adapted from previously described methods[23][24] with modifications to expand the number of cross-links detected. Mature (PYD, DPD, and pyrrole), immature (DHLNL and HLNL), and AGE cross-links (PEN and CML) were measured from each whole bone specimen, quantified via a standard curve of each cross-link and normalized to the collagen content (hydroxyproline). For the femora, the epiphyses were removed, and the marrow was flushed with PBS (n=5-6/group). For the mandibles, the central incisor, molars, and condyle were removed and cleaned with PBS (n=5-6/group). Both bones were then demineralized with 0.5 M ethylene diamine tetracetic acid (EDTA) for 72 hours, washed, suspended in TAPSO buffer, chopped, and reacted with sodium borohydride to preserve the immature cross-links[25][22][20]. Samples were then digested with TPCK-treated trypsin at 37 C for 24 hours then defatted with 3:1 chloroform:methanol. This digest was used for the pyrrole colorimetric assay, an additional aliquot of digest was used for hydrolysis, mixing 1:1 with 12 M hydrochloric acid and baked at 110 C for 24 hours. A portion of the hydrolysate was used for the hydroxyproline assay and the remainder was cleaned on an SPE column (Bond Elut-Cellulose, 12102095, Agilent) as described[25] with a 35 mL wash with 8:1:1 (Acetonitrile: Acetic Acid: Water) and methods slightly modified by eluting with 5 mL of LCMS grade water (W64, Fisher), Samples were then lyophilized and resuspended in 0.1% formic acid (A117-50, Fisher) in LC-MS water spiked with pyridoxine as in internal standard for subsequent LC-MS injection as a modification of previous methods[25] to more closely match

established LC-MS methods[23][24]. LC-MS (Agilent 6545 LC/Q-TOF) conditions were adapted from Naffa, et. al.[23][24] and as follows: injection volume: 5 μL, gradient elution program: Solvent A, 100% water/0.1% formic acid (v/v); solvent B, 100% acetonitrile/0.1% formic acid (v/v). Gradient: 0 min 90% solvent B, 2 min 84% solvent B, 12 min 42% solvent B and 17 min 10% solvent B. Total run time was 17 min and flow rate was 0.4 mL/min followed by 4 min of column equilibration time (total run time 21 min), column temp: 25 C.

The mass spectrometer used was the MS Q-TOF equipped with dual Jet Stream Technology Ion Source (AJS) Electrospray ionization spectrometry (ESI). Positive ion mode was used in all runs. System parameters were: column temperature, 35 C; sheath gas (N2) temperature: 320 C, flow: 10 L/min; Positive ion mode was used with a mass range of 50– 1200 m/z, scan rate: 2 spectra/second. All data were processed using Thermo Xcalibur 3.0 software. Agilent MassHunter Workstation Qualitative Analysis software version B.06.01 SP1 (Agilent Technologies, Santa Clara, CA, USA) was used for qualitative analysis and quantitation. A known mass list (detailed in Table 3.1) was used for extraction of ion chromatograms for quantification as compared to the standard curves for each species of cross-link.

Standards of the PYD (CAS# 63800-01-1, BOCSCI Inc.) and DPD (CAS # 83462-55-9, BOCSCI Inc.) were purchased, DHLNL was purchased from ChemCruz (sc-207059C) and used to quantify HLNL as well since they only differ by an oxygen and no standard is commercially available. CML (Cayman, 16483) and PEN (Cayman, 10010254) were purchased from Cayman Chemical. Pyrrole standard was purchased (Sigma, M78801) and used in a colorimetric assay[22][20]. Individual cross-links as well as grouped values for total mature (PYD + DPD + pyrroles), total pyridinolines (PYD + DPD), total immature (DHLNL + HLNL), total enzymatic cross-links (total immature + total mature) were calculated. Relevant ratios reported are DHLNL/HLNL, PYD/DPD, (total pyridinolines)/pyrroles, immature/mature, immature/(total pyridinolines). Collagen content (hydroxyproline) ratios to demineralized and mineralized bone weights were also calculated.

3.2.4 Histomorphometry

Mice treated with PBS or BAPN (C57Bl/6, n=5-7) were prepared for dynamic histomorphometry processing. In brief, bones were fresh embedding in poly-methyl-

methacrylate (PMMA) (Koldmount, SPI Supplies), sectioned and polishing with a series of fine-grit sandpaper as described[26]. The fluorescent labels were visualized using a confocal microscope (Nikon Eclipse T*i* confocal microscope). Images were analyzed for mineral apposition rate (MAR) at 3-5 locations along the ROI and averaged for each site using the Nikon software.

3.2.5 Raman Spectroscopy

Mineral composition and matrix composition were measured via Raman Spectroscopy as previously described[22][27][28]. In brief, the polished section from the histomorphometry samples (n = 6-8/group) were used, with the fluorescent regions of interest being probed with a 10 nm laser spot to quantify mineral and matrix parameters. The peaks associated with mineral were used to test the impact of altered collagen cross-linking on mineral quantity and quality. Measurements of "mineral to matrix" included a variety of ratios of phosphate to individual matrix bands: hydroxyproline (960 cm^{-1}/874 cm^{-1}), proline (960 cm^{-1}/854 cm^{-1}), phenylalanine (960 cm^{-1}/1001cm^{-1}), or amide I (960 cm^{-1}/1660 cm^{-1}). Measurement of mineral quality were described as "mineral stoichiometric perfection" or phosphate crystallinity (full width of 960 cm^{-1} peak at half maximum height), and "mineral maturity" or carbonate to phosphate ratio (960 cm^{-1}/1069 cm^{-1}). Matrix (collagen) parameters were described as Amide I (1660 cm^{-1}/1694 cm^{-1}) and (1660 cm^{-1}/1679 cm^{-1}), and Amide III 1240 cm^{-1}/1263 cm^{-1}). All reported peaks are from peak height at given wavenumber from processed and baselined spectra as previously described[27].

3.2.6 Nanoindentation

Tissue level mechanical properties were measured (n=6-8/group) and co-localized with the histomorphometric and the Raman spectroscopic measurements (2 separate sites per bone with 5-8 independent indents averaged per location). Samples were sectioned and polished with a final polish of 0.25 μm diamond suspension (Electron Microscopy Sciences, 50372-21) to create a smooth surface as previously described[26]. A Berkovich tip was then loaded at each site at 10 μNs^{-1}, to 1000 μN, then unloaded at 10 μNs^{-1} using a 950 TI TriboIndenter (Hysitron, Minneapolis, MN, USA). Indentations were conducted in a humid state via surface hydration

with calcium buffered PBS. Young's modulus and hardness were extracted from the load-displacement curve generated using the Oliver-Pharr method[29].

3.2.7 Statistics

The study was designed with a power calculation based on the primary outcome of altered mineral (carbonate/phosphate via Raman spectroscopy) calculated with means and variance from previous work[22] for a two-tailed t-test and yielded a minimum of n=5. IBM SPSS was used for statistical analysis. Raw data was analyzed for assumptions of normality (Shapiro-Wilk) and homogeneity of variance (Levene). Where valid, independent treatment effects in each compartment were assessed using a two tailed t-test. Site and bone comparisons were made with a repeated measures ANOVA based on a generalized linear effect model (GLM) framework and the use of Gaussier-Glass corrections for non-homogeneous data. Results are summarized as the mean +/- the standard deviation for each compartment and metric. Factor effects and contrasts (which represents direct comparisons between data grouped as site or treatment) are shown, the interaction term was not significant and is not shown. Where relevant, the non-normal and non-homogenous data is annotated. All values of $p < 0.05$ are considered significant, values of $p < 0.1$ are noted as trends.

3.3 Results

3.3.1 Mineral Apposition Rate and Total Mineral Density (TMD) are Anatomical Site-dependent

To study the effect of collagen cross-link alteration on mineral quantity and composition, the model of BAPN administration for LOX inhibition was chosen. Areas of interest included rapidly growing regions of tissue to maximize the effects of BAPN. In addition to the underlying compositional questions, the comparison of anatomical site (specifically craniofacial and long bones) was undertaken to investigate differential perturbations to mineral and matrix composition that are common in a variety of systemic disease conditions[30][3][31]. The mice in this study had a significant reduction (Welch's t-test, p=0.010) in body weight due to BAPN

administration[22]. However, there was no significant difference in bone weight with treatment (Table 3.2).

Both the mandible and femur contained areas of high- and low- mineral apposition rate (MAR) (Figure 3.1), allowing for direct comparison of MAR dependent effects of cross-link inhibition via BAPN treatment. There was no significant effect of BAPN treatment on MAR, therefore the combined mean values of both treatments are presented and analyzed. The regions of interest are highlighted in Figure 3.1A with the study design and timing of fluorophore injections (Figure 3.1B). Typically, the femur would not be considered to have an area of high-MAR, however, the cortical region at the distal epiphysis was primarily new tissue after the 21 days of this study due to the mice being young, growing mice (5.95 ± 1.25 μm/day, Figure 3.1C). Likewise, the interradicular bone of the first molar (2.44 ± 0.43 μm/day, Figure 3.1C) had a relatively high-MAR. The trabecular compartment of the distal epiphysis of the femur (1.77 ± 0.33 μm/day, Figure 3.1C) as well as the mandibular buccal cortical near the first molar (1.33 ± 0.28 μm/day, Figure 3.1C) showed areas of lower-MAR. Each site was significantly different than the other except for the femoral trabecular vs. mandibular cortical comparisons (GLM, $p<0.0001$, Figure 3.1C).

Mineral quantity was assessed via micro-CT at each volume of interest. TMD was highest in the cortical compartments of both bones, with the control group buccal cortex of the mandible having a significantly higher TMD (1215.41 ± 30.730 mg HA/cm^3, Figure 3.2A) than the femoral cortex (1118.00 ± 20.07 mg HA/cm^3, Figure 3.2A), interradicular bone of the mandible (1068.88 ± 18.6 mg HA/cm^3, Figure 3.2A), and the femoral trabecular bone (835.45 ± 32.00 mg HA/cm^3, Figure 3.2A). No effects of BAPN on any micro-CT parameter were observed in either bone or compartment (Table 3.3S) except for the BMD of the femur (GLM contrast for treatment, $p = 0.031$, Table 3.3S). The individual t-tests for each site revealed a trend towards decreased BMD with BAPN treatment in the femoral cortex (Welch's t-test, $p = 0.095$, Figure 3.2B). Each site was significantly different from every other site for BMD and TMD (GLM, $p<0.0001$, Figure 3.2 A&B).

3.3.2 Tissue Level Young's Modulus and Hardness Were Higher Mandible as Compared to the Femur but Were Not Altered by BAPN Treatment

The femoral cortex exhibited significantly higher modulus (10.92 ± 3.99 GPa, Figure 3.2C) and hardness (0.67 ± 0.23 GPa, Figure 3.2C) compared to the trabecular compartment (modulus: 5.97 ± 3.80 GPa, Figure 3.2C, hardness: 0.42 ± 0.20 GPa, Figure 3.2D). Both mandibular cortex (modulus: 16.68 ± 1.96 GPa, Figure 3.2C, hardness: 0.969 ± 0.125 GPa, Figure 3.2D) and interradicular bone (modulus: 17.635 ± 2.87 GPa, Figure 3.2, hardness: 0.937 ± 0.14 GPa, Figure 3.2D) exhibited significantly higher tissue level mechanical metrics compared to the femur (GLM, $p < 0.001$, Figure 3.2 C&D) yet did not differ from each other. No significant effect of BAPN was found on tissue level Young's modulus or hardness.

3.3.3 Collagen Cross-links Differ Between the Mandible and Femur and are Altered Differently with BAPN Treatment

Direct measures of collagen cross-links from whole hemimandibles and femora revealed significant compositional differences between bones (Table 3.2). The metrics presented are for the whole, homogenized bones, therefore site comparisons (cortical vs. trabecular) were not able to be made. Mandibles exhibited significantly higher collagen content (48.89 ± 13.96 mol collagen/mg whole bone weight) than femora (31.26 ± 12.13 mol collagen/mg) (GLM, $p = 0.012$, Table 3.2) with no significant effect of BAPN treatment. Pyrrolic cross-links were almost twice as high in the mandible (0.820 ± 0.31 mol/mol collagen) compared to the femur (0.465 ± 0.13 mol/mol collagen)(GLM, $p<0.002$, Figure 3.3B). Total mature cross-links were also significantly higher in the mandible (Pyr+PYD+DPD) (GLM, $p<0.003$, Figure 3.3B) but not the pyridinolines individually (Figure 3.3A). The (PYD+DPD)/Pyr ratio was significantly increased in the femur (0.065 ± 0.03 mol/mol collagen) compared to the mandible (0.007 ± 0.001 mol/mol collagen) (GLM, $p = 0.019$, Table 3.2).

Immature cross-links were significantly higher in the femur (0.803 ± 0.04 mol/mol collagen) than in the mandible (0.546 ± 0.21 mol/mol collagen) (GLM, $p = 0.014$, Figure 3.3C), predominantly driven by DHLNL content (GLM, $p = 0.011$, Figure 3.3C) of which the femur contained approximately 30% more DHLNL mol/mol collagen than the mandible. The

DHLNL/HLNL ratio was also significantly increased in the femur (4.34 ± 1.00 mol/mol collagen) compared to the mandible (3.70 ± 0.40 mol/mol collagen) (GLM, p = 0.041, Table 3.2).

Ratios of the mature to immature cross-links also showed significant differences between bones. The mandible contained significantly more mature/immature cross-links as calculated via the ratios: PYD/(DHLNL+HLNL), (PYD+DPD)/(DHLNL+HLNL), (PYD+DPD+Pyr)/(DHLNL+HLNL) (GLM, p<0.0001 for all three ratios, Table 3.2).

The advanced glycation end product, carboxymethyl-lysine (CML), was directly detected here in mouse bone for the first time. There was significantly increased CML in the mandible (0.282 ± 0.21 mol/mol collagen) compared to the femur (0.013 ± 0.004 mol/mol collagen) (GLM, factor effect p <0.0001 for bone effects, Figure 3.3D). No significant differences in PEN were detected between bones (Figure 3.3D).

BAPN caused a significant decrease in the PYD (Welch's t-test, p = 0.038, Figure 3.4A), DPD (Welch's t-test, p = 0.032, Figure 3.4B), and PYD+DPD of the mandible (Welch's t-test, p = 0.028, Figure 3.4C), but not the femur. While immature cross-links were not significantly altered by BAPN, there was a significant factor effect (GLM, factor effect p = 0.044 for BAPN effects, Table 3.2) in HLNL content for both bones and trends (GLM, factor effect p = 0.094 and p = 0.075 for BAPN effects, Table 3.2) towards decreased levels of both immature cross-links.

3.3.4 BAPN Causes Mineral Differences in the Femur and Matrix Differences in the Mandible

The comparison of the mandible and femur also highlighted mineral and matrix differences between these anatomical sites as measured via Raman spectroscopy (Figure 3.5 A-F, Table 3.3S). The largest site-specific matrix differences existed in the amide I (1660 cm^{-1}/1694 cm^{-1}) band with the highest values in the femoral cortex (7.18 ± 1.75 cm^{-1}/ cm^{-1}) and trabecular bone (3.50 ± 0.67 cm^{-1}/ cm^{-1}) compared to the mandibular interradicular bone (3.28 ± 0.33 cm^{-1}/ cm^{-1}) and cortex (2.18 ± 0.64 cm^{-1}/ cm^{-1}) (GLM, p < 0.0001, Figure 3.5A). Hydroxyproline/proline ratio (874 cm^{-1} /854 cm^{-1} cm^{-1}), hydroxyproline+proline (874 cm^{-1} + 854

cm^{-1} cm^{-1}) ($p = 0.035$) and amide III (1240 cm^{-1}/1263 cm^{-1}) also were significantly different between sites (GLM, $p < 0.001$, Figure 3.5F).

Mineral to matrix differences were seen in numerous Raman band parameters, including mineral/phenylalanine (960 cm^{-1}/1001 cm^{-1}) (Figure 3.5B), mineral(hydroxyproline+proline) (960 cm^{-1}/ (874 cm^{-1} + 854 cm^{-1} cm^{-1})), mineral/amide I (960 cm^{-1}/1660 cm^{-1}), and carbonate/amide I (1069 cm^{-1}/1660 cm^{-1}) (GLM, $p < 0.0001$, Table 3.3S). Mineral differences included crystallinity (1/FWHM of 960 cm^{-1}) (Figure 3.5C), carbonate/phosphate (1048 cm^{-1}/960 cm^{-1}) (Figure 3.5D) (GLM, $p < 0.0001$).

BAPN increased carbonate/phosphate ratios in the femoral cortex (Welch's t-test, p=0.019, Figure 3.5C) and decreased the hydroxyproline/proline ratio in the femoral trabecular compartment (Welch's t-test, p=0.012, Figure 3.5F). BAPN caused a decrease in the Amide III (1240 cm-1/1263 cm-1) in the mandibular buccal cortex (Welch's t-test, p=0.024, Figure 3.5E).

3.4 Discussion

While methods of direct measures of collagen cross-links can be cumbersome, the advances in LC-MS technology have alleviated some of the technical burden, expanding the detectability of some species. To my knowledge, this is the first report of directly measurable CML in mouse bone, as well as the first report of bone specific accumulation of CML (Figure 3.3 D). Direct measures of CML in human bone have only recently been reported[16]. Additionally, the trend (Welch's t-test, $p = 0.127$, Table 3.2) towards increasing CML with BAPN treatment begs the question of compensation or direct effect of LOX, both of which are beyond the scope of this study. The mandible also has a lower immature cross-link content, which has the same hydroxylysine formation site as AGE's and therefore negatively competes with AGE formation, unlike the mature cross-links[16]. This competitive formation of the cross-links could explain why less CML accumulation is seen in the femur (high immature cross-links content). It is plausible to hypothesize that there are unknown mechanisms (cell source dependent, bone formation rate dependent, or exercise/loading dependent) driving preferential formation of CML over immature cross-links in the mandible. Site-specific cross-link formation may render diseases that affect bone composition to be anatomic site dependent.

My hypothesis focused on anatomical and mineral apposition rate dependent changes to mineral with perturbed collagen cross-linking. However, site dependent changes to mineral (Figure 3.2, Figure 3.5, Table 3.2) do not appear to be driven by differences in mineral apposition rate (Figure 3.1) and are more dependent on the mature/immature collagen cross-link profile (Figure 3.3, Table 3.2). This work highlights that bone composition is not "one size fits all" -- that site specific compositional differences exist for both mineral and collagen which is consistent with other reports[32][33]. Compared to the femora, the mandible exhibits higher crystallinity, lower carbonation, higher mature collagen cross-links and mature/immature ratios, higher CML content (first report in mouse bone as well as first report of bone specific accumulation), and higher tissue level strength and stiffness (Table 3.2 & Table 3.3S). The implications of these results extend beyond the findings of compositional differences between anatomical sites. These results also show how altered collagen compositions can drive changes in mineral composition dependent on anatomical site, which could ultimately disrupt function and response to repeated loading. While traditional logic may point to these changes being MAR dependent, we studied the cortical compartment of the femur and the interradicular bone of the mandible (both with high-MAR) as well as the cortex of the mandible and the trabecular bone of the femur (both with low-MAR) (Figure 3.1C) to investigate the dependence of composition on MAR. However, mineral and matrix compositional changes varied more with anatomical site than MAR.

When cross-links are perturbed via BAPN inhibition of enzymatic cross-link formation, the matrix changes (decreased amide III bands) in the mandible are apparent via Raman spectroscopy (Figure 3.5E) as well as via direct LC-MS measures (deceased PYD and DPD) (Figure 3.4 A&B). Yet, no significant alteration of mineralization or tissue level mechanics (Figure 3.2 A-D) was detected in the mandible. The femur underwent less matrix changes with BAPN treatment (Figure 3.4 A-D), yet a significant increase in carbonation occurred (Figure 3.4D), but without alteration to the modulus or hardness (Figure 3.2 C&D).

This study design of targeting collagen cross-link effects on mineralization allows for investigation of the relationship of altered collagen to the carbonate band. An increase in carbonate/phosphate is negatively correlated with fracture toughness and tissue level mechanics[34] and associated with increased fracture risk[35]. I similarly observed a reduced

modulus and hardness (Figure 3.2 C&D) with increased carbonation in the femur as compared to the mandible (Figure 3.5D). In my original hypothesis, I suggested that there would be a site and MAR mineralization dependence. Yet, since both the femur cortical compartment and the mandibular interradicular bone had high-MAR but only the femur cortex exhibited increased carbonate/phosphate ratios with BAPN treatment, this could not dependent on MAR. I now suggest that bones with a higher immature/mature cross-link ratio (such as the femur) may be more susceptible to altered mineralization, independent of MAR.

Few studies have compared mineral and collagen compositional differences between anatomical sites, and even less have compared craniofacial and long bones. This study found that BAPN inhibition of LOX resulted in an altered enzymatic cross-link profile that is site dependent. Thus, disruption of cross-links is not only BAPN dose dependent[22], but also anatomical site dependent. The mature enzymatic cross-link profile was significantly reduced in the mandible, but not the femur (Figure 3.4 A-C). The femur was previously shown to have a reduction in PYD and DPD with the same BAPN dose[22], while here there are trends toward decreased PYD and DPD (Figure 3.3A). The current LC-MS method uses exact mass to four decimal places instead of fluorescence, and therefore the results may be slightly different from conventional HPLC. While BAPN is an established model of enzymatic cross-link inhibition[22][20][21] this study highlights the importance of direct measures of cross-links in different bones when testing whether a treatment or disease alters the cross-link profile.

Numerous collagen compositional differences exist between the mandible and femur. Highlighted in this work are the significantly increased collagen content, mature/immature ratio, CML, and pyrrolic cross-links in the mandible compared to the femur (Figure 3.3B and Table 3.2). This mouse data comparing the mandible to the femur is similar to human data showing that the mandible has higher mineral content, collagen content, and decreased lysyl hydroxylation[12]. An explanation for these compositional differences could be the bone formation rate (though not measured here) which is known to be increased in the mandible[36] as well as the exercised femur[37], both of which correspond to increased mature/immature and pyrrolic cross-links[20]. The effects of BAPN inhibition of enzymatic cross-links are also more pronounced in the mandible, with a significant decrease in the PYD and DPD cross-links with treatment (Figure 3.3 A&C, Table 3.2) and a corresponding decrease in the amide III matrix band in the mandible

cortex (Figure 3.5E). Yet, no mineral differences were detected in the mandible with BAPN treatment (Figure 3.5 B-D). The bone-dependent compositional response to systemic BAPN highlights that anatomical site comparisons are warranted and that there may be altered responses to a variety of perturbations (such as mutations or drug treatment) between these sites if mineral or collagen is affected. It is still unknown if the bone-dependent compositional changes are purely due to cells of origin, mechanical loading, or other factors. Additionally, this study focuses on cross-link depleted tissue during normal growth over a short time period (21 days) – essentially homeostatic conditions. It is also important to understand how cross-links affect tissue during periods of rapid bone deposition like osseous wound healing.

Collagen cross-links may "pre-destine" a site for mineralization[18]. While not explicitly confirmed in this study, my data provides evidence that altering the cross-link profile can alter mineralization (carbonate/phosphate ratios), at least in the growing distal femora (Figure 3.5D). In contrast, the cross-link profile was significantly altered in the mandible (Table 3.2, Figure 3.4 A-C), yet no changes to the mineralization pattern were observed (Table 3.3S). Therefore, I suggest that a lower matrix maturity ratio may be required for collagen cross-link mediated alteration in mineralization.

3.5 Conclusions

This study reveals that both mineral and collagen composition, including the newly detected CML cross-link, has an anatomical dependence and there is a differential response of these sites to collagen cross-links perturbation via BAPN treatment. In the femur, carbonate/phosphate increased with BAPN treatment whereas in the mandible this metric did not change. BAPN related matrix changes (both the amide III and the mature cross-links) were more pronounced in the mandible compared to the femur. The mandible and the femur also exhibited different collagen cross-link profiles, mineralization patterns, and tissue level mechanical properties – which highlights the importance of investigating multiple anatomical sites for bone compositional changes with disease or drug treatment.

3.6 Acknowledgements

I would like to thank the co-authors who contributed to this work: Aidan Terhune, Benjamin Bielajew, Michelle Lynch, Gurjit Mandair, Erin McNerny, and David H. Kohn. I would like to thank Dr. Wendy Feng for advice on the LC-MS processing and analysis via the Natural Products Core. Research reported in this publication was supported by the National Institutes of Health NIDCR T32 DE007057, F30 DE028167. Research reported in this publication was also supported by the National Institutes of Health NIAMS P30 AR069620 (Dr. Ken Kozloff, Nanoindentation) and R01 AR065424, R01 AR068452. The micro-CT core at the Michigan School of Dentistry is funded in part by NIH/NCRR S10RR026475-01. Research reported in this publication was also supported by the University of Michigan School of Dentistry (Dean's Scholarship and Natalie C. Roberts Endowed Professorship). The content is solely the responsibility of the authors and does not necessarily represent the official views of the National Institute of Health or the University of Michigan School of Dentistry.

3.7 Author Contributions

Study design: GR, EM and DK. Study conduct: GR, BB, AT and EM. Data collection: GR and AT. Data analysis: GR, GM, AT and ML. Data interpretation: GR, GM, ML and DK. Drafting manuscript: GR. Revising manuscript content: GR and DK. Approving final version of manuscript: GR, AT, BB, EM, GM, ML, and DK. GR and DK take responsibility for the integrity of the data analysis.

Table 3.1 Cross-links of interest with respective chemical formulas, molecular mass, and accurate masses of [M+H]+ charged ions of cross-links. Key: Pyridoxine is the internal standard. Mature cross-links (pyridinoline (PYD), deoxypyridinoline (DPD)), immature cross-links (dihydroxylysinorleucine (DHLNL)), and advanced glycations end products (such as pentosidine (PEN) and carboxy methyl-lysine (CML)).

Crosslinks	Formula	Mass (g/mol)	$[M+H]^+$
Pyridoxine	$C_8 H_{11} N O_3$	169.180	170.081
HLNL	$C_{12} H_{25} N_3 O_5$	291.348	292.187
DHLNL	$C_{12} H_{25} N_3 O_6$	307.347	308.182
PYD	$C_{18} H_{28} N_4 O_8$	428.437	429.198
DPD	$C_{18} H_{28} N_4 O_7$	412.433	413.203
PEN	$C_{17} H_{26} N_6 O_4$	378.430	379.209
CML	$C_8 H_{16} N_2 O_4$	204.224	205.118

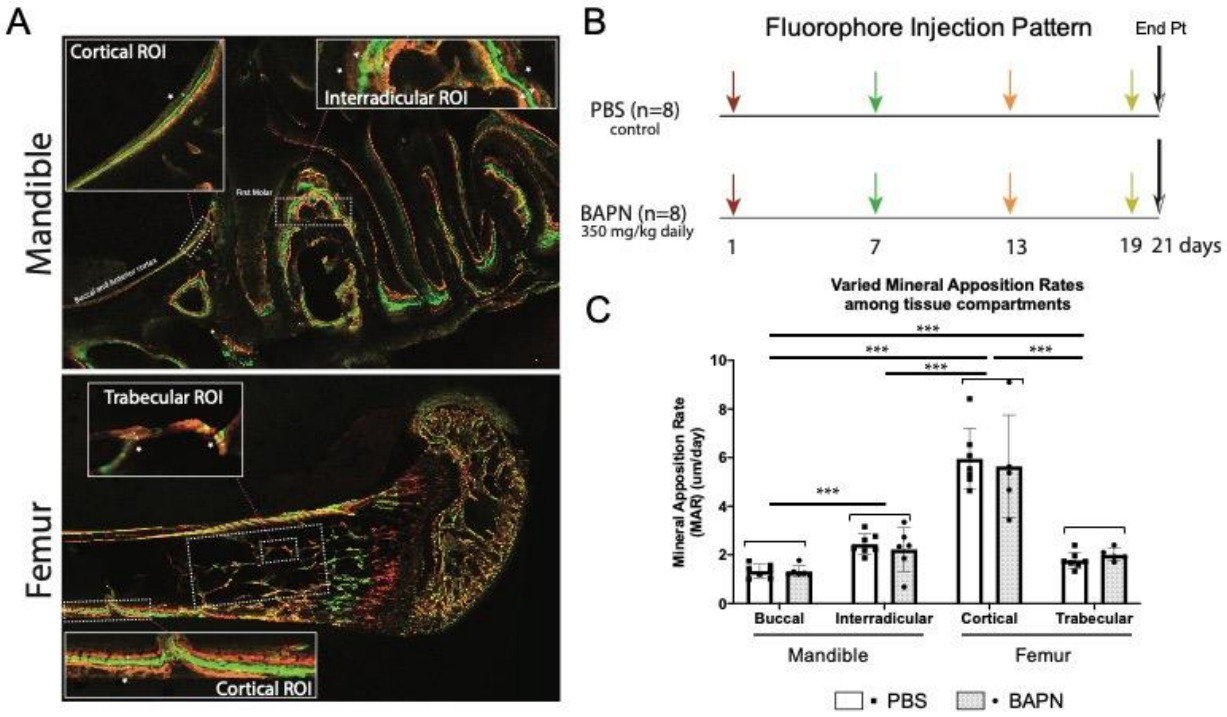

Figure 3.1 Dynamic histomorphometry of the mandible and femur. (A) Fluorescent images of longitudinally sectioned mouse femur showing cortical bone and trabecular bone ROIs for analysis via dynamic histomorphometry, nanoindentation and Raman spectroscopy. Fluorescent images of longitudinally sectioned mandible showing the first molar and the buccal cortical and interradicular bone of the first molar ROI's used for the same analyses as were conducted in the femur. (B) Schematic of the four fluorophores delivered at weekly injections, indicating tissue growth during treatment, and highlighting the area used for analyses. (C) Mineral apposition rate was significantly different between each compartment ($p<0.0001$, designated as ***)(All values from Generalized Linear Model (GLM)).

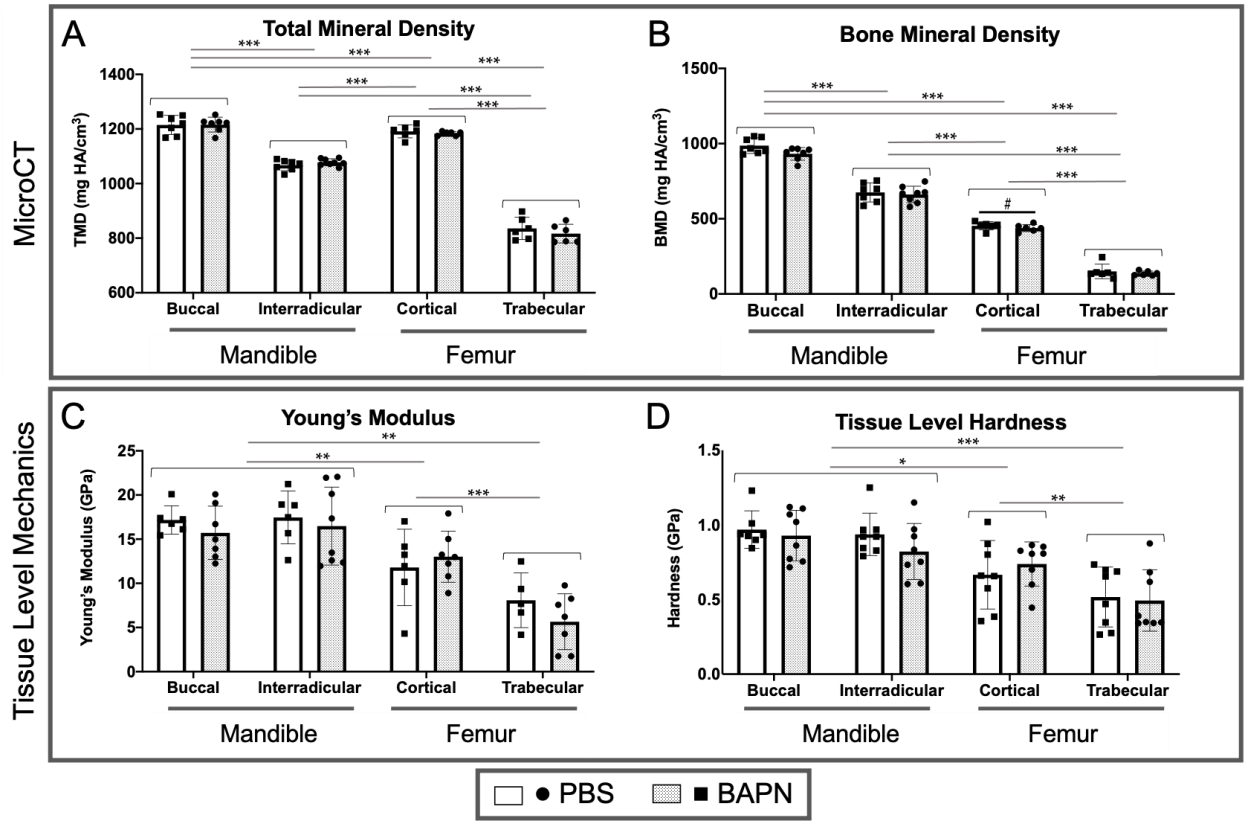

Figure 3.2 MicroCT and tissue level mechanics between bone compartments. (A) Total mineral density (TMD) was significantly different between every site ($p<0.0001$), with decreasing TMD from mandible to femur, with respective cortical site higher than woven bone counterparts. (B) Bone mineral density (BMD) was significantly decreased between sites, with the mandible having higher BMD than the femur ($p<0.0001$). (C) Young's modulus varied between bones and sites within the femur. The mandible had a higher modulus than both the femur cortical and trabecular compartments ($p<0.001$, or as designated) and the femur cortex had a higher modulus than the femur trabecular bone ($p<0.001$). (D) The same trend was seen with the hardness values ($p<0.05$, or as designated). No significant effects of treatment were seen in TMD, BMD, modulus or hardness.

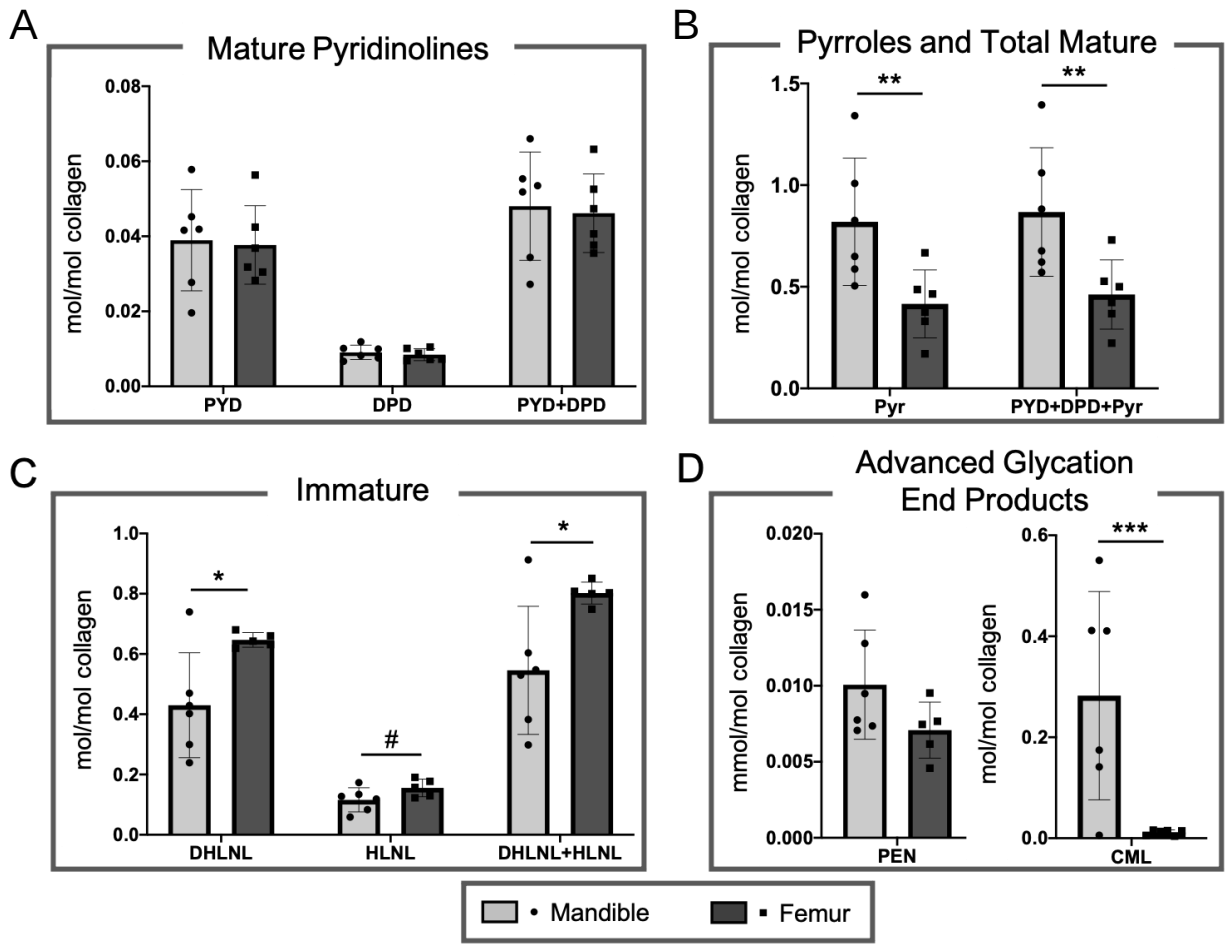

Figure 3.3 Differences in collagen cross-link profiles between bones. (BAPN groups excluded for clarity) (A) Mature pyridinoline collagen cross-links did not vary between bones ($p>0.18$). (B) Pyrrolic cross-links ($p=0.002$) as well as the sum of all mature cross-links ($p=0.003$) were significantly higher in the mandible compared to the femur. (C) Immature cross-links were significantly decreased in the mandible compared to the femur (DHLNL, $p=0.010$)(HLNL, $p=0.067$)(DHLNL+HLNL, $p=0.014$). (D) No change in pentosidine (PEN) was measured ($p=0.108$), between bones, however, there were significantly increased levels of carboxymethyl-lysine (CML) in the mandible compared to the femur ($p<0.0001$).

Table 3.2 Direct measures of collagen cross-link profile from mandibles and femurs as measured by LC-MS.

	Mandible			Femur			Factor Effects (a) (within subject)		
Site	**PBS**	**BAPN**	***p-value***	**PBS**	**BAPN**	***p-value***	**Bone**	**BAPN**	**Sig.**
Mature crosslinks									
Pyrroles (Pyr)	0.820 ± 0.31	0.700 ± 0.21	0.486	0.465 ± 0.13	0.468 ± 0.11	0.962	**0.002**	0.711	**
Hydroxylyslpyridinoline (PYD)	**0.039 ± 0.01**	**0.024 ± 0.004**	**0.038**	0.037 ± 0.01	0.046 ± 0.03	0.518 +	0.184	0.663	*
Lyslpyridinoline (DPD)	**0.009 ± 0.002**	**0.007 ± 0.001**	**0.032**	0.008 ± 0.002	0.008 ± 0.003	0.838	0.693	0.071#	*
Pyr + PYD + DPD	0.868 ± 0.32	0.730 ± 0.21	0.428	0.510 ± 0.14	0.523 ± 0.12	0.872	**0.003**	0.675	**
PYD + DPD	**0.048 ± 0.01**	**0.030 ± 0.005**	**0.028**+	0.045 ± 0.01	0.054 ± 0.03	0.554 +	0.199	0.555	*
Immature cross-links									
Dehydroxylyslnoroluceine (DHLNL)	0.430 ± 0.17	0.305 ± 0.09	0.185	0.648 ± 0.03	0.511 ± 0.28	0.364	**0.011**	0.094#	*
Hydroxylyslnoroluceine (HLNL)	0.116 ± 0.04	0.080 ± 0.03	0.138	0.155 ± 0.03	0.112 ± 0.06	0.253	0.067#	**0.044**	*
DHLNL + HLNL	0.546 ± 0.21	0.386 ± 0.12	0.172	0.803 ± 0.04	0.623 ± 0.33	0.325	**0.014**	0.075#	*
Cross-link Ratios									
DHLNL/HLNL	3.70 ± 0.40	3.86 ± 0.34	0.322	4.34 ± 1.00	4.90 ± 1.42	0.539	**0.041**	0.3	*
PYD/(DHLNL+HLNL)	0.072 ± 0.008	0.063 ± 0.009	0.111	0.040 ± 0.003	0.044 ± 0.009	0.381 +	**< 0.0001**	0.327	***
DPD/(DHLNL+HLNL)	0.007 ± 0.0008	0.006 ± 0.0009	0.727	0.007 ± 0.001	0.006 ± 0.001	0.359	0.614	0.08#	#
(PYD+DPD)/Pyr	0.065 ± 0.03	0.046 ± 0.02	0.293	0.099 ± 0.02	0.124 ± 0.09	0.575	**0.019**	0.62	*
PYD/DPD	4.32 ± 1.49	3.60 ± 0.40	0.322	4.69 ± 1.99	5.38 ± 2.32	0.615	0.162	0.974	
(PYD+DPD)/(DHLNL+HLNL)	0.090 ± 0.011	0.081 ± 0.011	0.187	0.050 ± 0.005	0.055 ± 0.011	0.396	**< 0.0001**	0.445	***
(PYD+DPD+Pyr)+(DHLNL+HLNL)	1.41 ± 0.376	1.12 ± 0.230	0.158	1.26 ± 0.097	1.12 ± 0.352	0.476	0.503	0.135	
(PYD+DPD+Pyr)/(DHLNL+HLNL)	1.75 ± 0.662	2.01 ± 0.657	0.525	0.57 ± 0.084	1.01 ± 0.605	0.198	**< 0.0001**	0.154	***
Advanced Glycation End Products (AGE's)									
Pentosidine (PEN) (mmol/mol collagen)	0.0101 ± 0.0036	0.0086 ± 0.0024	0.453	0.0077 ± 0.0014	0.0077 ± 0.0021	0.966	0.108	0.699	
Carboxymethyl-lysine (CML)	0.282 ± 0.21	0.254 ± 0.09	0.766+	0.013 ± 0.004	0.054 ± 0.054	0.127 +	**< 0.0001**	0.893	***
Whole bone									
Mineralized weight	0.018 ± 0.002	0.018 ± 0.002	0.646	0.018 ± 0.005	0.016 ± 0.003	0.521	0.699	0.422	
Collagen/mineralized weight	48.89 ± 13.96	41.32 ± 8.80	0.266	31.26 ± 12.13	32.60 ± 9.30	0.84	**0.012**	0.466	*

(a) Repeated measures ANOVA for main effects; Interaction term was not significant and is not shown. Subsequent t-test for site specific treatment effects. Factor effect as marginal #($p < 0.1$), or significant *($p<0.01$), **($p<0.001$), ***($p<0.0001$), +(uneaqual variance)

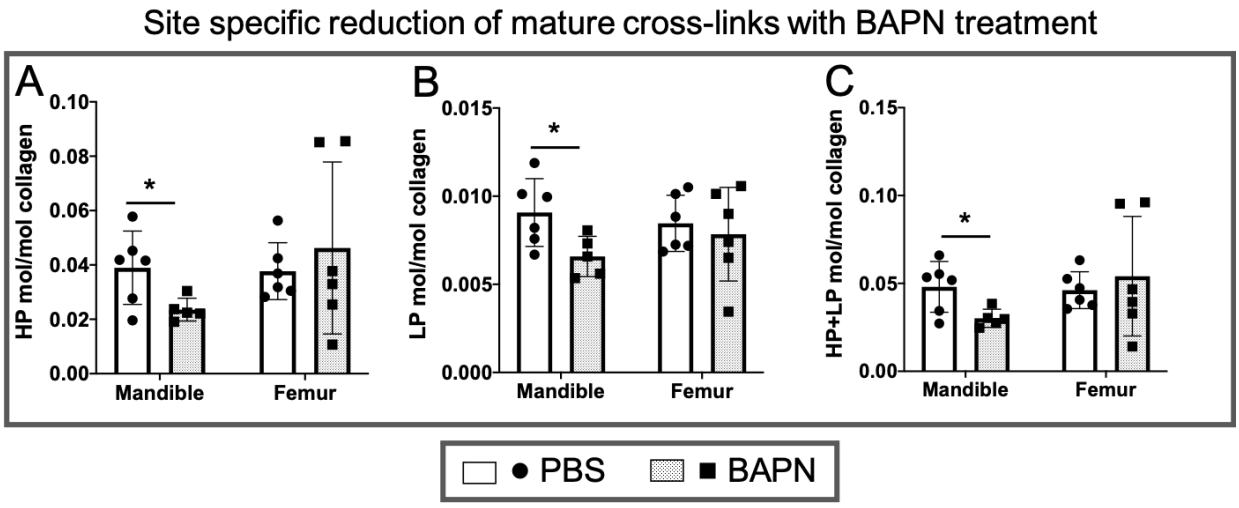

Figure 3.4 BAPN significantly reduced the mature cross-links in the mandible but not the femur. (A) PYD cross-links were significantly reduced with BAPN treatment in the mandible but not the femur (p=0.038). The same was seen for (B) DPD cross-links (p=0.032) and (C) for the sum of the total mature pyridinoline cross-links (PYD+DPD) (p=0.028).

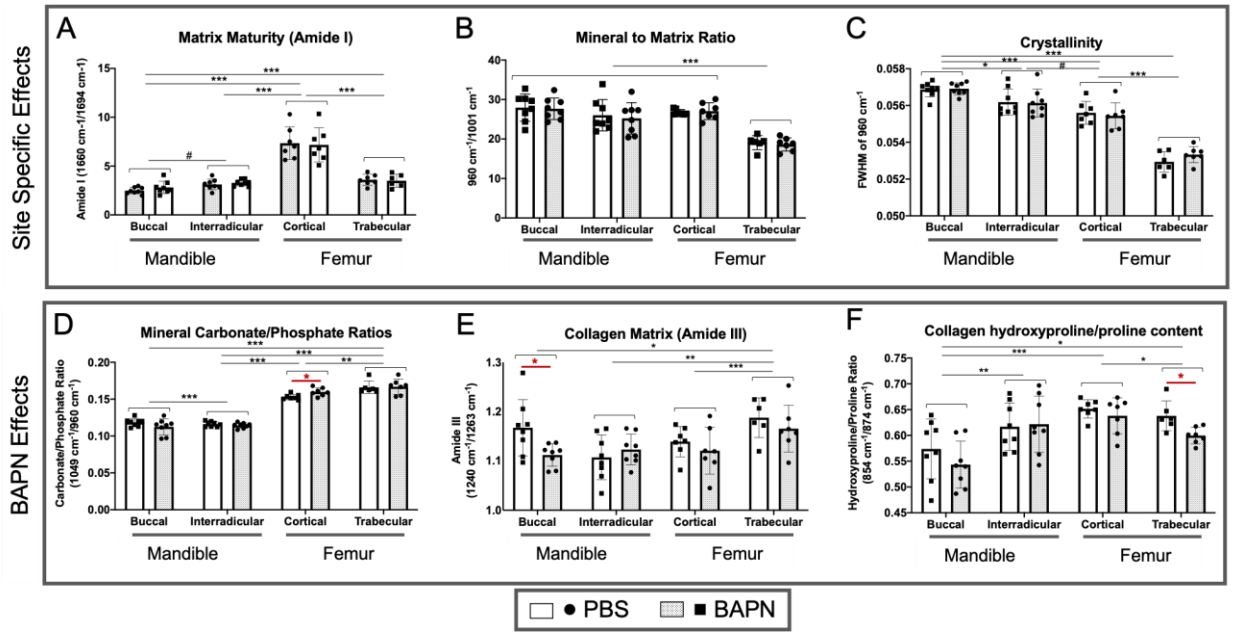

Figure 3.5. Numerous site-specific compositional differences between the mandible and femur were seen in mineral and matrix as measured via Raman Spectroscopy. (A) The matrix maturity (Amide 1) was significantly different between each site except the mandible cortex and interradicular bone ($p<0.0001$). (B) The mineral to matrix ratio was significantly lower in the femoral trabecular bone compared to every other compartment ($p<0.0001$). (C) Mineral crystallinity was significantly different in every compartment except the interradicular bone of the mandible and the femoral cortical bone ($p<0.05$ or as indicated). (D) Carbonate/phosphate ratios differed significantly between compartments ($p<0.0001$ or as indicated), with higher carbonation in the femur than the mandible. BAPN significantly increased carbonate/phosphate in the femur cortex ($p = 0.019$). (E) The amide III ratio was significantly higher in the femoral trabecular bone than any other compartment ($p<0.05$ or as indicated). Amide III was significantly reduced in the mandible buccal cortex with BAPN treatment ($p=0.024$). (F) Hydroxyproline/proline content was significantly lower in the mandible buccal cortex compared to the other sites ($p<0.05$ or as indicated), as well as the femur trabeculae as compared to the femur cortex ($p<0.05$). BAPN significantly reduced the hydroxyproline/proline ratio in the femur trabeculae ($p=0.012$).

Table 3.3S Supplemental summary table of tissue level mechanical data, histomorphometry, and MicoCT.

	Mandible						**Femur**									
	Buccal Cortical			**Interradicular Alveolar**			**Cortical**			**Trabecular**			**GLM Factor Effects**	**Differences in**	**Differences in**	
Site	**PBS**	**BAPN**	***p-value***	**PBS**	**BAPN**	***p-value***	**PBS**	**BAPN**	***p-value***	**PBS**	**BAPN**	***p-value***	**Site**	**Site**	**BAPN**	**Sig.**
Raman Matrix Parameters																
Hydroxyproline/Proline Ratio (874 cm^{-1}/854 cm^{-1})	0.574 ± 0.058	0.543 ± 0.046	0.26	0.618 ± 0.046	0.622 ± 0.055	0.848	0.652 ± 0.018	0.638 ± 0.035	0.386+	**0.638 ± 0.029**	**0.600 ± 0.016**	**0.012***	**< 0.0001**	**0.047**	0.144	***
Hydroxyproline + Proline (874 cm^{-1} + 854 cm^{-1})	0.097 ± 0.016	0.095± 0.009	0.778+	0.086 ± 0.009	0.091± 0.015	0.401	0.090 ± 0.007	0.092 ± 0.004	0.576	0.092 ± 0.008	0.101 ± 0.008	0.083#	**0.035**	0.418	0.235	*
Amide I (1660 cm^{-1}/1694 cm^{-1})	2.813± 0.636	2.485± 0.336	0.218	3.283 ± 0.327	3.115± 0.542	0.465	7.18 ± 1.75	7.35 ± 1.67	0.853	3.50 ± 0.67	3.599 ± 0.555	0.773	**< 0.0001** ^	**< 0.0001** ^	0.883 ^	***
Amide I (1660 cm^{-1}/1679 cm^{-1})	1.704 ± 0.094	1.642 ± 0.153	0.343	1.688 ± 0.128	1.689 ± 0.066	0.998	1.75 ± 0.10	1.74 ± 0.05	0.835	1.64 ± 0.17	1.677 ± 0.122	0.686	0.227	0.353	0.38	
Amide III (1240 cm^{-1}/1263 cm^{-1})	**1.167 ± 0.057**	**1.112 ± 0.023**	**0.024***	1.107 ± 0.045	1.123 ± 0.031	0.43	1.14 ± 0.031	1.121 ± 0.047	0.406	1.188 ± 0.040	1.165 ± 0.047	0.385	**< 0.001**	0.108	0.342	**
Raman Mineral Parameters																
Mineral/Hydroxyproline (960 cm^{-1}/874 cm^{-1})	28.623 ± 3.571	30.461 ± 3.102	0.290	27.831 ± 4.088	27.497 ± 3.026	0.855	28.33 ± 2.13	28.05 ± 1.69	0.793	28.23 ± 2.33	26.38 ± 1.87	0.139	0.306	0.85	0.757	
Mineral/(Hydroxyproline+Proline) (960 cm^{-1}/(874 cm^{-1} + 854 cm^{-1}))	10.596 ± 1.384	10.607 ± 1.0211	0.986	11.080 ± 1.257	11.340 ± 2.058	0.594	11.15 ± 0.89	10.85 ± 0.47	0.451	10.85 ± 0.94	9.93 ± 0.71	0.068#	**0.021**	0.162	0.166	*
Mineral/Phenylalanine(960 cm^{-1}/1001cm^{-1})	27.957 ± 3.438	27.666 ± 2.725	0.854	26.029 ± 3.980	25.239 ± 3.977	0.697	26.76 ± 0.73	27.062 ± 2.14	0.731+	19.08 ± 1.78	18.63 ± 1.67	0.653	**< 0.0001**	0.127	0.706	***
Mineral/Amide I (960 cm^{-1}/1660 cm^{-1})	11.259 ± 2.230	11.491 ± 1.908	0.826	11.442 ± 1.257	11.590 ± 1.511	0.834	12.99 ± 1.33	12.96 ± 1.08	0.971	9.87 ± 0.62	9.47 ± 0.74	0.320	**< 0.0001**	0.149	0.397	***
Crystallinity (1/ FWHM at 960 cm^{-1})	0.057 ± 0.0004	0.057 ±0.0003	0.833	0.056 ± 0.0007	0.056 ± 0.0008	0.900	0.056 ± 0.0006	0.055 ± 0.0007	0.658	0.053 ± 0.0006	0.053 ± 0.0004	0.183	**< 0.0001**	**< 0.0001**	0.968	***
Carbonate/Phosphate (1069 cm^{-1}/960 cm^{-1})	0.118 ± 0.005	0.112 ± 0.011	0.184	0.116 ± 0.004	0.114 ± 0.004	0.312	**0.153 ± 0.004**	**0.160 ± 0.006**	**0.019***	0.166 ± 0.008	0.167 ± 0.010	0.870	**< 0.0001**	**< 0.0001**	0.949	***
Carbonate/Amide I (1069 cm^{-1}/1660 cm^{-1})	1.331 ± 0.255	1.333 ± 0.240	0.992	1.335 ± 0.178	1.327 ± 0.188	0.936	1.99 ± 0.21	2.08 ± 0.19	0.418	1.64 ± 0.16	1.57 ± 0.13	0.313	**< 0.0001**	**< 0.0001**	0.643	***
Mechanical Data (Nanoindentation)																
Modulus (GPa)	17.17 ± 1.61	15.72 ± 3.01	0.675	17.46 ± 2.99	16.48 ± 4.42	0.545	11.80 ± 4.33	13.01 ± 2.90	0.403	8.08 ± 3.10	6.30 ± 2.91	0.759	**< 0.0001**	**< 0.0001**	0.839	***
Hardness (Gpa)	0.97 ± 0.13	0.93 ± 0.17	0.612	0.94 ± 0.14	0.82 ± 0.19	0.189	0.67 ± 0.23	0.74 ± 0.15	0.465	0.52 ± 0.20	0.49 ± 0.21	0.821	**< 0.0001**	**< 0.001**	0.873	***
Histomorphometry																
Mineral Apposition Rate (μm/day)	1.333 ± 0.278	1.317 ± 0.229	0.911	2.438 ± 0.431	2.221 ± 0.902	0.581	5.95 ± 1.25	5.64 ± 2.11	0.757	1.77 ± 0.33	2.00 ± 0.26	0.225	**< 0.0001** ^	**< 0.0001** ^	0.646	***
Micro-CT																
Bone volume/Total volume (BV/TV)	0.840 ± 0.048	0.803 ± 0.050	0.098#	0.671 ± 0.05	0.649 ± 0.058	0.344	0.365 ± 0.018	0.355 ± 0.018	0.235	0.1678 ± 0.062	0.152 ± 0.021	0.42	**< 0.0001** ^	**< 0.0001** ^	0.091#	***
SMI	-	-	-	-2.245 ± 1.314	-1.423 ± 1.506	0.195	-	-	-	2.07 ± 0.427	2.290 ± 0.197	0.137	**< 0.0001** ^	0.604	0.205	***
Trabecular Number (1/mm)	-	-	-	7.543 ± 0.549	7.659 ± 1.018	0.759	-	-	-	4.887 ± 0.378	5.058 ± 0.249	0.224	**< 0.0001** ^	**< 0.0001** ^	0.695	***
Trabecular Thickness (mm)	-	-	-	0.141 ± 0.015	0.145 ± 0.169	0.63	-	-	-	0.052 ± 0.008	0.047 ± 0.004	0.125	**< 0.0001** ^	**< 0.0001** ^	0.916	***
Trabecular Spacing (mm)	-	-	-	0.126 ± 0.019	0.132 ± 0.028	0.548	-	-	-	0.199 ± 0.018	0.192 ± 0.012	0.288	**< 0.0001** ^	**< 0.0001** ^	0.747	***
Bone mineral density (BMD)	986.38 ± 49.15	949.08 ± 56.66	0.125	684.52 ± 58.2	657.47 ± 54.0	0.268	455.21 ± 20.05	439.92 ± 20.91	0.095#	152.89 ± 42.46	139.26 ± 16.34	0.332	**< 0.0001** ^	**< 0.0001** ^	**0.031**	***
Total mineral density (TMD) (mg HA/cm^3)	1215.41 ± 30.73	1219.44 ± 20.06	0.712	1068.88 ± 18.6	1075.64 ± 12.7	0.311	1184.00 ± 20.07	1180.13 ± 8.18	0.565+	835.45 ± 32.00	815.75 ± 27.47	0.137	**< 0.0001** ^	**< 0.001**^	0.29	***

(a) GLM model for main factor effects and overall differences between site and treatment; Interaction term was not significant and is not shown. Subsequent t-test for site specific treatment effects. Significance presented as marginal #(p < 0.1), or significant *(p<0.01), **(p<0.001), ***(p<0.0001), +(uneaqual variance), ^(failed sphericity)

3.8 References

1. Granke M, Does MD, Nyman JS. The Role of Water Compartments in the Material Properties of Cortical Bone. Calcif Tissue Int. 2015 Sep 1;97(3):292–307.

2. Daley E, Streeten EA, Sorkin JD, Kuznetsova N, Shapses SA, Carleton SM, Shuldiner AR, Marini JC, Phillips CL, Goldstein SA, Leikin S, McBride DJ. Variable bone fragility associated with an Amish COL1A2 variant and a knock-in mouse model. Journal of Bone and Mineral Research. 2010;25(2):247–61.

3. Marin C, Papantonakis G, Sels K, van Lenthe GH, Falgayrac G, Vangoitsenhoven R, Van der Schueren B, Penel G, Luyten F, Vandamme K, Kerckhofs G. Unraveling the compromised biomechanical performance of type 2 diabetes- and Roux-en-Y gastric bypass bone by linking mechanical-structural and physico-chemical properties. Scientific Reports. Nature Publishing Group; 2018 Apr 12;8(1):5881.

4. Inzana JA, Maher JR, Takahata M, Schwarz EM, Berger AJ, Awad HA. Bone fragility beyond strength and mineral density: Raman spectroscopy predicts femoral fracture toughness in a murine model of rheumatoid arthritis. Journal of Biomechanics. 2013 Feb 22;46(4):723–30.

5. Zofkova I, Davis M, Blahos J. Trace Elements Have Beneficial, as Well as Detrimental Effects on Bone Homeostasis. Physiol Res. 2017 Jun 30;391–402.

6. Lee C, Lee J-H, Han S-S, Kim YH, Choi Y-J, Jeon KJ, Jung HI. Site-specific and time-course changes of postmenopausal osteoporosis in rat mandible: comparative study with femur. Scientific Reports. Nature Publishing Group; 2019 Oct 2;9(1):14155.

7. Chung U, Kawaguchi H, Takato T, Nakamura K. Distinct osteogenic mechanisms of bones of distinct origins. Journal of Orthopaedic Science. 2004 Jul 1;9(4):410–4.

8. Huja SS, Fernandez SA, Hill KJ, Li Y. Remodeling dynamics in the alveolar process in skeletally mature dogs. The Anatomical Record Part A: Discoveries in Molecular, Cellular, and Evolutionary Biology. 2006;288A(12):1243–9.

9. Tsouknidas A, Jimenez-Rojo L, Karatsis E, Michailidis N, Mitsiadis TA. A Bio-Realistic Finite Element Model to Evaluate the Effect of Masticatory Loadings on Mouse Mandible-Related Tissues. Front. Physiol. Frontiers in Physiology. 2017 May 9; 8(273):1-8.

10. Edwards WB, Schnitzer TJ, Troy KL. Bone mineral and stiffness loss at the distal femur and proximal tibia in acute spinal cord injury. Osteoporos Int. 2014 Mar 1;25(3):1005–15.

11. Matsuura T, Tokutomi K, Sasaki M, Katafuchi M, Mizumachi E, Sato H. Distinct Characteristics of Mandibular Bone Collagen Relative to Long Bone Collagen:

Relevance to Clinical Dentistry. BioMed Research International. 2014 April 10, Article ID 769414.

12. Sasaki M, Matsuura T, Katafuchi M, Tokutomi K, Sato H. Higher Contents of Mineral and Collagen but Lower of Hydroxylysine of Collagen in Mandibular Bone Compared with Those of Humeral and Femoral Bones in Human. Journal of Hard Tissue Biology. 2010;19(3):175–80.

13. Smith-Mungo LI, Kagan HM. Lysyl oxidase: Properties, regulation and multiple functions in biology. Matrix Biology. 1998 Feb 1;16(7):387–98.

14. Trackman PC. Enzymatic and non-enzymatic functions of the lysyl oxidase family in bone. Matrix Biology. 2016 May 1;52–54:7–18.

15. Thomas CJ, Cleland TP, Sroga GE, Vashishth D. Accumulation of carboxymethyl-lysine (CML) in human cortical bone. Bone. 2018 May 1;110:128–33.

16. Arakawa S, Suzuki R, Kurosaka D, Ikeda R, Hayashi H, Kayama T, Ohno R, Nagai R, Marumo K, Saito M. Mass spectrometric quantitation of AGEs and enzymatic crosslinks in human cancellous bone. Scientific Reports. Nature Publishing Group; 2020 Nov 2;10(1):18774.

17. Hanson DA, Eyre DR. Molecular Site Specificity of Pyridinoline and Pyrrole Cross-links in Type I Collagen of Human Bone*. Journal of Biological Chemistry. 1996 Oct 25;271(43):26508–16.

18. Knott L, Bailey AJ. Collagen cross-links in mineralizing tissues: A review of their chemistry, function, and clinical relevance. Bone. 1998 Mar 1;22(3):181–7.

19. van den Bos T, Speijer D, Bank RA, Brömme D, Everts V. Differences in matrix composition between calvaria and long bone in mice suggest differences in biomechanical properties and resorption: Special emphasis on collagen. Bone. 2008 Sep 1;43(3):459–68.

20. McNerny EMB, Gardinier JD, Kohn DH. Exercise increases pyridinoline cross-linking and counters the mechanical effects of concurrent lathyrogenic treatment. Bone. 2015 Dec 1;81:327–37.

21. Hammond MA, Wallace JM. Exercise prevents β-aminopropionitrile-induced morphological changes to type I collagen in murine bone. Bonekey Rep. 2015 Mar 11;4. 1-5.

22. McNerny EM, Gong B, Morris MD, Kohn DH. Bone Fracture Toughness and Strength Correlate With Collagen Cross-Link Maturity in a Dose-Controlled Lathyrism Mouse Model. Journal of Bone and Mineral Research. 2015;30(3):455–64.

23. Naffa R, Holmes G, Ahn M, Harding D, Norris G. Liquid chromatography-electrospray ionization mass spectrometry for the simultaneous quantitation of collagen and elastin crosslinks. Journal of Chromatography A. 2016 Dec 23;1478:60–7.

24. Gaar J, Naffa R, Brimble M. Enzymatic and non-enzymatic crosslinks found in collagen and elastin and their chemical synthesis. Org. Chem. Front. 2020;7(18):2789–814.

25. Bolger MW, Romanowicz GE, Bigelow EMR, Ward FS, Ciarelli A, Jepsen KJ, Kohn DH. External bone size identifies different strength-decline trajectories for the male human femora. Journal of Structural Biology. 2020 Dec 1;212(3):107650.

26. Sinder BP, Zweifler L, Koh AJ, Michalski MN, Hofbauer LC, Aguirre JI, Roca H, McCauley LK. Bone Mass Is Compromised by the Chemotherapeutic Trabectedin in Association With Effects on Osteoblasts and Macrophage Efferocytosis. Journal of Bone and Mineral Research. 2017;32(10):2116–27.

27. Mandair GS, Oest ME, Mann KA, Morris MD, Damron TA, Kohn DH. Radiation-induced changes to bone composition extend beyond periosteal bone. Bone Reports. 2020 Jun 1;12:100262.

28. Gardinier JD, Al-Omaishi S, Morris MD, Kohn DH. PTH signaling mediates perilacunar remodeling during exercise. Matrix Biology. 2016 May 1;52–54:162–75.

29. Oliver WC, Pharr GM. An improved technique for determining hardness and elastic modulus using load and displacement sensing indentation experiments. Journal of Materials Research. Cambridge University Press; 1992 Jun;7(6):1564–83.

30. Burke MV, Atkins A, Akens M, Willett TL, Whyne CM. Osteolytic and mixed cancer metastasis modulates collagen and mineral parameters within rat vertebral bone matrix. Journal of Orthopaedic Research. 2016;34(12):2126–36.

31. Gistelinck C, Weis M, Rai J, Schwarze U, Niyazov D, Song KM, Byers PH, Eyre DR. Abnormal Bone Collagen Cross-Linking in Osteogenesis Imperfecta/Bruck Syndrome Caused by Compound Heterozygous PLOD2 Mutations. JBMR Plus. 2021;5(3):e10454.

32. Zhang H, Zhang Y, Terajima M, Romanowicz G, Liu Y, Omi M, Bigelow E, Joiner DM, Waldorff EI, Zhu P, Raghavan M, Lynch M, Kamiya N, Zhang R, Jepsen KJ, Goldstein S, Morris MD, Yamauchi M, Kohn DH, Mishina Y. Loss of BMP signaling mediated by BMPR1A in osteoblasts leads to differential bone phenotypes in mice depending on anatomical location of the bones. Bone. 2020 Aug;137:115402.

33. Zhang Y, McNerny EG, Terajima M, Raghavan M, Romanowicz G, Zhang Z, Zhang H, Kamiya N, Tantillo M, Zhu P, Scott GJ, Ray MK, Lynch M, Ma PX, Morris MD, Yamauchi M, Kohn DH, Mishina Y. Loss of BMP signaling through BMPR1A in osteoblasts leads to greater collagen cross-link maturation and material-level mechanical properties in mouse femoral trabecular compartments. Bone. 2016 Jul;88:74–84.

34. Unal M. Raman spectroscopic determination of bone matrix quantity and quality augments prediction of human cortical bone mechanical properties. Journal of Biomechanics. 2021 Apr 15;119:110342.

35. McCreadie BR, Morris MD, Chen T, Sudhaker Rao D, Finney WF, Widjaja E, Goldstein SA. Bone tissue compositional differences in women with and without osteoporotic fracture. Bone. 2006 Dec 1;39(6):1190–5.

36. Huja SS, Beck FM. Bone Remodeling in Maxilla, Mandible, and Femur of Young Dogs. The Anatomical Record. 2008;291(1):1–5.

37. Gardinier JD, Rostami N, Juliano L, Zhang C. Bone adaptation in response to treadmill exercise in young and adult mice. Bone Reports. 2018 Jun 1;8:29–37.

Chapter 4.

Sub-critical Defect Healing is Anatomical Site-Dependent as Well as Cellular and Mechanical Response to Beta-aminopropionitrile

4.1 Introduction

Ensuring proper osseous wound healing in both craniofacial bones and long bones is critical to restoring form and function in defects spanning in size from small (tooth extraction, implant/plate placement, biopsy, etc.) to large (reconstruction, trauma, pathologies, congenital defects, etc.). For both small (sub-critical) and large (critical) size defect healing, it is still unknown why some patients heal better (i.e. more quickly, more robust bone formation measured radiographically via density and volume) while others do not. Numerous diseases and lifestyle elements predispose an individual to have a higher risk of delayed or impaired healing[(1)(2)(3)] as well as risk of anatomically site dependent healing complications such as osteonecrosis of the jaw[(4)]. During healing or site specific pathologies are numerous systemic diseases display perturbation to bone matrix composition including the collagen and mineral components and delayed healing[(5)(6)(7)(8)]. While changes to bone composition exist with impaired healing in both craniofacial and long bones, there are limited studies on the direct effect of altered bone matrix on bone healing[(9)(10)].

Bone matrix composition is different between craniofacial and long bones (Chapter 3). Healing time frame and progenitor cell populations are also different[(11)]. For critical size defects of the femur, healing occurs through endochondral ossification, while intramembranous ossification occurs in subcritical defects and cells regenerating the defect are primarily from the marrow space. On the other hand, the maxilla undergoes intramembranous ossification for both sub- and critical size defects and cells regenerating the defect are primarily from the periosteum. Therefore, subcritical defect healing following small fractures, surgical trauma and implant placement may be affected by altered bone matrix composition (via systemic conditions altering

bone composition) in a site dependent manor and may ultimately compromise the quality of the healed bone leading to refracture, implant failure, or site specific conditions such as osteonecrosis.

To determine the effect of altered bone composition (without overt systemic cellular disease) on the quality of the healing bone in both craniofacial and long bones, the model of perturbed collagen cross-linking via beta-aminoproprionitrile (BAPN) was used[12][13](Chapter 3). BAPN irreversibly binds and inhibits the lysyl oxidase (LOX) enzyme in a dose dependent manor. LOX inhibition not only alters the enzymatic collagen cross-link profile[12][13](Chapter 3). LOX also exhibits differential activity between anatomical sites[14]. Therefore, my hypothesis is that *perturbed collagen via BAPN impairs the quality of bone healing dependent on anatomical site due to inherent differences in LOX activity and healing rate.*

4.2 Methods

4.2.1 Animals

All animal procedures were approved by Institutional Animal Care & Use Committee (IACUC) at the University of Michigan. Adult, skeletally mature mice (11-week old, male C57Bl6 (Charles River)) were utilized to minimize growth as a covariate in the analysis of healing. Animals were allowed to acclimate upon arrival for 7 days, then weight matched and assigned to two treatment groups and two end points (7d and 14d post operation). Daily subcutaneous injections of sterile phosphate buffered saline (PBS) or 350 mg/kg BAPN[13] (Beta-aminoproprionitrile fumarate salt, CAS: 2079-89-2, Sigma Aldrich, St. Louis, MO, USA) were administered 7 days prior to surgery and daily until euthanasia (7d or 14d post surgery). 350 mg/kg was chosen to cause a mild perturbation to the cross-links that causes changes to fracture toughness in the long bones of growing mice[13]. To provide sequential fluorochrome labelling for dynamic histomorphometric analysis and to identify newly deposited tissue (cross-link deficient) for nanoindentation, weekly fluorochrome injections were administered – days -7 (alizarin complexone (Alizarin-3-methyl-iminodiacetic acid), 25 mg/kg, Sigma A3882), day 0 (day of surgery) (calcein, 15 mg/kg, Sigma C-0875) and again day 5 (post-surgery), followed by day 12 (post-surgery) for the 14d group (Figure 4.1A). For surgical creation of a subcritical osseous defect (Figure 4.1B), mice were anesthetized with isoflurane (5% induction, 2%

maintenance) and adequate anesthesia was verified with toe pinch. Mice were given pre- and post-op analgesics of carprofen 4.5 mg/kg as directed by IACUC. The maxillary defects were created by retracting the mandible and each cheek to allow visualization and creation of a 0.412 mm transmucosal defect in the maxilla using a mini-kin drill with a slow speed (1500 rpm) drill, 1 mm anterior to the first molar along the maxillary ridge. The femoral defects were created by first shaving off the hair on the distal femur, creating a sterile field, then an incision on the antero-lateral border of the distal femur with blunt dissection to visualize the anterior-distal femur. The same drill and speed were used to create a similar sized defect to the maxilla. Mice were monitored for the duration of the experiment for any adverse reactions to surgery or BAPN. Mice were euthanized at 7d or 14d post surgery by CO_2 inhalation. Femora and maxillae were harvested, cleaned of soft tissue, and stored frozen in gauze soaked in calcium buffered PBS as reported[12][13] for histomorphometric identification of new bone and nanoindentation analysis. A subset of maxillae and femora were harvested and immediately processed for microCT and histology.

4.2.2 MicroCT

Femora (n = 6-7/group) and maxillae (n = 5-6/group) were harvested at sacrifice (7d or 14d) and fixed in 10% formaldehyde for 24 hrs at 4 C, washed and stored in 70% ethanol. Bones were then scanned via microCT. Specimens were placed in a 19 mm diameter specimen holder and scanned using a μCT100 system (Scanco Medical, Bassersdorf, Switzerland). Scan settings were: voxel size 12 μm, 70 kVp, 114 μA, 0.5 mm AL filter, and integration time 500 ms. Analysis was performed using the manufacturer's evaluation software, reoriented using Scanco IPL to obtain a standard region of interest (ROI) and a fixed global threshold of 20% (200 on a grayscale of 0–1000) was used to segment bone from non-bone. A 37 pixel (444 um) diameter circle was centered in the defect and analysis was performed over 30 slices (360 um).

4.2.3 Histomorphometry and Immunohistochemistry

Following microCT, femora (n = 4-5/group) and maxillae (n = 3-6/group) were decalcified with 0.5 M EDTA at 4 C for 14d, embedded in paraffin and sectioned (5 μm) to reveal the osseous defects in cross section. Slides were stained with hematoxylin and eosin

(H&E), Masson's trichrome, Picrosirius Red, tartrate-resistant acid phosphatase (TRAP; 387A, Sigma, following manufacturer's protocol), or LOX (Abcam; ab174316, 1:500 dilution for immunohistochemistry following manufacturer's IHC protocol). All images were analyzed with Fiji[15]. Bone surface was calculated from the Masson's trichrome slides by thresholding and creating a mask from the bone surface in a standardized region of interest (ROI), then using the mask to normalize the osteoblast number (counted as cuboidal, single-nucleated cells on the bone surface in the defect or flat, single-nucleated cells in non-defect sites). Osteoclasts were similarly normalized to bone surface from the Masson's trichrome serial section and counted as TRAP+ multinucleated cells on the bone surface using Fiji software and in accordance with American Society for Bone and Mineral Research standards[16]. LOX-stained sections were quantified for positively stained bone area using Fiji. Bone area masks were created and applied to the defect area. The entire defect was analyzed at a standardized threshold for either the femur (85) or maxilla (60). Positive pixels/total defect pixels were used to represent positively stained bone area.

Birefringent images were acquired from Picrosirius stained sections using a Nikon Eclipse C*i* microscope with bright field and polarized filters with standardized alignment and image settings. Birefringence of Picrosirius stained sections was used to measure morphometric changes to collagen in response to BAPN treatment. Red and green channels represent mature and immature collagen, respectively, as measured via birefringence[17]. To quantify additional collagen parameters (length, width, angle distribution, straightness, and number), the CT-FIRE program[18] was utilized with the red and green channel birefringent images analyzed separately. Settings were changed from default for minimum fiber length: 0, image resolution: 300, fiber line width: 0.5, max fiber width: 15.

Bones from mice treated with PBS or BAPN (C57Bl/6, n=5-7) were prepared for imaging of sequential fluorescent bone labels (alizarin red and calcein) to identify regions of new, cross-link deficient bone. In brief, bones were fresh embedded in poly-methyl-methacrylate (PMMA) (Koldmount, SPI Supplies), sectioned and polishing with a series of fine-grit sandpaper as described[19] and detailed in Section 4.2.4. The fluorescent labels were visualized using a confocal microscope (Nikon Eclipse T*i* confocal microscope). Images were used to locate areas of new tissue for subsequent nanoindentation.

4.2.4 Nanoindentation

Tissue level mechanical properties were measured from the 14 day end-point hemi-maxillae (n=5/group) and femora (n=5/group) at locations that corresponded to the fluorescent labels at day 7 bone (ie. 1 week old bone formed in the defect) and compared to the intracortical bone of the same sample (old bone, formed prior to experiment). Comparisons were made between the new (defect bone) and old (intracortical bone) in each bone (with 5-6 independent indents averaged per site). Samples were sectioned to reveal the defects in cross-section, ground with a series of sandpapers, polished and finished with 0.25 μm diamond suspension (Electron Microscopy Sciences, #50372-21) [19][20](Chapter 3). A Berkovich tip was then loaded at each site at 2000 μNs^{-1}, to 10 mN, then unloaded at 2000 μNs^{-1} with a 60 s hold time using a 950 TI TriboIndenter (Hysitron, Minneapolis, MN, USA). This step load was adapted from Wu, et al.[21] to measure both viscoelastic behavior (creep), elastic measurements (Young's modulus) and plastic measurements (stiffness and hardness). All measures were done in a humid state (surface hydration with calcium buffered PBS). Young's modulus and hardness were extracted from the load-displacement curve generated using the Oliver-Pharr method[22]. Creep behavior was extracted using a custom MATLAB code to fit the displacement-time curve to a Burgers model[21] (Figure 4.2). This model utilized the instantaneous modulus (E_1) and instantaneous viscosity (η_1) as well as the long term modulus (E_2) and parallel viscosity (η_2) to yield the viscoelastic time constant (τ).

4.2.5 Statistics

The study was designed with a power calculation (for analysis via 2-way ANOVA) based on the desired primary outcome of bone healing (BV/TV) evaluated via microCT. Mean and variance for this calculation were found in similar work studying sub-critical defects in femoral bone. This calculation yielded a minimum of n=2. However, n=12/group was chosen due to lack of similar data to predict healing differences in the maxilla, which heals at a slower rate[23]. Prism 8 was used for statistical analysis. A two-way ANOVA was used to determine effects of BAPN and time (days of healing) for each bone. For the nanoindentation data, a 3-way ANOVA was used to analyze effects of bone, site and treatment and a mixed effects model (M-E model) for repeated measures analysis of healing (defect) bone to adjacent, non-defect bone (intracortical).

Data is presented as the mean +/- SD or as percent change in new, healing bone compared to existing bone. Factor effects and direct comparisons of time and treatment are shown, the interaction of time and treatment was not significant and is not shown. Significance was considered if $p < 0.05$, values of $p < 0.1$ are noted as trends.

4.3 Results

4.3.1 BAPN Alters LOX Expression and Collagen Fibers Differently in Femoral and Maxillary Osseous Wound Sites

To study the effect of perturbed collagen on intramembranous subcritical osseous wound healing, small (0.45 mm dia.) cortical defects were created in the maxilla and femur, bilaterally. All animals healed without infection and the maxillary defect healed without any need for closure material (continuous epithelium present at 7d and 14d). Daily subcutaneous delivery of 350 mg/kg BAPN or PBS were administered, resulting in 7 days of pre-treatment and 7 or 14 days of treatment following osseous surgery. There was a significant decrease in anti-LOX+ stained bone in the maxillary defect with an overall treatment effect ($p = 0.0198$, 2-way ANOVA), yet post-hoc tests did not reveal individual differences (Figure 4.3A). A trend of reduced anti-LOX+ stained bone area was noted for an overall treatment effect in the femur defect ($p=0.0635$, 2-way ANOVA) (Figure 4.3B). Defect sites showed an increase in anti-LOX+ bone area compared to the surrounding bone (data not shown).

Birefringent analysis (workflow depicted in Figure 4.4) revealed changes in the red and green channel analysis for the femur and maxilla over time (Table 4.1). The red channel (representing mature collagen) fiber length for the maxilla increased over time, as did the green channel (representing immature collagen) fiber number and length ($p < 0.05$, two-way ANOVA). The red and green channel fiber width increased over time for the femur ($p < 0.05$, two-way ANOVA, Table 4.1). No significant effect of treatment was seen.

4.3.2 Viscoelastic Properties are Altered in Defect Sites Compared to Existing Bone with BAPN Treatment

Nanoindentation was used to determine the Young's modulus, stiffness, hardness, and viscoelastic creep properties of new, healing bone (defect), as compared to the adjacent, non-defect bone (intracortical) that was unaffected by surgery or by BAPN (or control PBS) treatment. Percent change from defect to intracortical bone is presented. The maxilla and femur showed different responses to BAPN treatment, as exhibited by differences in mechanical properties. The stiffness of the maxillae treated with BAPN decreased (15%, $p < 0.05$) but maxillae treated with PBS had a non-significant decrease of only % (Figure 4.5A, M-E model). The femora showed no change in stiffness (12-14% decrease in new bone for both groups, Figure 4.5A). Hardness (Figure 4.5B, M-E model) was decreased in the BAPN treated femora (26%, $p < 0.05$) but not in the PBS treated femora (21%). The maxilla showed no significant differences in hardness with BAPN treatment (19-20%) (Figure 4.5B). Young's modulus was decreased at all sites (Femur PBS, 23%, Femur BAPN, 25%, Maxilla PBS, 17%, Maxilla Defect, 23%) (Figure 4.5C, $p < 0.05$, M-E model). For overall bone effects, the hardness was significantly higher in the maxilla compared to the femur ($p < 0.05$, 3-way ANOVA, Figure 4.5B).

Viscoelastic measures were extracted from the Burger's model (Figure 4.2) to estimate creep behavior. The primary comparison being made was healing bone (defect) vs. adjacent, non-defect bone (intracortical) with/without BAPN treatment. Creep distance (A, M-E model) was increased significantly in the BAPN treated femur (-30%, $p < 0.05$) and had trends of an increase in creep distance in all other sites and with BAPN treatment (PBS femur (-25%), BAPN maxilla (-30%), and PBS maxilla (-29%). The creep retardation time (τ) was not changed with treatment (B). Plastic work showed an increasing trend in healing bone compared to existing bone (C, M-E model) (femur PBS, -19%, maxilla PBS, -24%, maxilla PBS, -22%), reaching significance in the femora treated with BAPN (-23%) ($p < 0.05$). Elastic work showed an increasing trend in the BAPN treated maxillae (-35%) (D, $p = 0.085$, M-E model). Plastic index (ratio of plastic work to elastic work) remained unchanged (-3-1%) for each group (E). Instantaneous creep constants (E_1 and η_1, Figure 6 F&G) showed no change with treatment except for E_1 in the BAPN treated maxilla group (19%) (Figure 6G, $p < 0.05$, M-E model). The

long-term modulus, E_2 (H) was decreased in the BAPN treated femora (28%, $p = 0.05$) and the PBS treated maxillae (22%, $p < 0.05$, M-E model), with a trend in the BAPN treated maxillae (22%, $p = 0.07$, M-E model). η_2 showed a significant decrease in the PBS treated maxillae (25%, $p < 0.05$, M-E model) and a trend in the BAPN treated maxillae (26%, $p = 0.07$, M-E model) (Figure 4.6I), but there was no difference in the PBS or BAPN treated femora. For overall bone effects, E_1, E_2 and η_2 were all significantly higher in the maxilla compared to the femur ($p< 0.05$, 3-way ANOVA)(Figure 4.5A and F,H,I).

4.3.3 Delayed Healing Rate in Maxilla Compared to Femur, Yet Healing Rate is Not Changed with BAPN Treatment

Mineral density and percent bone-fill were assessed via micro-CT at 7d or 14d following creation of osseous defects to determine the bone-fill healing rate (or increase in bone volume from 7 to 14 days). Bone volume fraction (BV/TV) and TMD were unchanged with BAPN treatment, but there were significant differences in healing rates between bones. Femoral bone-fill increased by 60% from 7d to 14d (A)($p < 0.001$, 2-way ANOVA), whereas the maxilla had no significant change over this time frame (C). The femora showed a decrease in TMD from 7d to 14d (B)($p < 0.01$, 2-way ANOVA) and no change was detected in the maxillae (D). The maxillae had more ectopic bone formation as compared to the femora (Figure 4.7).

4.3.4 Femur Osteoclast Numbers Initially Reduced with BAPN, then Increased at Day 14

Defect sites in the femur and maxilla were histologically assessed for osteoclasts (TRAP+, multinucleated cells), osteoblasts (pink cuboidal cells via Masson's trichrome), and osteocytes (occupied and empty lacunae via Masson's trichrome). BAPN was not expected to alter the number of osteoclasts, osteoblasts, or osteocytes. However, the number of TRAP+ osteoclasts per bone surface decreased at 7 days in femoral defects in BAPN treated mice compared to PBS controls (A)($p < 0.05$, 2-way ANOVA). A similar trend was seen in the maxilla though not significant. There was a subsequent increase in osteoclasts/B.Pm. with BAPN treatment in the femora at day 14 (B)($p < 0.05$, 2-way ANOVA), but no change in the maxillae. No change in osteoblasts or osteocytes was seen in either bone defect (S1). Because of the difference in osteoclasts/B.Pm. with BAPN treatment in the defect, the osteoclasts, osteoblasts

and osteocytes were also quantified in non-defect sites of the femur (distal trabeculae) and maxilla (pre-maxillary suture). No difference was seen in osteoclasts or osteoblasts in either bone or over time (S2). The only change in osteocytes detected was the % empty lacunae, with an increase with BAPN at day 7 but no change at 14d as compared to PBS.

4.4 Discussion

Collagen cross-linking influences bulk mechanical properties of bone[13][12], yet less is known about differential effects of cross-link changes between long bones and craniofacial bones, especially during osseous wound healing. Since numerous systemic conditions can negatively affect both collagen cross-linking and healing, this study sought to perturb collagen cross-links without a systemic co-morbid disease state to determine the effect of perturbed collagen cross-linking on bone healing. This animal model of systemic inhibition of LOX via BAPN allows for comparisons between different bones undergoing a consistent mode of healing - intramembranous ossification. This study showed that the femur has an accelerated healing phase compared to the maxilla (Figure 4.7), with increased LOX+ bone (Figure 4.3). There was also decreased hardness and Young's modulus in BAPN affected healing bone (Figure 4.5). The maxilla had lower LOX+ staining and healed minimally in the 14 day time period (Figure 4.3) with reduced Young's modulus and stiffness in BAPN affected healing tissue (Figure 4.5). Reduced modulus and stiffness is suggestive of mineral changes (though not measured here), which may be bone dependent rather than healing rate dependent since newly formed bone in both the maxilla (slow healing) and femur (fast healing) exhibited reduced Young's modulus with BAPN treatment. Data in Chapter 3 also demonstrated an anatomical site dependent alteration in mineral content with BAPN treatment during normal growth and development. The implication of the findings presented in Chapter 4 is that mechanical properties of healing bone are driven by collagen as well as anatomical location and therefore anatomical site differences should be considered as a component of design criteria for fixed implantable devices as well as for response to pharmacological therapies targeting improvement of bone mechanics.

The viscoelastic properties (Figure 4.7) were extracted from nanoindentation at local sites to discern the matrix mechanical response at areas of new (defect) and existing (intracortical) tissue. The Burger's model was used to estimate the viscoelastic properties of bone by extracting

several spring constants to fit a model of creep behavior to the experimental data. The long-term spring constants (E_1, E_2, η_2) increase in the maxilla compared to the femur. Yet treatment effects only manifested in a decrease in the E_1 metric in the maxillary defect, decrease in the E_2 metric in the femoral defect and a trend toward a decrease in E_2 in the maxillary defect. Defect related decreases were seen in the E_2 maxilla defect value and the η_2 maxilla value. While all groups had increased creep within the defect compared to intracortical bone, the femur BAPN group was the only one to reach significance. The hardness was also significantly higher in the maxilla compared to the femur, which trends with the higher E_2 and η_2. Stiffness and E_1 both changed with BAPN treatment in the maxilla, suggesting a possible relation between these parameters.

The increase in the E_2 and η_2 constants in the maxilla compared to the femur is of interest. The constants could relate to the mineral/collagen interaction in the bone matrix, as has been shown with filler content in thermoset nanocomposites[24]. With increasing filler content (similar for modeling purposes to the mineral component of bone) the E_2 and η_2 values in man-made composites increase. The collagen in craniofacial bones is also more highly cross-linked (Chapter 3) with mature cross-links (like a 3-D conformation of a thermoset polymer) and therefore the bone may be behaving similarly to thermoset nanocomposites.

The viscoelastic constants and mechanical properties are altered with BAPN treatment in an anatomical site dependent fashion, highlighting the need to understand mechanical regulation in a bone specific manor. There are numerous implications for changes in tissue level mechanical properties in healing bone within a defect. These include resistance to mechanical deformation around an implant/osseous screw, healing after microfracture, or removal of tissue due to pathologies. All of these clinical scenarios could be impacted by systemic conditions that affect collagen cross-linking, such as diabetes, smoking, or radiation[5][6][7][8].

Surprisingly, BAPN also altered the osteoclast response in the defect bone, more so in the femur (where LOX+ bone was higher) than the maxilla (Figure 4.3) and not in the non-defect bone. BAPN altered collagen increases osteoclastic activity in vitro[17] and loosely cross-linked ECM promotes osteoclast maturation[25]. Conditions such as osteoporosis and diabetes lead to impaired collagen cross-linking[26][5] and reduced LOX[27][5] as well as concurrent increase in osteoclasts[29][30]. There was no change in osteoclast number with BAPN treatment in the non-defect sites, highlighting that the deceased osteoclast number is likely due to the new (BAPN

affected) tissue being deposited as the non-defect sites are not rapidly forming bone and should be relatively unaffected by BAPN treatment. While the direct mechanism is not shown here, it is important to determine if targeting recovery of LOX in bone disease (e.g. under cross-linked) tissue could reduce the concurrent increase in osteoclasts.

The osteoclast number is higher in the femoral defect than the maxillary defect, which is consistent with other studies comparing long bone and craniofacial bone[31][32]. A potential cause for these site specific differences is the difference in cell source for each bone (neural crest for maxilla vs. mesoderm for femur), and compartment (periosteum for maxilla vs. marrow for femur). The femur was occupied by primarily marrow cells (qualitative from H&E sections), whereas the maxilla had infiltration of sinus tissue and cells appear to be primarily from the periosteum (qualitative from dynamic histomorphometry and H&E). Pharmacological intervention (ie. bisphosphonates) to control osteoclast number and activity is also site specific during healing[31][33]. Further studies on the LOX status with drugs such as bisphosphonates could lead to another possible target for therapeutic intervention to not only improve mechanical function, but also modulate the osteoclast response.

Systemic administration of BAPN reduced the tissue level mechanical properties of newly formed bone in osseous defects in a site-specific manor. The mechanical loading environment, healing rates, LOX expression, and osteoclasts are different between the femur and maxilla and produce an altered response to perturbed collagen. Results from this study highlight the need for consideration of anatomical site dependence of osseous wound healing. This work opens doors to further investigate the potential to modulate LOX expression during healing to improve mechanical properties of newly formed bone in a variety of disease states.

4.5 Acknowledgements

I would like to thank my co-authors: Lizhong Zhang, Morgan Bolger, Michelle Lynch, David H. Kohn. The authors would like to thank Dr. Hsiao Sung for training with the subcritical osseous defect model and Chris Strayhorn and Theresa Cody for histology sectioning and staining. Research reported in this publication was supported by the National Institutes of Health NIDCR T32 DE007057, F30 DE028167. Research reported in this publication was also supported by the National Institutes of Health NIAMS P30 AR069620 (Dr. Ken Kozloff,

Nanoindentation) and R01 AR065424, R01 AR068452. The micro-CT core at the Michigan School of Dentistry is funded in part by NIH/NCRR S10RR026475-01. The content is solely the responsibility of the authors and does not necessarily represent the official views of the National Institute of Health.

4.6 Author Contributions

Study design: GR and DK. Study conduct: GR, MB, and LZ. Data collection: GR and LZ. Data analysis: GR, MB and LZ. Data interpretation: GR and DK. Drafting manuscript: GR. Revising manuscript content: GR and DK. Approving final version of manuscript: GR, MB, LZ, and DK. GR and DK take responsibility for the integrity of the data analysis.

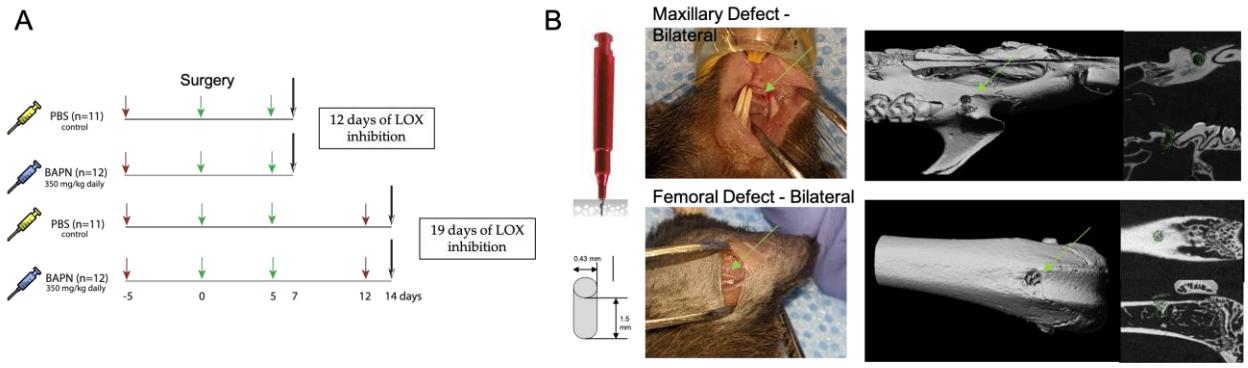

Figure 4.1 Schematic of experimental design (A) 2 treatments (Phosphate buffered saline (PBS) or 350 mg/kg beta-aminoproprionitrile (BAPN)) and two end points (7 day or 14 day post surgery). Daily subcutaneous injections were given of PBS or BAPN and fluorophores (red = alizarin red complexone, green = calcein) were injected at 5 days prior to surgery, day of surgery, 5 days post surgery, and 12 days post surgery. (B) Images of defect location (maxilla or femur) and size (0.43 mm diameter) with corresponding microCT images of the defects.

$$h^2(t) = \frac{\pi}{2} P_0 \cot\cot\alpha\,(1-\nu^2)\left[\frac{1}{E_1} + \frac{1}{E_2}\left(1 - e^{-\frac{t}{\tau}}\right) + \frac{1}{\eta_1(1-\nu^2)}t\right]$$

$$\tau = \frac{E_2}{\eta_1}$$

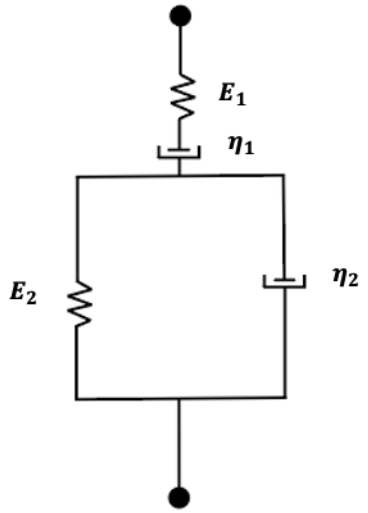

- $h^2(t)$ is the indentation depth [nm] at time(t)
- P_0 is the peak force [mN]
- α is the equivalent cone semi−angle (70.3° for a Berkovich indenter)
- ν is the Poissan's ratio for the material
- E_1 is the instantaneous modulus (Gpa)for the sample
- η_1 is the long−term creep viscosity (Gpa s)
- E_2 is the long − term modulus for the sample
- τ is the creep time constant (s)
- η_2 parallel viscosity (Gpa s)

Figure 4.2 Equation used to calculate a fit of the Burgers model to the experimental data for extraction of viscoelastic properties of the bone at either the defect location or intracortical location. Terms are described in the figure.

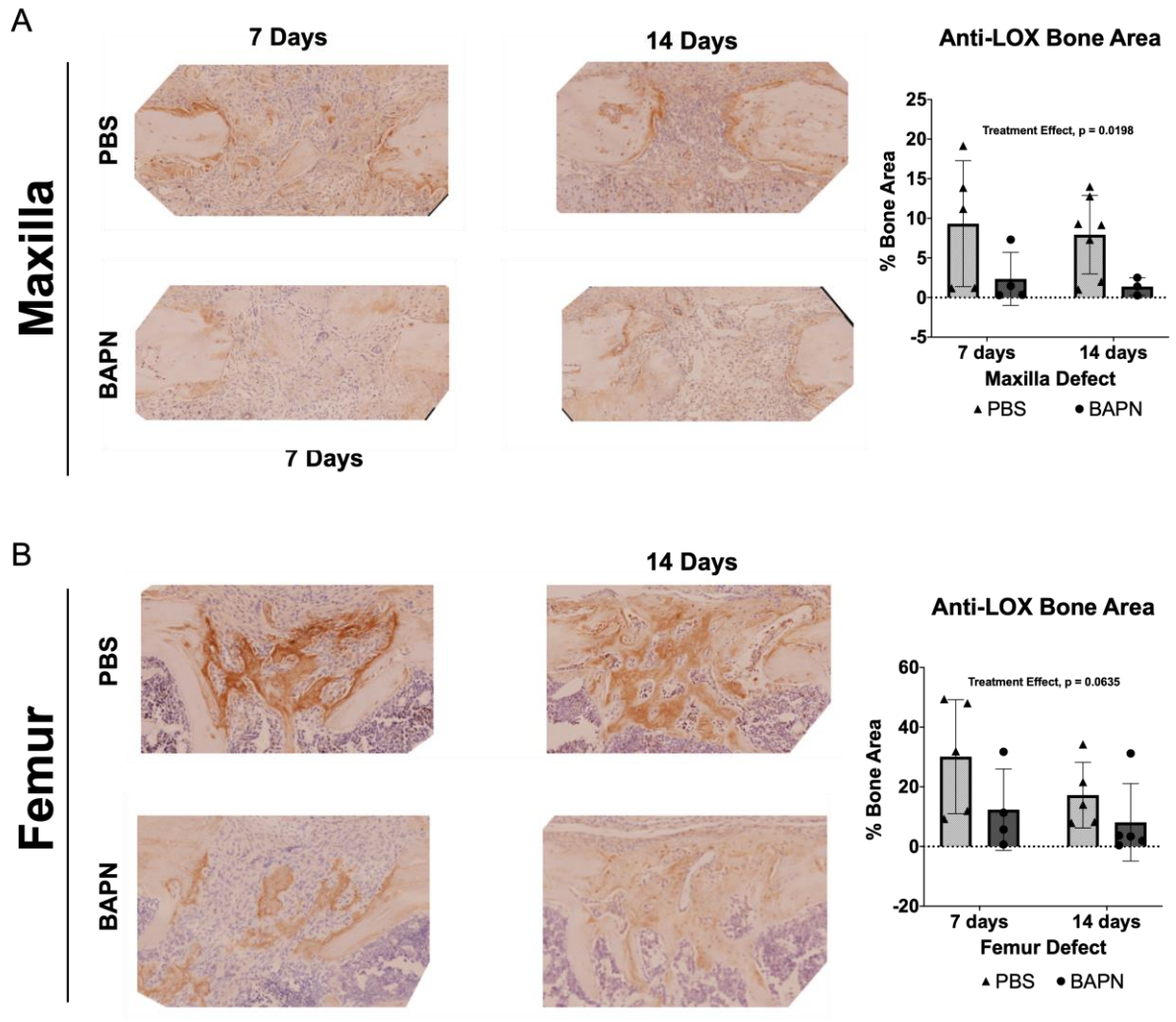

Figure 4.3 Immunohistochemistry depicting lysyl oxidase (LOX) enzyme positive bone areas in the maxillary and femoral defects with phosphate buffered saline (PBS) or beta-aminoproprionitrile (BAPN). (A) Anti-LOX bone area was significantly decreased with BAPN treatment ($p = 0.0198$) compared to PBS in the maxilla. (B) Anti-LOX bone area showed a trend of a decrease with BAPN treatment ($p = 0.0635$, 2-way ANOVA) in the femur compared to PBS in the femur). *$p < 0.05$, **$p < 0.001$, ***$p < 0.0001$, 2-way ANOVA.

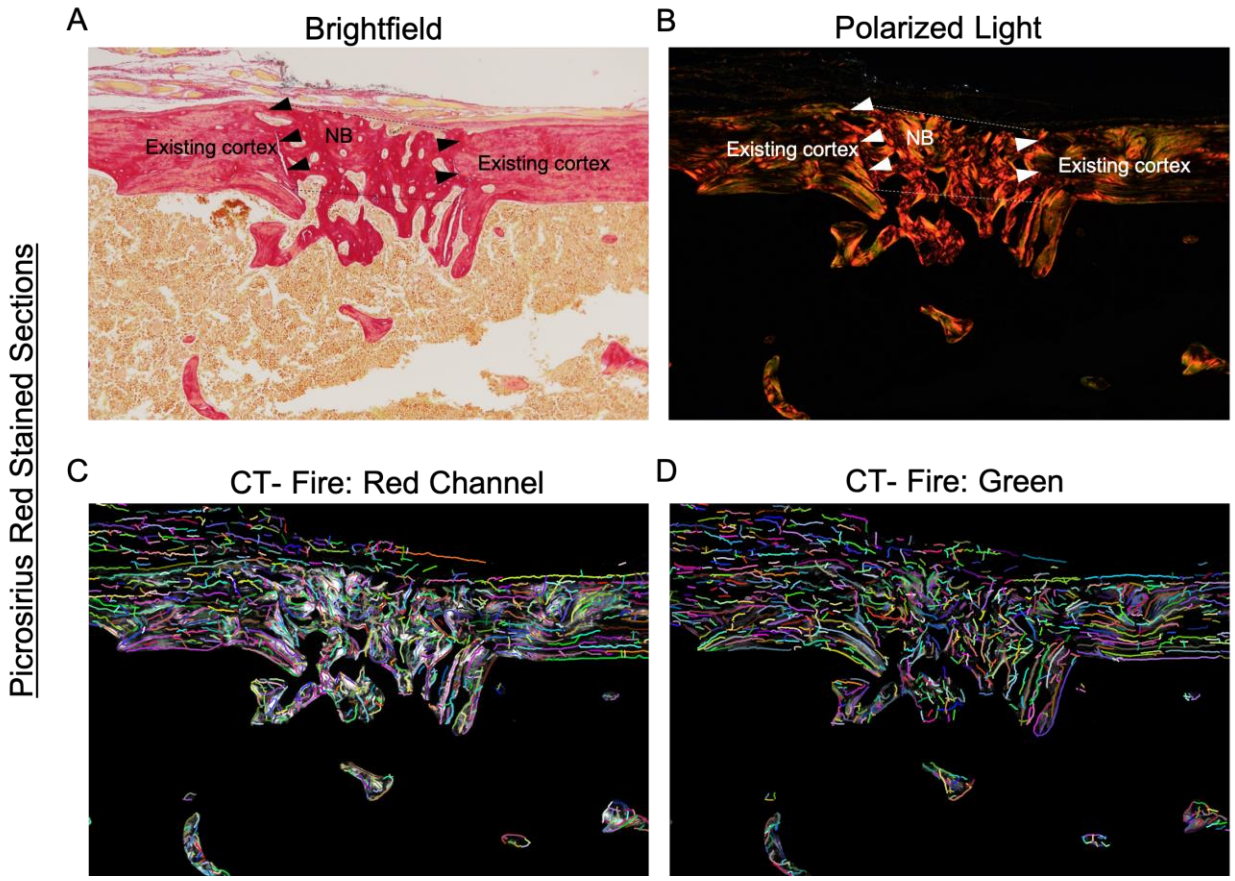

Figure 4.4 Representative images of the workflow for birefringent analysis of the Picrosirius Red histological sections. (A) Brightfield view of a femoral defect, showing areas of new bone (NB) and existing, non-defect cortical bone. (B) Same view of image A under polarized light, using consistent settings and alignment between samples. (C) Output from the CT-Fire program when the image from B is split into Red, Blue, Green channels and the Red channel (representative of mature collagen fibers) is analyzed. The program identifies individual fiber traces and quantifies the number, alignment, length, width, and straightness (See Table 1). (D) CT-Fire output of the Green channel image. (Blue channel was not analyzed – no signal).

Table 4.1 Birefringent analysis of red and green channels using CT-FIRE for the femoral and maxillary defects. Both the femora (fiber width) and maxillae (fiber length, number and straightness) showed changes to mature (Red) fibers and immature (Green) fibers with time. However, there was no effect of BAPN treatment. Abbreviations: PBS, phosphate buffered saline (control group), BAPN, Beta-aminoproprionitrile (test group); Values presented as mean ± s.d. n = 4-5 per group for femur, n = 3-7 per group for maxilla. *p < 0.05, **p < 0.001, ***p < 0.0001, effect of time (change in 7 to 14 days). No significant effect of BAPN, 2-way ANOVA.

Femur

	Day 7 PBS	*Day 7 BAPN*	*Day 14 PBS*	*Day 14 BAPN*
Red Channel				
Fiber number	132.80 ± 44.01	127.50 ± 65.86	158.60 ± 19.32	163.60 ± 35.57
Fiber Length	35.74 ± 1.82	37.90 ± 1.88	39.34 ± 2.05	37.66 ± 2.41
Fiber Width *	5.72 ± 0.65	5.60 ± 0.29	6.30 ± 0.38	6.14 ± 0.30
Fiber Angle	81.56 ± 6.62	76.63 ± 17.80	91.74 ± 15.85	85.90 ± 7.20
Fiber Straightness	0.94 ± 0.01	0.94 ± 0.00	0.93 ± 0.01	0.93 ± 0.01
Green Channel				
Fiber number	124.40 ± 46.05	130.50 ± 62.63	154.60 ± 19.40	156.00 ± 39.61
Fiber Length	34.74 ± 3.14	38.30 ± 2.79	37.18 ± 2.82	36.90 ± 2.77
*Fiber Width***	4.96 ± 0.38	5.05 ± 0.18	5.49 ± 0.32	5.54 ± 0.19
Fiber Angle	84.44 ± 10.72	76.73 ± 17.46	92.26 ± 13.73	85.36 ± 8.23
Fiber Straightness	0.94 ± 0.01	0.94 ± 0.00	0.93 ± 0.01	0.93 ± 0.00

Maxilla

	Day 7 PBS	*Day 7 BAPN*	*Day 14 PBS*	*Day 14 BAPN*
Red Channel				
Fiber number	169.20 ± 58.68	119.75 ± 28.00	162.43 ± 37.72	178.33 ± 62.07
Fiber Length ***	33.94 ± 2.28	31.88 ± 1.76	39.56 ± 3.13	36.97 ± 2.64
Fiber Width	5.49 ± 0.24	5.13 ± 0.15	5.39 ± 0.29	5.49 ± 0.48
Fiber Angle	80.52 ± 7.50	82.48 ± 11.17	82.00 ± 12.46	82.63 ± 8.47
Fiber Straightness	0.93 ± 0.01	0.94 ± 0.01	0.93 ± 0.01	0.93 ± 0.01
Green Channel				
*Fiber number**	139.00 ± 45.54	90.25 ± 33.71	154.29 ± 39.10	181.67 ± 70.55
*Fiber Length***	33.78 ± 2.45	31.25 ± 0.62	37.89 ± 3.67	36.87 ± 3.55
Fiber Width	4.83 ± 0.25	4.51 ± 0.10	4.78 ± 0.20	4.85 ± 0.30
Fiber Angle	83.44 ± 9.39	88.40 ± 10.87	83.77 ± 11.42	82.00 ± 6.07
*Fiber Straightness***	0.94 ± 0.00	0.94 ± 0.01	0.93 ± 0.01	0.93 ± 0.00

Abreviations: PBS, phosphate buffered saline (control group), BAPN, Beta-aminoproprionitrile (test group); Values presented as mean ± s.d. n = 4-5 per group for femur, n = 3-7 per group for maxilla. *p < 0.05, **p < 0.001, ***p < 0.0001, effect of time (change in 7 to 14 days). No significant effect of BAPN, 2-way ANOVA.

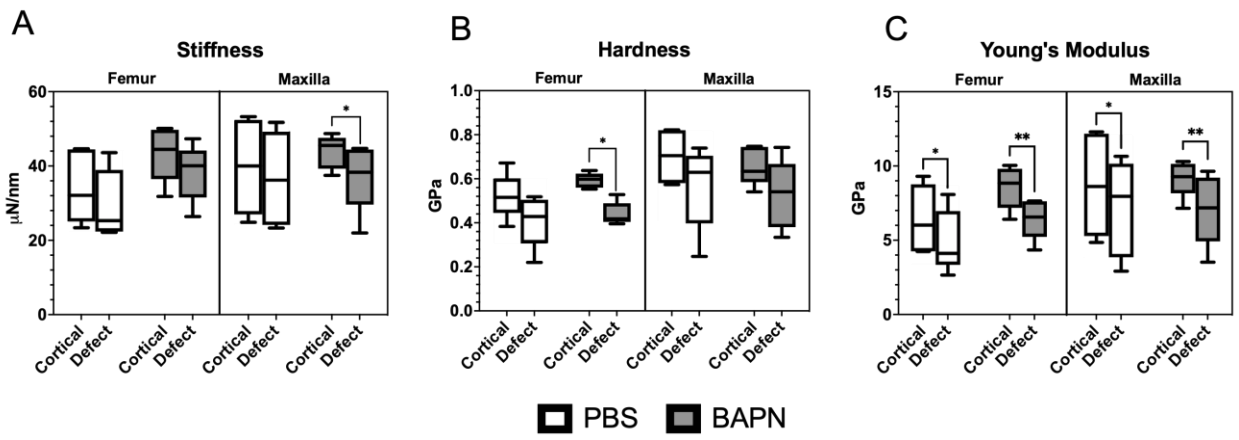

Figure 4.5 Nanoindentation was used to determine the Young's modulus, stiffness, hardness, and viscoelastic creep properties of new, healing bone (defect), compared to the adjacent, non-defect bone (intracortical) that was unaffected by surgery or by beta-aminoproprionitrile (BAPN) treatment. Changes in properties from defect to intracortical regions of bone are presented. (A) Stiffness was only decreased in defect bone of the maxillae treated with BAPN ($p < 0.05$). (B) Hardness was only decreased in the BAPN treated femora ($p < 0.05$). For overall bone effects, the hardness was significantly higher in the maxilla compared to the femur ($p < 0.05$, 3-way ANOVA) (C) Young's modulus was decreased at all sites (Femur PBS, Femur BAPN, Maxilla PBS, Maxilla Defect) ($p < 0.05$ for PBS groups and $p < 0.01$ for BAPN treated groups). ($p < 0.05$). *$p < 0.05$, **$p < 0.001$, ***$p < 0.0001$, Mixed-Effect model unless otherwise noted.

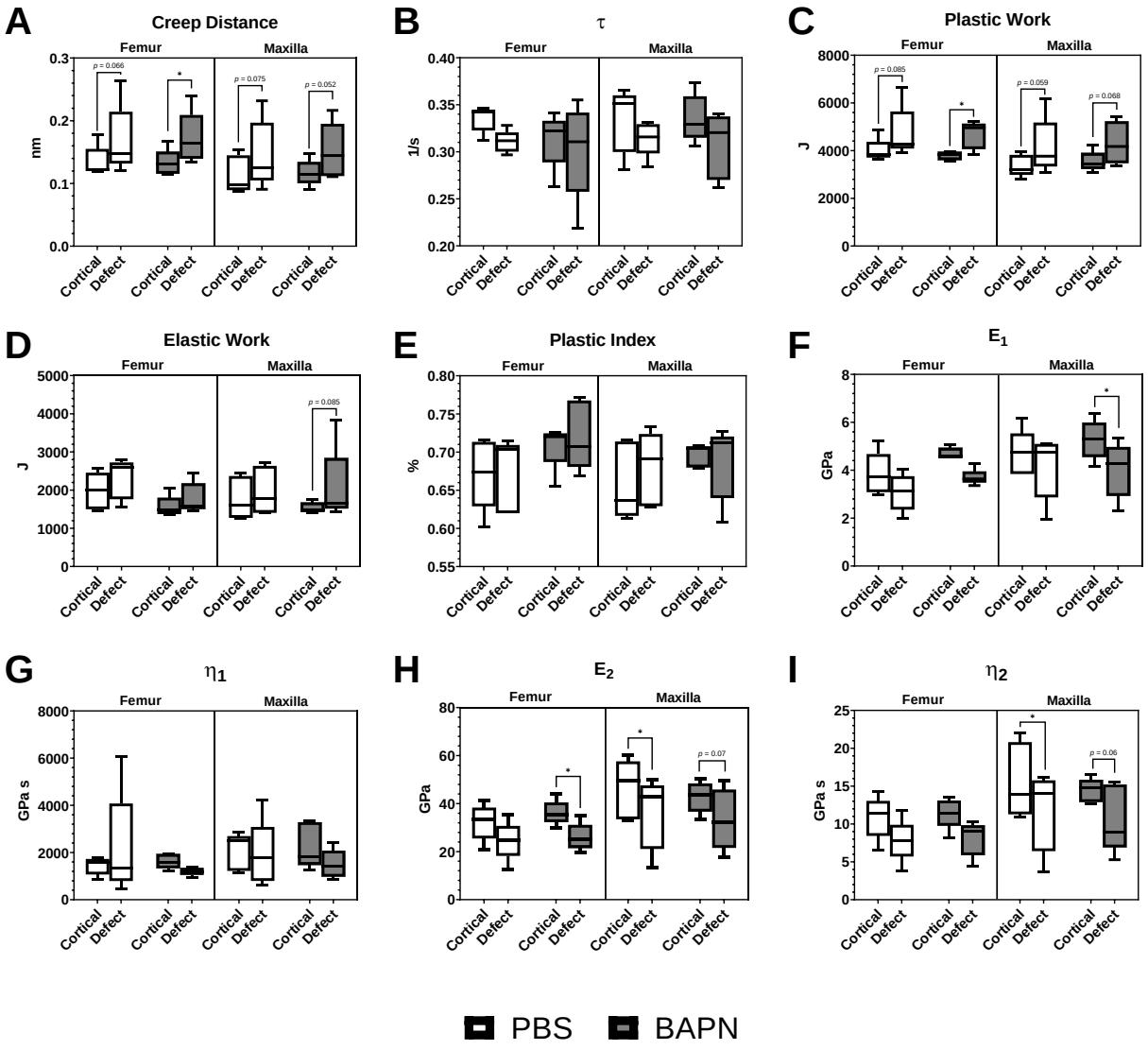

Figure 4.6 Viscoelastic measures were extracted from the Burger's model to estimate creep behavior. The primary comparison made was healing bone (defect) vs. adjacent, non-defect bone (intracortical) with/without beta-aminoproprionitrile (BAPN) treatment. (A) Creep distance was increased in the BAPN treated femora ($p < 0.05$) and there were trends of an increase in creep distance in all other sites and with BAPN treatment ($p < 0.1$). (B) The creep retardation time (τ) did not change with BAPN treatment. (C) Plastic work showed an increasing trend at all sites, reaching significance in the femora treated with BAPN ($p < 0.05$). (D) Elastic work showed an increasing trend in the BAPN treated maxillae ($p = 0.085$). (E) Plastic index (ratio of plastic work to elastic work) remained unchanged for each group. (F) Instantaneous modulus (E_1) showed no change with BAPN treatment except for in the maxillae ($p < 0.05$). E_1 was also increased in the maxilla compared to the femora ($p< 0.05$, 3-way ANOVA). (G) Long term creep viscosity (η_1) showed no change between sites or with BAPN treatment. (H) The long-term modulus (E_2) was decreased in the BAPN treated femora ($p = 0.05$) and the PBS treated maxillae

($p < 0.05$) with a trend in the BAPN treated maxillae ($p = 0.07$). E_1 was also increased in the maxillae compared to the femora ($p< 0.05$, 3-way ANOVA). (I) Parallel creep viscosity (η_2) showed a significant decrease in the PBS treated maxilla ($p < 0.05$) and a trend in the BAPN treated maxilla ($p = 0.07$), but no difference in the PBS or BAPN treated femora. η_2 was significantly higher in the maxilla compared to the femur ($p< 0.05$, 3-way ANOVA). *$p < 0.05$, **$p < 0.001$, ***$p < 0.0001$, Mixed-Effect model unless otherwise noted.

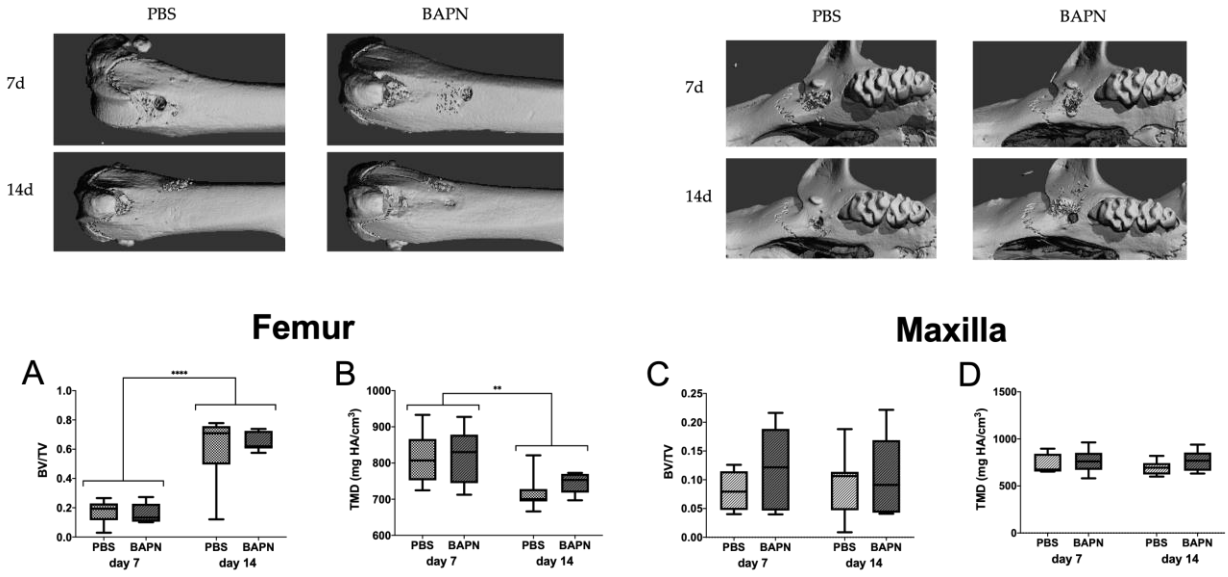

Figure 4.7 Representative images (TOP LEFT - FEMUR, AND RIGHT - MAXILLA) of microCT 3D images of the defects at day 7 and 14 for control (PBS) and beta-aminoproprionitrile (BAPN) groups. (A) Bone volume/total volume (BV/TV) in the femur was increased by about 60% from 7 days post surgery to 14 days post surgery ($p < 0.0001$), but no change occurred with BAPN treatment. (B) Total mineral density (TMD) was decreased from 7 days post surgery to 14 days post surgery ($p < 0.01$), but not by BAPN treatment. (C) BV/TV was unchanged in the maxilla between 7 and 14 days of healing or with BAPN treatment. (D) BV/TV was unchanged in the maxilla between 7 and 14 days of healing or with BAPN treatment. *$p < 0.05$, **$p < 0.001$, ***$p < 0.0001$, 2-way ANOVA.

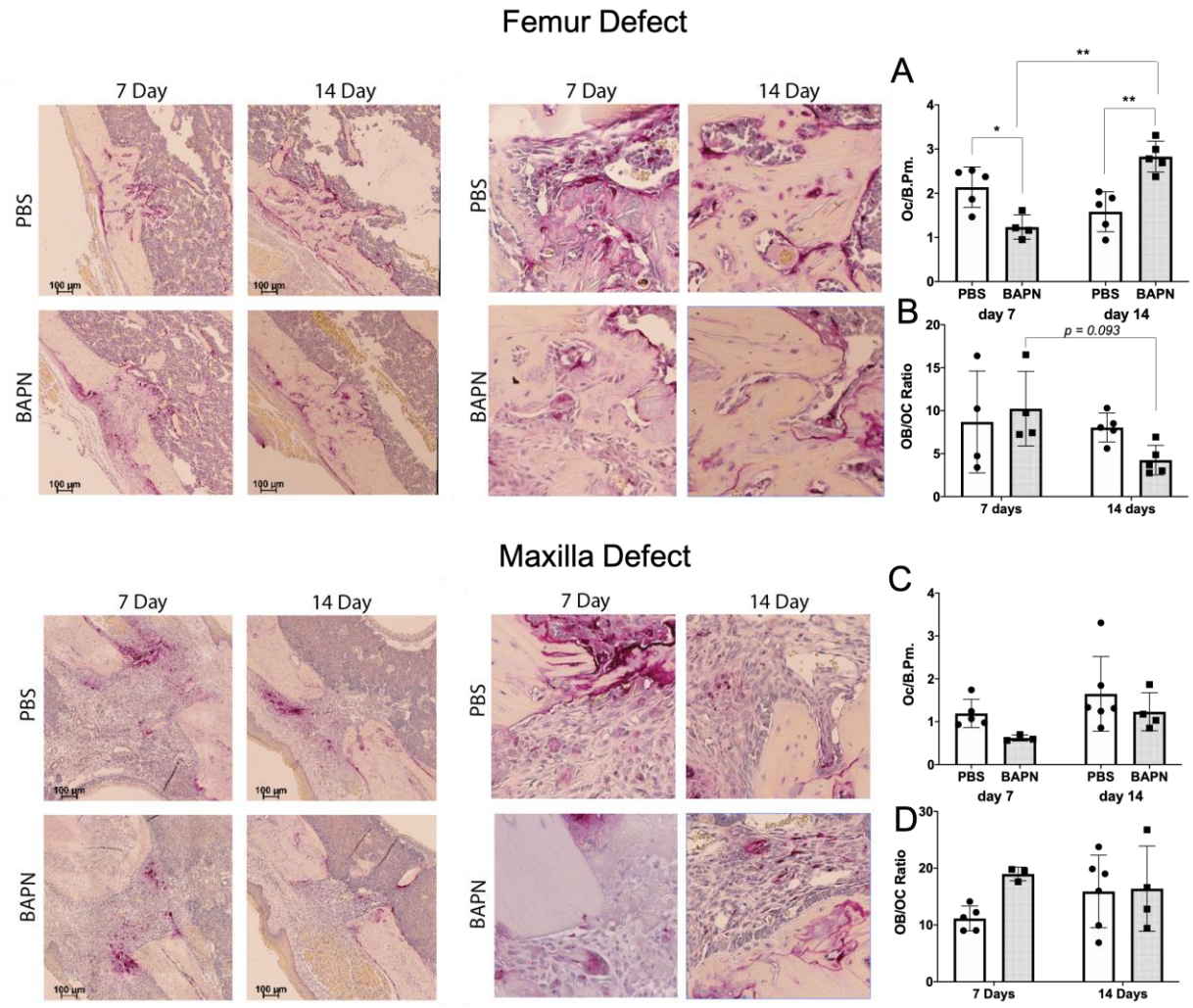

Figure 4.8 Representative images (TOP LEFT - FEMUR, AND BOTTOM LEFT - MAXILLA) of tartrate resistant alkaline phosphatase (TRAP) staining to highlight osteoclasts in the healing defects at day 7 and 14 for the control (PBS) and beta-aminoproprionitrile (BAPN) treatment groups. (A) Femoral defect osteoclasts per bone perimeter (OC/B.Pm.) increased from 7 days to 14 days ($p < 0.01$), decreased with BAPN treatment at day 7 ($p < 0.05$) and increased at day 14 ($p < 0.01$). (B) Femoral defect osteoblast/osteoclast ratio (OB/OC) had a trend of a decrease from 7 days post surgery to 14 days post surgery ($p = 0.093$) in the BAPN treatment group. (C) Maxillary defect Oc/B.Pm. showed no significant change with time of healing or BAPN treatment. (D) Maxillary defect OB/OC ratio showed no significant change with time of healing or BAPN treatment. *$p < 0.05$, **$p < 0.001$, ***$p < 0.0001$, 2-way ANOVA.

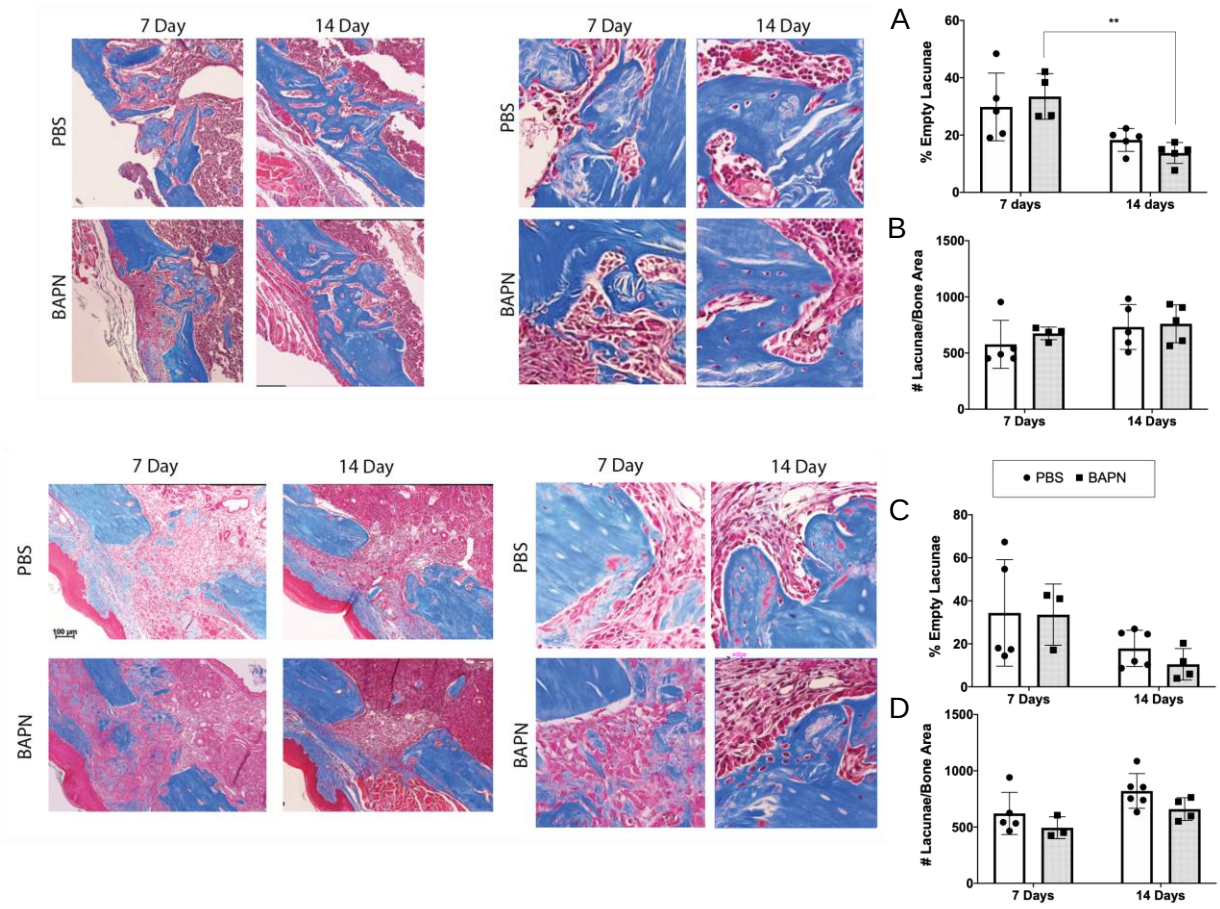

Figure 4.9S1 Representative images (TOP LEFT - FEMUR, AND BOTTOM LEFT - MAXILLA) of Masson's trichrome staining to highlight collagen in the healing defects at day 7 and 14 for both the control (PBS) and beta-aminoproprionitrile (BAPN) groups. (A) Femoral % empty lacunae decreased from 7 days to 14 days ($p < 0.01$) in the BAPN group only, but there was no change in the PBS control group. (B) Femoral defect # lacunae/bone area remained unchanged. (C) Maxillary defect % empty lacunae showed no significant change with time of healing or BAPN treatment. (D) Maxillary defect # lacunae/bone area showed no significant change with time of healing or BAPN treatment. *$p < 0.05$, **$p < 0.001$, ***$p < 0.0001$, 2-way ANOVA.

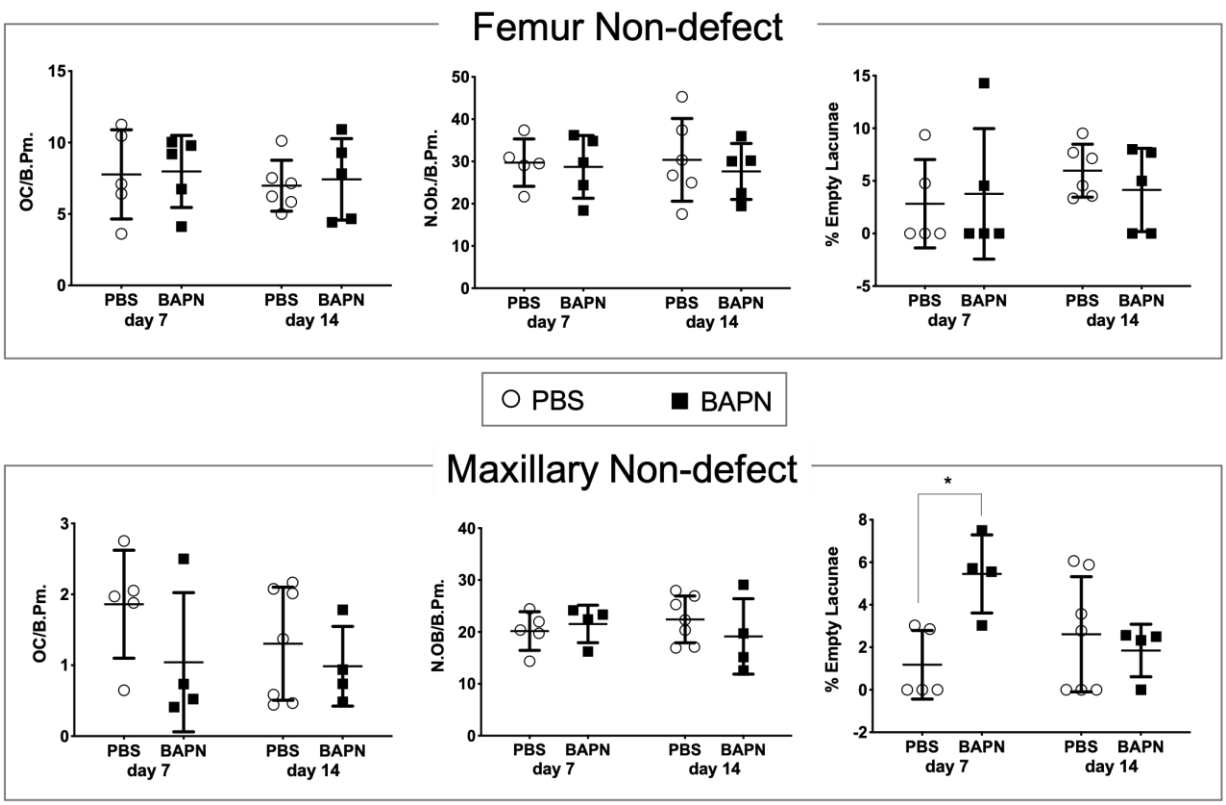

Figure 4.10S2 Non-defect sites (pre-maxillary suture or distal femur trabeculae) of tartrate resistant alkaline phosphatase (TRAP) staining to highlight osteoclasts and masons trichrome staining to highlight collagen for the defects at day 7 and 14 for both the control (PBS) and beta-aminoproprionitrile (BAPN) groups were quantified for changes to osteoclasts, osteoblasts and % empty lacunae. Of these, only the maxillary non-defect % empty lacunae showed an increase with BAPN treatment at day 7 ($p < 0.05$). *$p < 0.05$, **$p < 0.001$, ***$p < 0.0001$, 2-way ANOVA.

4.7 References

1. Shibuya N, Humphers JM, Fluhman BL, Jupiter DC. Factors Associated with Nonunion, Delayed Union, and Malunion in Foot and Ankle Surgery in Diabetic Patients. The Journal of Foot and Ankle Surgery. 2013 Mar 1;52(2):207–11.

2. Patel RA, Wilson RF, Patel PA, Palmer RM. The effect of smoking on bone healing. Bone & Joint Research. The British Editorial Society of Bone & Joint Surgery; 2013 Jun 1;2(6):102–11.

3. Jegoux F, Malard O, Goyenvalle E, Aguado E, Daculsi G. Radiation effects on bone healing and reconstruction: interpretation of the literature. Oral Surgery, Oral Medicine, Oral Pathology, Oral Radiology, and Endodontology. 2010 Feb 1;109(2):173–84.

4. Chang J, Hakam AE, McCauley LK. Current Understanding of the Pathophysiology of Osteonecrosis of the Jaw. Curr Osteoporos Rep. 2018 Oct 1;16(5):584–95.

5. Daley EJ, Pajevic PD, Roy S, Trackman PC. Impaired Gastric Hormone Regulation of Osteoblasts and Lysyl Oxidase Drives Bone Disease in Diabetes Mellitus. JBMR Plus. 2019;3(10):e10212.

6. Mandair GS, Oest ME, Mann KA, Morris MD, Damron TA, Kohn DH. Radiation-induced changes to bone composition extend beyond periosteal bone. Bone Reports. 2020 Jun 1;12:100262.

7. Khalid M, Bora T, Ghaithi AA, Thukral S, Dutta J. Raman Spectroscopy detects changes in Bone Mineral Quality and Collagen Cross-linkage in Staphylococcus Infected Human Bone. Sci Rep. 2018 Jun 20;8(1):9417.

8. Cusano NE. Skeletal Effects of Smoking. Curr Osteoporos Rep. 2015 Oct 1;13(5):302–9.

9. Mubarak S, Masako N, Al-Omari FA, Keisuke H, Katsumi U. Effect of Collagen Cross-Link Deficiency on Incorporation of Grafted Bone. Dent J. 2019 May 1;7(2):1-12.

10. Mendes EM, Irie MS, Rabelo GD, Borges JS, Dechichi P, Diniz RS, Soares PBF. Effects of ionizing radiation on woven bone: influence on the osteocyte lacunar network, collagen maturation, and microarchitecture. Clin Oral Invest. 2020 Aug;24(8):2763–71.

11. Mouraret S, Hunter DJ, Bardet C, Brunski JB, Bouchard P, Helms JA. A pre-clinical murine model of oral implant osseointegration. Bone. 2014 Jan 1;58:177–84.

12. McNerny EMB, Gardinier JD, Kohn DH. Exercise increases pyridinoline cross-linking and counters the mechanical effects of concurrent lathyrogenic treatment. Bone. 2015 Dec 1;81:327–37.

13. McNerny EM, Gong B, Morris MD, Kohn DH. Bone Fracture Toughness and Strength Correlate With Collagen Cross-Link Maturity in a Dose-Controlled Lathyrism Mouse Model. Journal of Bone and Mineral Research. 2015;30(3):455–64.

14. Khosravi R, Trackman PC. Diabetes-induced fibrotic matrix inhibits intramembranous bone healing. J. Cell Commun. Signal. 2015 Mar 1;9(1):19–26.

15. Schindelin J, Arganda-Carreras I, Frise E, Kaynig V, Longair M, Pietzsch T, Preibisch S, Rueden C, Saalfeld S, Schmid B, Tinevez J-Y, White DJ, Hartenstein V, Eliceiri K, Tomancak P, Cardona A. Fiji: an open-source platform for biological-image analysis. Nat Methods. 2012 Jul;9(7):676–82.

16. Parfitt AM, Drezner MK, Glorieux FH, Kanis JA, Malluche H, Meunier PJ, Ott SM, Recker RR. Bone histomorphometry: Standardization of nomenclature, symbols, and units. Report of the ASBMR Histomorphometry Nomenclature Committee. J Bone Miner Res. 1987; 2:595–610.

17. Ida T, Kaku M, Kitami M, Terajima M, Rocabado JMR, Akiba Y, Nagasawa M, Yamauchi M, Uoshima K. Extracellular matrix with defective collagen cross-linking affects the differentiation of bone cells. PLoS ONE. 2018 Sep 25:13(9): e0204306.

18. Bredfeldt JS, Liu Y, Pehlke CA, Conklin MW, Szulczewski JM, Inman DR, Keely PJ, Nowak RD, Mackie TR, Eliceiri KW. Computational segmentation of collagen fibers from second-harmonic generation images of breast cancer. J Biomed Opt. 2014 Jan;19(1):016007.

19. Sinder BP, Zweifler L, Koh AJ, Michalski MN, Hofbauer LC, Aguirre JI, Roca H, McCauley LK. Bone Mass Is Compromised by the Chemotherapeutic Trabectedin in Association With Effects on Osteoblasts and Macrophage Efferocytosis. Journal of Bone and Mineral Research. 2017;32(10):2116–27.

20. Sinder BP, Lloyd WR, Salemi JD, Marini JC, Caird MS, Morris MD, Kozloff KM. Effect of anti-sclerostin therapy and osteogenesis imperfecta on tissue-level properties in growing and adult mice while controlling for tissue age. Bone. 2016 Mar 1;84:222–9.

21. Wu Z, Ovaert TC, Niebur GL. Viscoelastic properties of human cortical bone tissue depend on gender and elastic modulus. Journal of Orthopaedic Research. 2012;30(5):693–9.

22. Oliver WC, Pharr GM. An improved technique for determining hardness and elastic modulus using load and displacement sensing indentation experiments. Journal of Materials Research. Cambridge University Press; 1992 Jun;7(6):1564–83.

23. Gomes-Ferreira PHS, de Oliveira D, Frigério PB, de Souza Batista FR, Grandfield K, Okamoto R. Teriparatide improves microarchitectural characteristics of peri-implant bone in orchiectomized rats. Osteoporos Int. 2020 Sep;31(9):1807–15.

24. Faraz MI, Besseling N a. M, Korobko AV, Picken SJ. Characterization and modeling of creep behavior of a thermoset nanocomposite. Polymer Composites. 2015;36(2):322–9.

25. Hwang MP, Subbiah R, Kim IG, Lee KE, Park J, Kim SH, Park K. Approximating bone ECM: Crosslinking directs individual and coupled osteoblast/osteoclast behavior. Biomaterials. 2016 Oct 1;103:22–32.

26. Saito M, Marumo K. Collagen cross-links as a determinant of bone quality: a possible explanation for bone fragility in aging, osteoporosis, and diabetes mellitus. Osteoporos Int. 2010 Feb 1;21(2):195–214.

27. Cai L, Zhang D, Liu W, Cui Y, Jing J, Xie J, Zhou X. Effects of parathyroid hormone (1-34) on the regulation of the lysyl oxidase family in ovariectomized mice. RSC Advances. Royal Society of Chemistry; 2018;8(53):30629–41.

28. Schurman CA, Verbruggen SW, Alliston T. Disrupted osteocyte connectivity and pericellular fluid flow in bone with aging and defective TGF-β signaling. Proc Natl Acad Sci USA. 2021 Jun 22;118(25):e2023999118.

29. Henriksen K, Bollerslev J, Everts V, Karsdal MA. Osteoclast Activity and Subtypes as a Function of Physiology and Pathology—Implications for Future Treatments of Osteoporosis. Endocrine Reviews. 2011 Feb 1;32(1):31–63.

30. Kayal RA, Tsatsas D, Bauer MA, Allen B, Al-Sebaei MO, Kakar S, Leone CW, Morgan EF, Gerstenfeld LC, Einhorn TA, Graves DT. Diminished Bone Formation During Diabetic Fracture Healing is Related to the Premature Resorption of Cartilage Associated With Increased Osteoclast Activity. Journal of Bone and Mineral Research. 2007;22(4):560–8.

31. Michalski MN, Zweifler LE, Sinder BP, Koh AJ, Yamashita J, Roca H, McCauley LK. Clodronate-Loaded Liposome Treatment Has Site-Specific Skeletal Effects. J Dent Res. SAGE Publications Inc; 2019 Apr 1;98(4):459–67.

32. Chaichanasakul T, Kang B, Bezouglaia O, Aghaloo TL, Tetradis S. Diverse Osteoclastogenesis of Bone Marrow From Mandible Versus Long Bone. Journal of Periodontology. 2014;85(6):829–36.

33. Lin H-N, O'Connor JP. Osteoclast depletion with clodronate liposomes delays fracture healing in mice. J Orthop Res. 2017 Aug;35(8):1699–706.

Chapter 5.
Discovery of a Novel Serum Detectable Bone Collagen Cross-link

5.1 Introduction

It critically important to develop additional methods to estimate bone quality. Traditional clinical methods of determining bone mineral density (BMD) via the gold standards, dual X-ray absorptiometry (DEXA) or peripheral quantitative computed tomography (pQCT), do not consistently predict fracture risk. In the Rotterdam study, ~18% of men and ~13% of women[(1)] having a normal BMD still experienced fracture. This clinical study highlights that for a large portion of the population DEXA fails to identify patients at risk for fracture. More recently, an emphasis is being put on understanding the contribution of structural properties: size, shape and microarchitecture as well as material properties: microdamage, mineral-to-matrix ratio, mineral crystal size, collagen type and cross-links, to determine bone quality[(2)(3)(4)(5)]. Since bone is a composite material, comprised of both mineral (confers the property of stiffness) and collagen (provides tensile strength, toughness, and ductility), understanding both compartments is critical to understanding fracture risk.

Bone collagen cross-links form either enzymatically or non-enzymatically, with different resulting mechanical properties depending on the amount, proportion and level of modification. Most cross-links occur enzymatically via lysyl hydroxylase (LH) and lysyl oxidase (LOX) enzymes which catalyze the formation of the immature and mature cross-links. The immature, or reducible, cross-links are the dehydro-dihydroxylysinonorleucine (deh-DHLNL) and dehydro-hydroxylysinonorleucine (deh-HLNL). The mature cross-links are the non-reducible cross-links (pyridinoline (PYD), deoxypyridinoline (DPD) or the pyrroles) and form from addition of a hydroxyallysine to the deh-DHLNL or deh-HLNL, respectively. Studies of altered collagen cross-links by chemical inhibition of enzymatic cross-link formation have shown that the ratios of mature to immature cross-links contributes to the whole bone fracture toughness in mice, while ratios of different mature cross-links are significant contributors to tissue strength[(6)]. In

studies of human bone, by introducing age (a covariate for the non-enzymatic collagen cross-links) and immature cross-link content (DHLNL/HLNL) to total mineral density (TMD), predictive capacity of tissue level strength nearly doubled to an R^2 of 0.56[3]. Together, these findings highlight the importance of analyzing both the mineral and collagen components of bone for better prediction of tissue level mechanical properties.

Clinical assessment of collagen can only be done invasively via a biopsy to yield samples for direct measures of collagen via high performance liquid chromatography (HPLC). Such invasive and destructive methods are therefore is not widely used clinically. Mature, trivalent, collagen cross-links in bone (pyridinoline and deoxypyridinoline) can be measured by urine and serum using commercially available enzyme-linked immunosorbent assays (ELISA) raised against the pyridinoline bound peptides or HPLC[7] measurements of free pyridinolines. Together these cross-link fragments are used clinically as markers of bone resorption and turnover. Serum detectable cross-links are primarily from the skeleton due to the more rapid turnover rate of bone compared to other tissues[7]. The surrogate measures of bone turnover are the collagen degradation products, amino- (N) and carboxy- (C) terminal telopeptides (NTx, CTx, respectively) and free pyridinolines, and have shown promise for screening and monitoring for a variety of diseases such as Pagets[8], cancer metastasis to bone[9], and osteoporosis[10]. However, there is wide variation between individuals in these laboratory values and conflicting reports on their relationship to bone density and predictive value for fracture risk[11][12].

The pyridinoline cross-links are found in collagen in cartilage, bone, ligament and blood vessels while deoxypyridinoline is thought to be exclusive to bone and dentin[13]. Yet, these mature cross-links are not the predominant cross-links in bone. Likely due to the increased turnover rate compared to other tissues, bone has a higher ratio of immature/mature cross-links[14][15][6]. However, immature cross-links, deh-DHLNL and deh-HLNL, to our knowledge, have not been detected in serum or any other body fluids. Immature cross-links may have been overlooked due to additional processing steps required *ex vivo* using sodium borohydride to reduce them in their stable, reduced forms, DHLNL and HLNL, that are resistant to acid hydrolysis. However, like the other enzymatic cross-links, these immature cross-links are also located between the terminal telopeptides and the helix of two collagen molecules[16][13](Figure 5.1, adapted from Seibel, 2005[13]). These telopeptide regions are then degraded during bone

turnover by osteoclasts and released into serum. This is the form from which serum detectable mature cross-links were first identified and shown to correlate with bone turnover[17][18]. Therefore, I hypothesized that immature cross-links DHLNL and HLNL (measured in reduced form), are detectible in serum at higher ratios than mature pyridinolines. This is the first report of measurement of immature cross-links in mouse and human serum. This discovery presents a valuable tool to work towards correlating serum detectable cross-links with collagen cross-links measured directly from bone as a first step towards investigating the potential use of a broad panel of serum detectable cross-links as a non-invasive indicator of bone quality.

5.2 Methods

5.2.1 Serum Samples

All animal procedures were approved by Institutional Animal Care & Use Committee (IACUC) at the University of Michigan. 12-week old, male C57Bl6 (Charles River) were euthanized by CO_2 inhalation and cardiac puncture was performed to collect the maximum volume of whole blood. Blood was allowed to clot at room temperature in a 1.5 mL Falcon tube for 1 hour, then centrifuged at 8000 RPM for 15 min. A clear supernatant formed and was removed and stored as whole serum. Human serum was purchased (Sigma-Aldrich, H6914), aliquoted and stored at - 20 C until used for analysis.

5.2.2 Protein Quantification, Depletion and Visualization

Protein interferes with subsequent processing steps (Figure 5.2) for analysis of the collagen cross-links, therefore large molecular weight proteins (albumins and IgG's, > 65 kDa MW) must be depleted. To assess efficiency of > 65 kDa MW protein depletion, quantification using a Bradford assay (Sigma, B6916) was performed against a bovine serum albumin (Sigma, A7906) standard. Protease inhibitor cocktail (ThermoFisher, #78410) was added to serum per manufacturer's instructions.

Depletion was done by mixing the starting volume of raw serum with ice cold acetonitrile (ACN) (Fisher, A9554) in a 1:2 ratio (serum: ACN), vortexing for 5 seconds, letting sit on ice for 30 min. Samples were then centrifuged at 13,000 RPM for 15 min. The resulting supernatant was

removed (as well as equivalent volumes of un-depleted serum), dried using a vacuum line, and resuspended in original volume of water (Fisher, W6-4). Raw serum samples were then diluted 1:100 in Milli-Q water, depleted serum was used as is. The Bradford assay was then conducted per manufacturer's instructions (Sigma, B6916-500ML) and allowed to react in the dark for 10 min and protein concentration was read at UV wavelength (λ) 595 nm.

A starting concentration of 2 μg/uL of protein in raw serum (or equivalent starting volume of protein depleted serum) was mixed with 2x laemmli buffer (Bio-Rad, #161-0737) containing 5% beta-mercaptoethanol, denatured on a heat block (70^0C) for 10 minutes, loaded onto a 4-20% Tris-Glycine SDS-PAGE gel and ran at 225 mV for 45 min. Proteins were fixed in place with 40% deionized water (DI), 10% acetic acid, 50% methanol solution) for two hours. The gel was stained with Coomassie stain (40% DI water, 10% acetic acid, 50% methanol solution and an additional 0.25% (by weight) Brilliant Blue R-250 (ThermoFisher, 20278)) overnight. Excess dye was removed with 67.5% DI water, 7.5% acetic acid, 25% methanol over the course of 36 hr. Protein bands were then imaged using a ChemiDock MP Imaging System.

5.2.3 Cross-link Quantification via LC-MS

Serum processing for cross-link detection via Ultra-high performance liquid chromatography with tandem mass spectrometry (LC-MS) is outlined in Figure 5.2. Serum was first reduced with 0.01 mg/uL sodium borohydride in 1 mM sodium hydroxide over 1 hour producing intense bubbling. The serum was then mixed 1:2 with ice cold ACN and vortexed for 5 seconds, then allowed to precipitate on ice for 30 min. Samples were centrifuged at 13,000 RPM for 15 min. The supernatant was then dried on a heat block (110 C) for 30 min, resuspended in 6 M hydrochloric acid (HCl) in LC-MS water at the same starting volume of raw serum and left on the heat block for 24 hours. Raw serum was also reacted with sodium borohydride, then mixed 1:1 with 12 M HCl and applied to the heat block. Acid hydrolysate fractions were then cleaned via SPE (Chapter 3). Lyophilized samples were suspended in LC-MS grade water spiked with pyridoxine as in internal standard for subsequent LC-MS injection (as presented in Chapter 3). The column was a Hydrophilic interaction liquid chromatography (HILIC) normal phase column (Microsolv, 70000-15P-2). LC-MS (Agilent 6545 LC/Q-TOF). Conditions were as follows: injection volume: 5 μL, gradient elution program: Solvent A, 100%

water/0.1% formic acid (v/v); solvent B, 100% acetonitrile/0.1% formic acid (v/v). Gradient: 0 min 90% solvent B, 2 min 84% solvent B, 12 min 42% solvent B and 17 min 10% solvent B. Total run time was 17 min and flow rate was 0.4 mL/min followed by 4 min of column equilibration time (total run time 21 min), column temp: 25 C.

The mass spectrometer used was the MS Q-TOF equipped with dual Jet Stream Technology Ion Source (AJS) Electrospray ionization spectrometry (ESI). Positive ion mode was used in all runs. System parameters were: column temperature, 35 C; sheath gas (N_2) temperature: 320 C, flow: 10 L/min; Positive ion mode was used with a mass range of 50– 1200 m/z, scan rate: 2 spectra/second. All data were processed using Thermo Xcalibur 3.0 software. Agilent MassHunter Workstation Qualitative Analysis software version B.06.01 SP1 (Agilent Technologies, Santa Clara, CA, USA) was used for qualitative analysis and quantitation. A known mass list (detailed in Table 5.1) was used for extraction of ion chromatograms for quantification as compared to the standard curves for each species of cross-link.

Standards of the PYD (CAS# 63800-01-1, BOCSCI Inc.) and DPD (CAS # 83462-55-9, BOCSCI Inc.) were purchased, DHLNL was purchased from ChemCruz (sc-207059C) and used to quantify HLNL as well since they only differ by an oxygen and no standard is commercially available. CML (Cayman, 16483) and PEN (Cayman, 10010254) were purchased from Cayman Chemical.

5.3 Results

5.3.1 Depletion of High Molecular Weight Proteins from Serum was Required to Detect Collagen Cross-Links via LC-MS

Due to the high sensitivity of LC-MS, overabundance of molecules in the mass range (50 -1200 m/z) of detection limits the ability to detect the cross-links[19]. Previous methods of detection for the mature cross-links could work around this issue by using a reverse phase column with ion-pairing agents. However, this methodology narrows the scope of the MS capabilities as the ion-pair agents interfere with negative ion mode and contaminate the system. The method chosen here uses a HILIC normal phase column to work around the ion-pairing agent issues[20][21]. For the directly hydrolyzed raw serum, an overabundance of molecules (50 –

1200 m/z range) were detected, lacking any peak clarity on the total ion chromatogram (TIC) (Figure 5.3A) whereas with protein precipitation (Figure 5.3C) there were distinguishable peaks formed on the TIC. The internal standard, pyridoxine, signal was also suppressed under hydrolysis conditions (Figure 5.3B, no signal). Decreasing the injection volume marginally improved the signal, but suppression still existed. When protein precipitation was utilized, the pyridoxine signal became clearly distinguishable (Figure 5.3D).

ACN precipitation is a simple, yet effective method for depleting interfering high molecular weight (HMW) proteins (> 65 kDa) such as albumin and IgG, enriching the low molecular weight fraction (LMW) (< 65 kDa). Mouse and human serum were quantified for protein concentration, with mouse serum showing 49,150 ng/μL and human serum containing 33,025 ng/μL (Figure 5.4A). Upon acetonitrile depletion, 5,930 ng/μL remained in mouse serum and 9,665 ng/μL remained in human serum. This resulted in an efficiency of 87.9% depletion in mouse and 70.7% in human (Figure 5.4A). Serum was enriched for LMW proteins via protein precipitation in both species as visualized in the SDS-PAGE (Figure 5.4B). Here, fractions above 65 kDa in the protein precipitation for mouse and human are reduced compared to the raw serum, while still maintaining clear bands in the < 30 kDa range (where telopeptide cross-links would be seen).

5.3.2 Novel Detection of DHLNL and HLNL in Mouse and Human Serum

To the best of my knowledge, immature cross-links have never been detected in serum. Modifying LC-MS methods of detecting cross-links in bone (detailed in Chapter 3) allowed for detection and quantification collagen cross-links via LC-MS in serum. Cross-links were compared to standards of mature cross-links (pyridinoline (PYD), deoxypyridinoline (DPD)), immature cross-links (dihydroxylysinorleucine (DHLNL)), and advanced glycations end products (pentosidine (PEN) and carboxy methyl-lysine (CML)) (Figure 5.5). No commercially available standard exists for and hydroxylysinorleucine (HLNL). The method developed showed clear peaks at the identifiable m/z for each cross-link (Table 5.1).

Mouse serum showed quantifiable peaks for each cross-link (Figure 5.6A), with serum detectible immature cross-links (HLNL: 0.1978 pmol/μL, DHLNL: 0.1227 pmol/μL), mature cross-links (PYD: 0.2676 pmol/μL, DPD: 0.0419 pmol/μL), and advanced glycation end-

products (PEN: 0.8986 pmol/μL, CML: 0.3285 pmol/μL) (Table 5.2). Human serum also showed quantifiable peaks for each cross-link (Figure 5.6A), with serum detectible immature cross-links (HLNL: 0.0515 pmol/μL, DHLNL: 0.0631 pmol/μL), mature cross-links (PYD: 0.1645 pmol/μL, DPD: 0.0261 pmol/μL), and advanced glycation end-products (PEN: 0.4351 pmol/μL, CML: 0.1677 pmol/μL) (Table 5.2). Mouse serum contained 3.84X the amount of HLNL compared to human, while only 1.95X the DHLNL. The mature cross-links had almost identical ratios in mouse to human serum (PYD: 1.63 and DPD: 1.61). The AGE's also had similar ratios (PEN: 2.07, CML: 1.90) (Table 5.2).

5.4 Discussion

The discovery of new serum-detectible collagen cross-links, dihydroxylysinorleucine (DHLNL) and hydroxylysinorleucine (HLNL), while preliminary, could serve as a fundamental expansion in the clinical utility of serum collagen cross-link assays. Currently, serum detectable cross-links are primarily used as a turnover marker. The results of Aim 3 of this dissertation enable the quantification of ratios of immature to mature cross-links, potentially leading to better prediction of disease state or fracture risk.

Recent advances in MS technology have opened avenues for more breadth and depth in quantification of serum detectible collagen cross-links. Chromatography methods are generally coupled with methods of detecting each species of interest. Options include fluorescence, ultraviolet, or mass spectrometry. The specific detection method depends on the inherit properties of each species. Mature cross-links (pyridinoline (PYD) and deoxypyridinoline (DPD)) as well as the AGE, pentosidine (PEN) are naturally fluorescent. However, immature cross-links (dihydroxylysinorleucine (DHLNL) and hydroxylysinorleucine (HLNL) must be reacted with *o*-pthaldehyde to be detected via fluorescence[6][23][3], yet known chemical formulas allow for detection via mass spectrometry). Additionally, the AGE, carboxy methyl-lysine (CML) is non-fluorescent and has only recently been measured directly in human bone[24] and mouse bone (Chapter 3) (both via LCMS). Depletion of the high molecular weight protein fraction (> 65 kDa)(Figure 5.4) was necessary to reduce the number of interfering compounds (< 1200 m/z) to allow for adequate detection of the internal standard (pyridoxine) (Figure 5.3) as well as the cross-links (not detectible without protein precipitation, data not shown).

The serum processing and LC-MS analysis presented in this work revealed not only the mature (PYD, DPD) and AGE (CML, PEN) cross-links, but also the detection of the immature (HLNL, DHLNL) cross-links for the first time in mouse and human serum (Figure 5.6, Table 5.2). These cross-links varied in concentration from ~0.2 pmol/μL to 0.9 pmol/μL), depending on species and cross-link. For mouse serum, the most abundant cross-link was PEN followed by CML. These cross-links are not bone specific and therefore their high abundance is not a surprise and well documented[27][28]. PYD was the next most abundant mouse serum cross-link, followed by HLNL, DHLNL, then DPD. Human serum cross-links followed the same trend in prevalence, except DHLNL had slightly higher amounts than HLNL (Table 5.2). Ratios of mouse to human serum cross-links showed the greatest separation in the relative pmol/uL of HLNL (3.84X more in mouse than human), whereas all other cross-links were around 1.6-2X higher in mouse than human. One explanation for the increased HLNL could be that the mouse serum was from a 12-week old mouse (static, middle aged mouse timepoint yet still likely younger than human), whereas the human serum was pooled from a number of male human donors and therefore age may not have been controlled. Additionally, the increase in cross-links per similar volume of serum for mouse compared to human is of interest. A possible explanation is that protein content was also higher, so it is possible that mice have more "concentrated" serum than humans as a whole.

While my original hypothesis was that the immature cross-links would be detectible in higher amounts than the mature cross-links, the opposite is reported here, yet more experiments will be needed to fully determine if this was a product of the groups analyzed or a universal phenomenon. An explanation for the increase in PYD compared to HLNL and DLNL is that of the enzymatic cross-links described, PYD is the least "specific" to bone, as the abundance of PYD is much higher in tissues with low turnover rates such as skin[20]. HLNL and DHLNL are the predominant cross-link in bone, and DPD is thought to be relatively specific to bone[25] and diminish with disease such as osteoporosis[26]. While specificity of these cross-links to bone is not proven here, a wide array of studies show that immature/mature collagen cross-link ratios are higher in long bones than other tissues[25]. The mouse ratio of immature/mature was 1.03, whereas the human ratio was 0.6 (Table 5.2). These discrepancies between species should be further studied with larger samples size, different ages, and diseases to determine the source of this variation. While these are limitations to the presented data, I believe that the presence of

both HLNL and DHLNL in two species is supporting evidence of the mechanisms as hypothesized, that they originate in the type I collagen and are excreted during the degradation of bone via osteoclasts. However, this was not directly tested in this study.

While cross-links from bone should dominate the serum profile due to the higher turnover rate of bone compared to other tissues, studies should be conducted to determine the direct contribution of bone cross-links to serum cross-links. However, the detection of plasma pentosidine, a non-enzymatically formed collagen cross-link, is linearly correlated with patients' cortical bone pentosidine levels[27] and positively associated with vertebral fractures in diabetic patients[28]. Increased pentosidine levels are detrimental to bone mechanical properties as measured directly[29] and by serum[28]. Therefore, serum concentrations of pentosidine can serve as a surrogate for bone quality despite bone not being the only source of pentosidine in serum. Likewise, our next steps are to measure the full set of cross-links (PYD, DPD, HLNL, DHLNL, PEN, CML) in serum and correlate to directly measurable cross-links in bone of the same animal. Future studies should focus also on diseases of bone or a collagen perturbation model, such as in Chapters 3 and 4, to determine the contribution of direct bone cross-link changes to serum.

5.5 Conclusions

Here we presented quantification of immature cross-links in serum for the first time in mouse and human serum. This discovery was made possible by depleting high molecular weight proteins and processing the serum with an additional reduction and hydrolysis steps to select for acid resistant cross-link species. These cross-links included a full panel of bone related crosslinks including the mature (PYD, DPD), the novel detection of the immature (HLNL, DHLNL), and advanced glycation end products (PEN, CML). It is of interest to further study the specificity of the full suite of collagen cross-links in serum to direct measurements of cross-links from bone. The ability to survey these cross-links as a "liquid biopsy" of the bone would allow for minimally invasive real-time monitoring of bone cross-link status. Such a diagnostic could provide information over time and with aging and may provide better indication of fracture risk or diseases effecting enzymatic and non-enzymatic cross-linking.

5.6 Acknowledgements

I would like to thank my co-authors: Benjamin Sexton, Morgan Bolger, David H. Kohn. I would like to thank Dr. Wendy Feng for advice on the LC-MS processing and analysis via the Natural Products Core. Research reported in this publication was supported by the National Institutes of Health NIDCR T32 DE007057, F30 DE028167. Research reported in this publication was also supported by the National Institutes of Health NIAMS P30 AR069620 and RO1 AR065424, RO1 AR068452. Research reported in this publication was also supported by the University of Michigan School of Dentistry (Dean's Scholarship and Natalie C. Roberts Endowed Professorship). The content is solely the responsibility of the authors and does not necessarily represent the official views of the National Institute of Health or the University of Michigan School of Dentistry.

5.7 Author Contributions

Study design: GR and DK. Study conduct: GR, BS, and MB. Data collection: GR, BS, and MB. Data analysis: GR and BS. Data interpretation: GR and DK. Drafting manuscript: GR. Revising manuscript content: GR and DK. Approving final version of manuscript: GR, BS, MB, and DK. GR and DK take responsibility for the integrity of the data analysis.

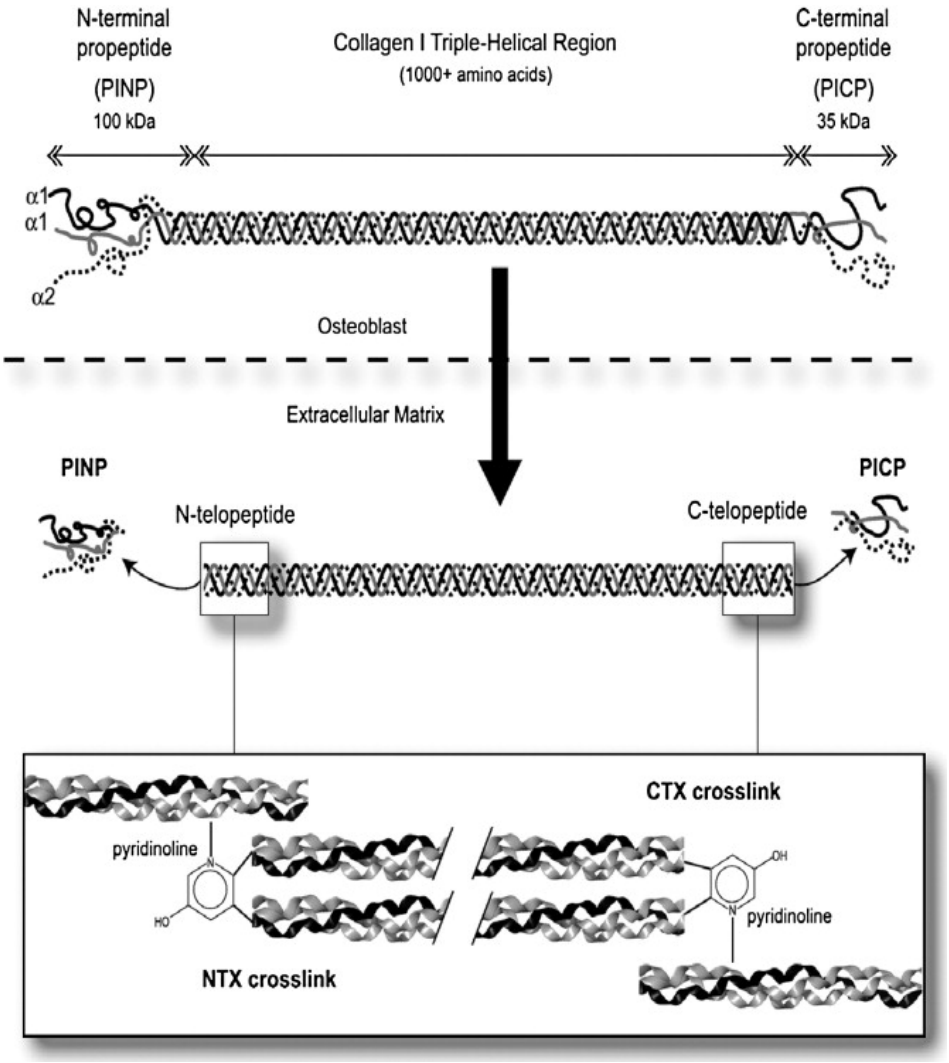

Figure 5.1 Bone collagen serum formation markers are considered to be cleavage products at the N- and C- terminal regions of type I collagen where cross-linking occurs. The subsequent degradation products can be analyzed in serum as the N- and C- terminal propeptides (NTX and CTX, respectively), the non-helical ends of the telopeptide cross-links to nearby helices by mature (trivalent) or theoretically, the immature (divalent) cross-links. Following degradation of the collagen molecules via osteoclasts, the NTX and CTX regions are released into circulation and contain the mature (pyridinoline, deoxypridinoline, and pyrroles) collagen cross-links. I am suggesting that the immature cross-links could also be released following this mechanism as they are also thought to be contained in these NTX and CTX regions (from Herrmann and Seibel, 2008 with permission).

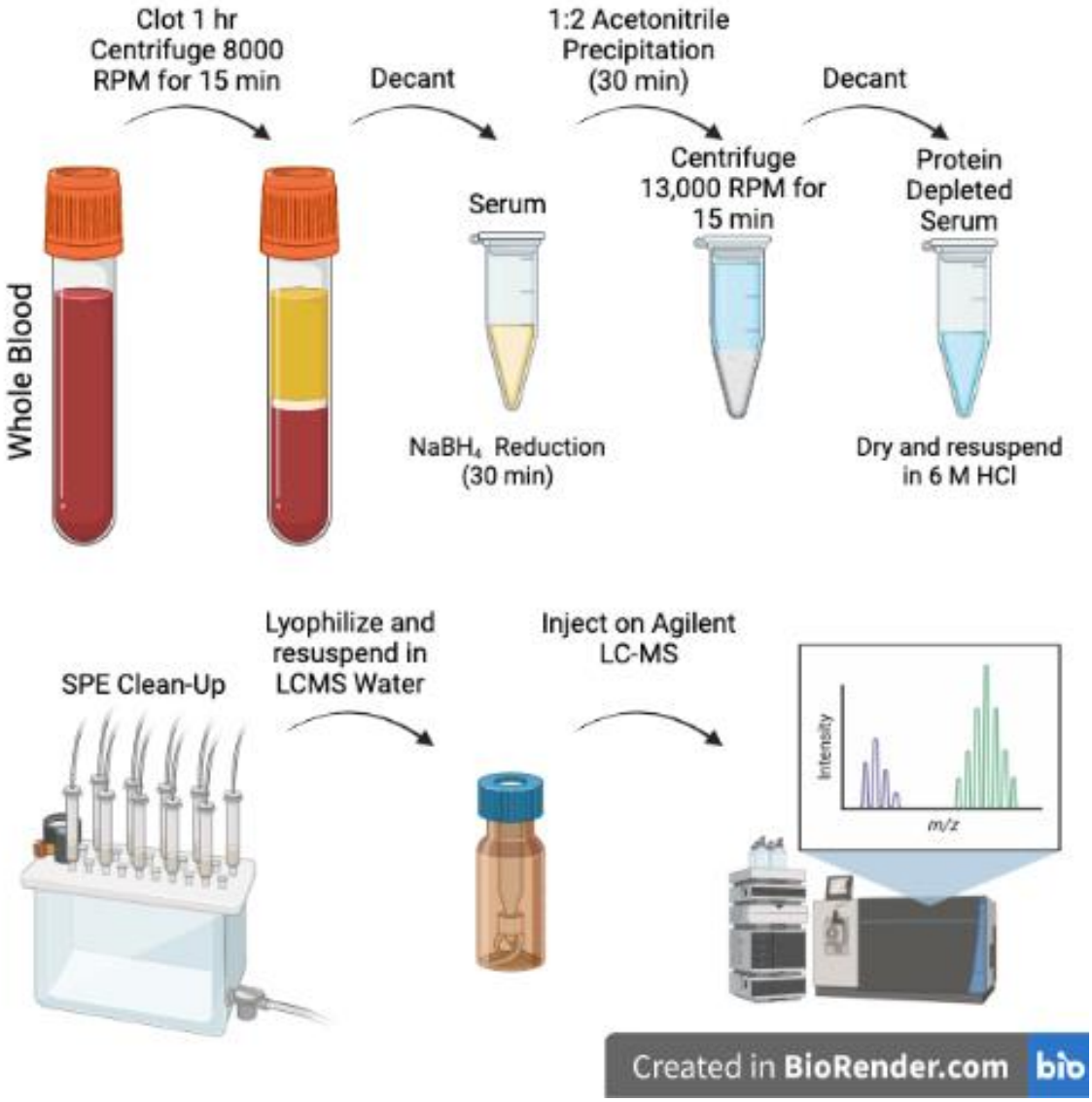

Figure 5.2 Schematic highlighting the workflow optimized for measuring mature and immature collagen cross-links from serum using ultra-high performance liquid chromatography with tandem mass spectrometry (LC-MS). First, whole blood is processed for collection of serum via clotting at room temperature followed by centrifugation. The serum is then removed and reacted with sodium borohydride ($NaBH_4$) for 30 minutes. The protein is then precipitated with 1:2 ratio serum: acetonitrile, vortexed, and allowed to precipitate for 15 minutes followed by centrifugation. The supernatant is decanted and utilized as "High molecular weight depleted serum" for further processing for LC-MS. This includes, acid hydrolysis, solid phase extraction (SPE) cleaning with a series of organic washes and elution with water. Lyophilized samples are resuspended in LC-MS water spiked with internal standard and injected on the LC-MS system. Figure created with BioRender.

Table 5.1 Cross-links of interest with respective chemical formulas, molecular mass, and accurate masses of [M+H]+ charged ions of cross-links. Key: Pyridoxine is the internal standard. Mature cross-links (pyridinoline (PYD), deoxypyridinoline (DPD)), immature cross-links (dihydroxylysinorleucine (DHLNL)), and advanced glycations end products (such as pentosidine (PEN) and carboxy methyl-lysine (CML) (repeated from Chapter 3).

Crosslinks	Formula	Mass (g/mol)	$[M+H]^+$
Pyridoxine	$C_8 H_{11} N O_3$	169.180	170.081
HLNL	$C_{12} H_{25} N_3 O_5$	291.348	292.187
DHLNL	$C_{12} H_{25} N_3 O_6$	307.347	308.182
PYD	$C_{18} H_{28} N_4 O_8$	428.437	429.198
DPD	$C_{18} H_{28} N_4 O_7$	412.433	413.203
PEN	$C_{17} H_{26} N_6 O_4$	378.430	379.209
CML	$C_8 H_{16} N_2 O_4$	204.224	205.118

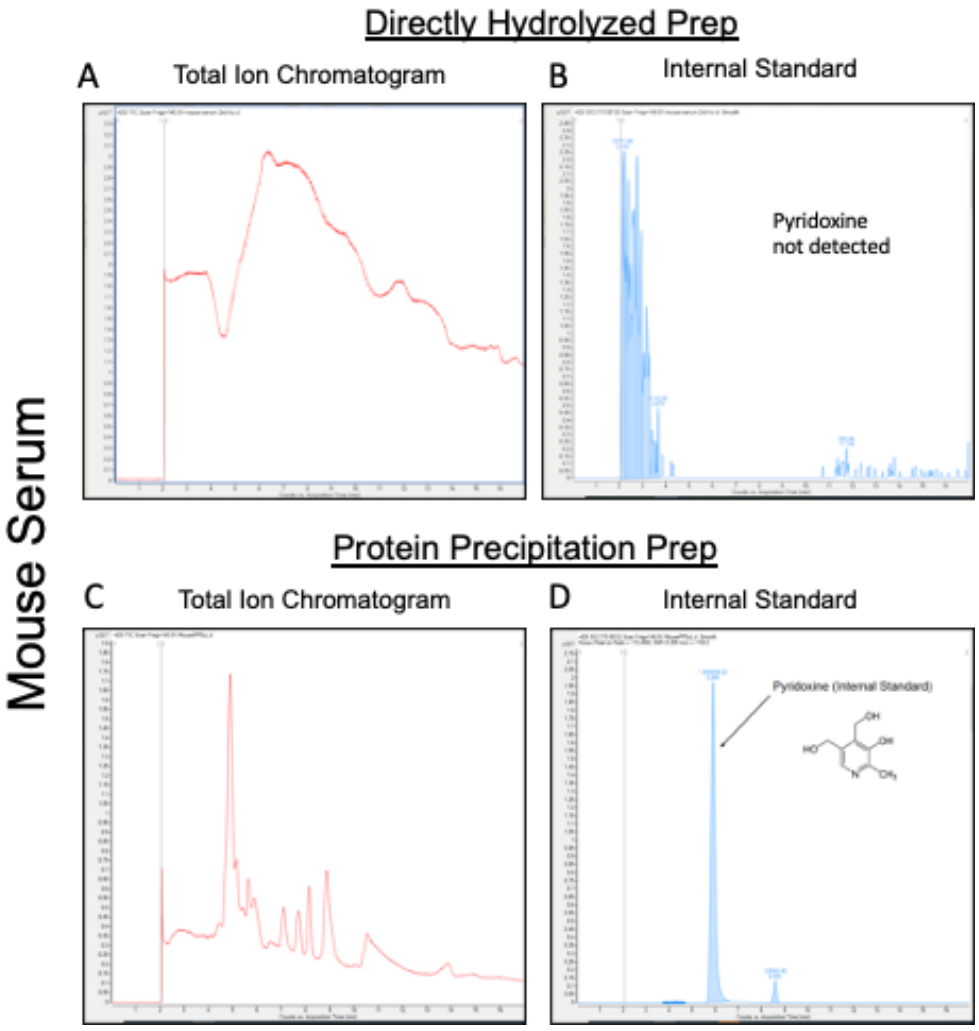

Figure 5.3 Protein precipitation of mouse serum enhances mass spectrometry signal for the internal standard, pyridoxine. (A) Total ion chromatogram for directly hydrolyzed mouse serum (akin to historical preparation of serum for cross-link detection) contained a large fraction of irrelevant signals that diminished detection of the internal standard, pyridoxine, in panel (B). (C) The addition of protein precipitation with 1:2 acetonitrile produced more defined peaks in the total ion chromatogram and (D) enhanced signal of the internal standard, pyridoxine.

A

Serum	Protein Concentration (ng/uL)		
	Raw Serum	Protein Precipitation	% Protein Depleted
Mouse	49,150	5,930	87.9
Human	33,025	9,665	70.7

B

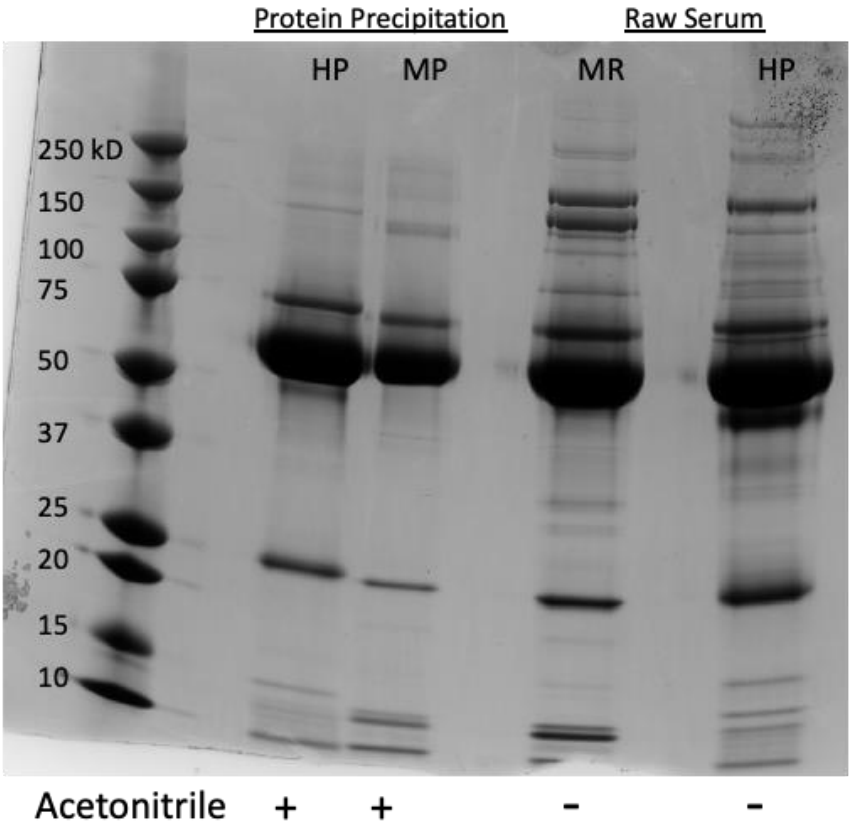

Figure 5.4 Protein precipitation depleted most of the protein in the high molecular weight (HMW) (> 65 kD) fraction. (A) Bradford assay results of raw serum revealed that mouse serum contained higher protein ng/μL than human serum. A higher percentage of protein was also depleted in the mouse serum (87.9%) compared to human serum (70.7%). (B) SDS-PAGE of equal protein concentration of either human protein precipitated serum (HP), mouse protein precipitated serum (MP), mouse raw serum (MR), or human raw serum (HR) followed by Coomassie staining showed that protein precipitation removed proportionally more HMW proteins than low molecular weight proteins, where our desired fraction for cross-link analysis lies.

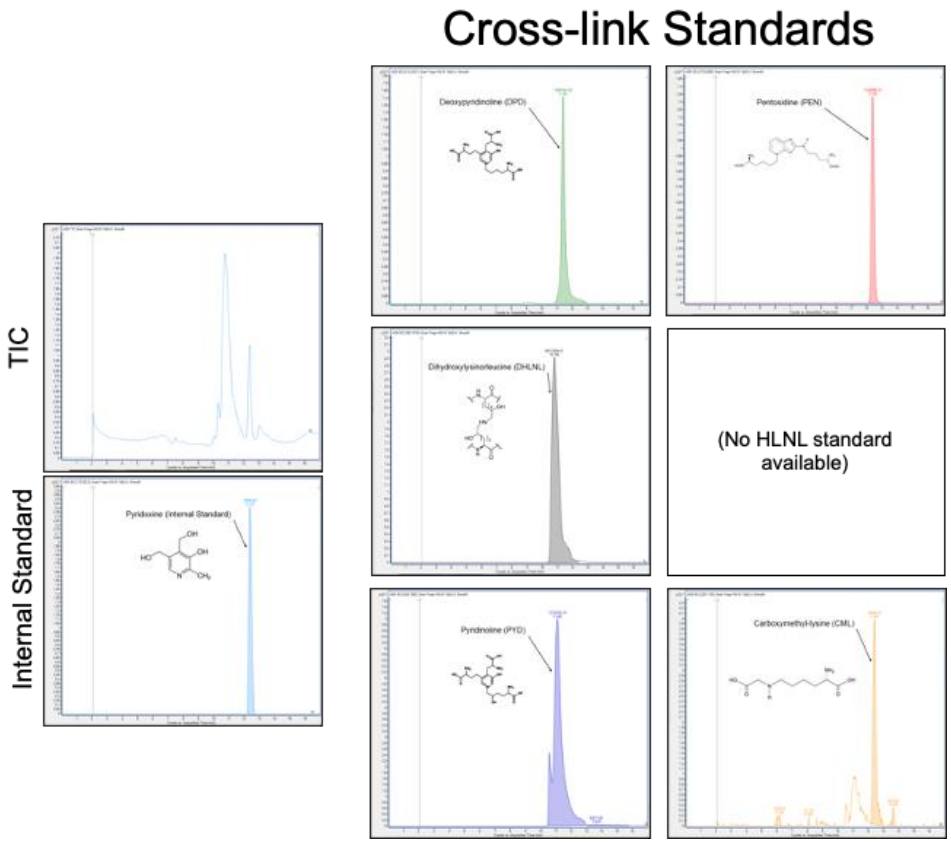

Figure 5.5 Quantification of cross-link standards. Total ion chromatogram (TIC) and extracted ion chromatogram (remaining panels) of the cross-link standards separated on a Cogent Diamond Hydride column. Solvent A, 100% water/0.1% formic acid (v/v); solvent B, 100% acetonitrile/0.1% formic acid (v/v). Gradient: 0 min 90% solvent B, 2 min 84% solvent B, 12 min 42% solvent B and 17 min 10% solvent B. Total run time was 17 min and flow rate was 0.4 mL/min.

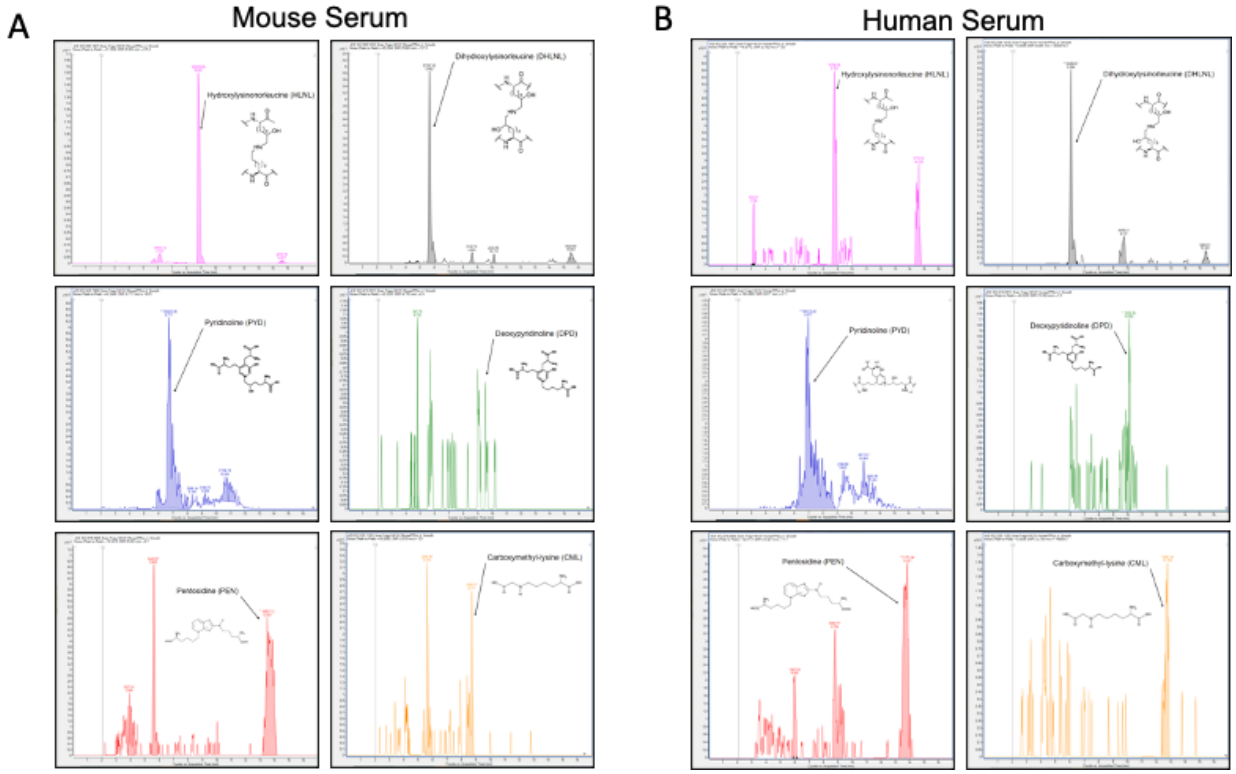

Figure 5.6 Chromatograms of cross-links in mouse and human serum. Extracted ion chromatogram (remaining panels) of the cross-links from mouse serum (A) and human serum (B), both separated on a Cogent Diamond Hydride column (following the same protocol as the standards presented in Figure 5.5). Solvent A, 100% water/0.1% formic acid (v/v); solvent B, 100% acetonitrile/0.1% formic acid (v/v). Gradient: 0 min 90% solvent B, 2 min 84% solvent B, 12 min 42% solvent B and 17 min 10% solvent B. Total run time was 17 min and flow rate was 0.4 mL/min.

Table 5.2 Summary of serum detectible collagen cross-links in mouse and human serum. Mature cross-links (pyridinoline (PYD), deoxypyridinoline (DPD)), immature cross-links (dihydroxylysinorleucine (DHLNL)), and advanced glycations end products (such as pentosidine (PEN) and carboxy methyl-lysine (CML)). Ratios of the mouse (pmol/μL) to human (pmol/μL) for each cross-link are also presented.

Serum			
Cross-links	Mouse (pmol/μL)	Human (pmol/μL)	Ratio (Mouse/Human)
HLNL	0.1978	0.0515	3.84
DHLNL	0.1227	0.0631	1.95
PYD	0.2676	0.1645	1.63
DPD	0.0419	0.0261	1.61
PEN	0.8986	0.4351	2.07
CML	0.3185	0.1677	1.90

5.8 References

1. Schuit SCE, van der Klift M, Weel AE a. M, de Laet CEDH, Burger H, Seeman E, Hofman A, Uitterlinden AG, van Leeuwen JPTM, Pols H a. P. Fracture incidence and association with bone mineral density in elderly men and women: the Rotterdam Study. Bone. 2004 Jan;34(1):195–202.

2. Felsenberg D, Boonen S. The bone quality framework: Determinants of bone strength and their interrelationships, and implications for osteoporosis management. Clinical Therapeutics. 2005 Jan 1;27(1):1–11.

3. Bolger MW, Romanowicz GE, Bigelow EMR, Ward FS, Ciarelli A, Jepsen KJ, Kohn DH. External bone size identifies different strength-decline trajectories for the male human femora. Journal of Structural Biology. 2020 Dec 1;212(3):107650.

4. Schlecht SH, Bigelow EMR, Jepsen KJ. Mapping the natural variation in whole bone stiffness and strength across skeletal sites. Bone. 2014 Oct 1;67:15–22.

5. Bigelow EM, Patton DM, Ward FS, Ciarelli A, Casden M, Clark A, Goulet RW, Morris MD, Schlecht SH, Mandair GS, Bredbenner TL, Kohn DH, Jepsen KJ. External Bone Size Is a Key Determinant of Strength-Decline Trajectories of Aging Male Radii. Journal of Bone and Mineral Research. 2019;34(5):e3661.

6. McNerny EM, Gong B, Morris MD, Kohn DH. Bone Fracture Toughness and Strength Correlate With Collagen Cross-Link Maturity in a Dose-Controlled Lathyrism Mouse Model. Journal of Bone and Mineral Research. 2015;30(3):455–64.

7. Eyre DR. The specificity of collagen cross-links as markers of bone and connective tissue degradation. Acta Orthopaedica Scandinavica. 1995 Jan;66(sup266):166–70.

8. Alvarez L, Guañabens N, Peris P, Vidal S, Ros I, Monegal A, Bedini JL, Deulofeu R, Pons F, Muñoz-gomez J, Ballesta AM. Usefulness of biochemical markers of bone turnover in assessing response to the treatment of paget's disease. Bone. 2001 Nov 1;29(5):447–52.

9. Coleman RE. The clinical use of bone resorption markers in patients with malignant bone disease. Cancer. 2002;94(10):2521–33.

10. Herrmann M, Seibel M. The amino- and carboxyterminal cross-linked telopeptides of collagen type I, NTX-I and CTX-I: A comparative review. Clinica Chimica Acta. 2008 Jul 17;393(2):57–75.

11. Garnero P, Sornay-Rendu E, Claustrat B, Delmas PD. Biochemical Markers of Bone Turnover, Endogenous Hormones and the Risk of Fractures in Postmenopausal Women: The OFELY Study. Journal of Bone and Mineral Research. 2000;15(8):1526–36.

12. Chapurlat RD, Garnero P, Brárt G, Meunier PJ, Delmas PD. Serum type I collagen breakdown product (serum CTX) predicts hip fracture risk in elderly women:: The EPIDOS study. Bone. 2000 Aug 1;27(2):283–6.

13. Herrmann M, Seibel M. The amino- and carboxyterminal cross-linked telopeptides of collagen type I, NTX-I and CTX-I: A comparative review. Clin. Chim. Acta. 2008 Jul 17;393(2):57–75.

14. Saito M, Marumo K, Kida Y, Ushiku C, Kato S, Takao-Kawabata R, Kuroda T. Changes in the contents of enzymatic immature, mature, and non-enzymatic senescent cross-links of collagen after once-weekly treatment with human parathyroid hormone (1–34) for 18 months contribute to improvement of bone strength in ovariectomized monkeys. Osteoporos Int. 2011 Aug 1;22(8):2373–83.

15. Saito M, Kida Y, Kato S, Marumo K. Diabetes, Collagen, and Bone Quality. Curr Osteoporos Rep. 2014 Jun 1;12(2):181–8.

16. Knott L, Bailey AJ. Collagen cross-links in mineralizing tissues: A review of their chemistry, function, and clinical relevance. Bone. 1998 Mar 1;22(3):181–7.

17. Robins SP. An enzyme-linked immunoassay for the collagen cross-link pyridinoline. Biochemical Journal. 1982 Dec 1;207(3):617–20.

18. Eyre DR, Koob TJ, Van Ness KP. Quantitation of hydroxypyridinium crosslinks in collagen by high-performance liquid chromatography. Analytical Biochemistry. 1984 Mar 1;137(2):380–8.

19. Das L, Murthy V, Varma AK. Comprehensive Analysis of Low Molecular Weight Serum Proteome Enrichment for Mass Spectrometric Studies. ACS Omega. American Chemical Society; 2020 Nov 10;5(44):28877–88.

20. Naffa R, Watanabe S, Zhang W, Maidment C, Singh P, Chamber P, Matyska MT, Pesek JJ. Rapid analysis of pyridinoline and deoxypyridinoline in biological samples by liquid chromatography with mass spectrometry and a silica hydride column. Journal of Separation Science. 2019;42(8):1482–8.

21. Naffa R, Holmes G, Ahn M, Harding D, Norris G. Liquid chromatography-electrospray ionization mass spectrometry for the simultaneous quantitation of collagen and elastin crosslinks. Journal of Chromatography A. 2016 Dec 23;1478:60–7.

22. Identification of High-Risk Individuals for Hip Fracture: A 14-Year Prospective Study - Nguyen - 2005 - Journal of Bone and Mineral Research - Wiley Online Library [Internet]. [cited 2021 Jul 1]. Available from: https://asbmr.onlinelibrary.wiley.com/doi/full/10.1359/JBMR.050520

23. McNerny EMB, Gardinier JD, Kohn DH. Exercise increases pyridinoline cross-linking and counters the mechanical effects of concurrent lathyrogenic treatment. Bone. 2015 Dec 1;81:327–37.

24. Arakawa S, Suzuki R, Kurosaka D, Ikeda R, Hayashi H, Kayama T, Ohno R, Nagai R, Marumo K, Saito M. Mass spectrometric quantitation of AGEs and enzymatic crosslinks in human cancellous bone. Scientific Reports. Nature Publishing Group; 2020 Nov 2;10(1):18774.

25. Saito M, Marumo K. Effects of Collagen Crosslinking on Bone Material Properties in Health and Disease. Calcif Tissue Int. 2015 Sep 1;97(3):242–61.

26. Oxlund H, Mosekilde L, Ortoft G. Reduced concentration of collagen reducible cross links in human trabecular bone with respect to age and osteoporosis. Bone. 1996 Nov;19(5):479–84.

27. Odetti P, Rossi S, Monacelli F, Poggi A, Cirnigliaro M, Federici M, Federici A. Advanced Glycation End Products and Bone Loss during Aging. Annals of the New York Academy of Sciences. 2006 Jan 9,1043(1):710-717.

28. Yamamoto M, Yamaguchi T, Yamauchi M, Yano S, Sugimoto T. Serum Pentosidine Levels Are Positively Associated with the Presence of Vertebral Fractures in Postmenopausal Women with Type 2 Diabetes. The Journal of Clinical Endocrinology & Metabolism. 2008 Mar 1,3(93):1013-1019.

29. Saito M, Fujii K, Mori Y, Marumo K. Role of collagen enzymatic and glycation induced cross-links as a determinant of bone quality in spontaneously diabetic WBN/Kob rats. Osteoporos Int. 2006 Oct 1;17(10):1514–23.

Chapter 6.
Conclusions and Future Directions

6.1 Bone Matrix Composition and Response to Cross-link Perturbation are Anatomically Site-Dependent

Craniofacial and long bones are derived from different cell types, embryologically[1], and are uniquely susceptible to certain pathologies[2][3][4] that also display altered bone composition (collagen or mineral). However, limited studies exist that directly compare bone matrix composition (i.e. collagen cross-links and mineral quantity and quality) or mechanics (modulus, harness, stiffness, or viscoelastic properties) between craniofacial and long bones. The work presented in Chapter 3 of this thesis highlights the differences in bone matrix composition (Figure 3.3) between the mouse mandible and femur. Data in Chapter 3 also demonstrates differences in susceptibility of each bone to alterations in mineral following alterations in collagen cross-linking. While initially it was hypothesized that mineral apposition rate (MAR) would drive compositional differences as is the case with long bones[5], the low mineral carbonation in the mandible independent of MAR indicates that different processes drive mineralization in craniofacial bones and long bones (Figure 3.1, Figure 3.5, Table 3.3S). One explanation for the different response to collagen alteration is that the mandible contains more mature/immature cross-links compared to the femur (Figure 3.3). While the mature cross-links were significantly decreased via beta-aminoproprionitrile (BAPN) inhibition of lysyl oxidase (LOX) (Figure 3.4), the mandible did not display any change in mineral carbonation (Figure 3.5). Conversely, the femur did not display a significant change in mature cross-links (Figure 3.4) yet a significant increase in carbonation of the mineral occurred in response to BAPN (Figure 3.5). These results suggest that either an increased mature/immature ratio is protective against carbonation or some unknown compensatory mechanism may exist between the mandible and the femur.

One possible compensatory mechanism could be the amount of the advanced glycation end product, carboxymethyl-lysine (CML), which was directly measured in mouse bone for the first time (Figure 3.3). The CML content was ~22X higher in the mandible than the femur, which is also the first description of an anatomical site dependent accumulation of CML (Figure 3.3). The suggestion of CML "protecting" a bone against an increase in carbonation with perturbed collagen is supported by the trend towards increased CML in the femora treated with BAPN, possibly to counteract any further increase in carbonation (Figure 3.4). The inherit carbonation of the femur was ~30% higher than the mandible, which had dramatically higher CML content. This intriguing finding warrants further investigation into the possibility of CML providing compensatory mechanical or biochemical features to the bone collagen matrix. The current understanding is that CML accumulation is spontaneous and occurs at the same hydroxylysine formation site that immature cross-links compete for. Since there is bone specific accumulation of CML and possibly a compensation mechanism in the femur with BAPN treatment, further studies investigating the direct mechanism of action and functional consequence of CML accumulation is an important future direction. Such studies could be conducted if a verified model of a directly measurable increase in CML could be established. Likely model candidates include aging or diabetes.

6.2 Craniofacial and Long Bone have Altered Healing Rates and Osteoclast Response to BAPN

There are a number of clinical situations where healing is site dependent, such as osteonecrosis of the jaw[(4)]. However, the predominant understanding of bone healing has been derived from investigating anatomical sites in isolation, a vast majority of historical osseous healing studies have been conducted only in long bones in isolation (not in comparison to a craniofacial defect). While there is a growing body of craniofacial bone healing literature[(6)(7)] the direct comparison of long bones v. craniofacial bones has not been well studied. Additionally, the influence of bone matrix composition on the healing rate and mechanical outcomes has not been well studied in either craniofacial or long bones. Changes in composition and mechanical properties are critical signs of disease and identifying changes in these outcomes could identify differential effects of disease at different skeletal sites.

Research presented in Chapter 4 furthered the findings in Chapter 3 (normal growth conditions) by introducing rapid bone formation during healing in a sub-critical osseous defect model with perturbed bone collagen cross-links. The findings showed a bone-dependent reduction in the accrued bone volume in the maxilla (no measurable increase) compared to the femur (60% significant increase), but no change in bone-fill with perturbed collagen in either bone defect (Figure 4.7). The healing rate contrast between the maxilla and femur highlights that the mechanisms driving healing in long bones and craniofacial bones are different. One possible explanation could be that the progenitor cells (bone or immune) involved in intramembranous osseous repair come from different sources between the maxilla and femur[8]. Further investigation via cell transplantation (maxilla osteoblast progenitors → femur defect or femur osteoblast progenitors → maxilla) could aid in understanding the cell v. environment question. The data presented in Chapter 4 showed that there is a matrix environment component to the healing process, as the osteoclast number was significantly decreased (day 7), then increased (day 14) with BAPN treatment (Figure 4.8). The maxilla did not show a significant alteration in osteoclast number (Figure 4.8). However, maxillary and femur osteoclasts are derived from different embryonic lineage (neural crest for maxilla and mesoderm for femur)[9] and the collagen cross-links are different between the bones (Figure 3.3). Therefore a cell transplant experiment for the osteoclasts would further our understanding of the role of collagen cross-links on osteoclasts between craniofacial and long bones.

6.3 LOX as a Therapeutic Target in Healing

One of the most surprising findings of Chapter 4 was the response of osteoclasts to BAPN (or loss of LOX) in the femur, but no significant osteoclast response in the maxilla. The number of osteoclasts in the femur was also ~2X that of the maxilla (Figure 4.8), which is consistent with other studies[10]. Most therapies developed to alter osteoclast response (bisphosphonates or antibody therapies such as denosumab) are developed to improve bone density in long bones by reducing osteoclast activity. These therapies have a rare, but concerning side effect of osteonecrosis of the jaw (ONJ)[4], especially following dental extraction where osteoclasts are needed to remodel bone at the extraction site. A potential solution to mitigate ONJ would be to develop a way to locally overcome systemic osteoclast suppression at sites of extraction or surgery. Since there were site-to-site differences in osteoclast number (Figure 4.8)

and no systemic affect (S2), experiments designed to test the effect of local LOX up- or down-regulation during healing could give insight into strategies to modulate a local response of osteoclasts for improved bone healing. These studies should also be performed in the presence of a bisphosphonate or denosumab (which at high doses can cause ONJ in a mouse model[11][12]), to determine the therapeutic potential of LOX mediated osteoclast response to reduce the side effects of ONJ.

6.4 Craniofacial and Long Bone Mechanical Response to BAPN

Research presented in Chapter 3 investigated the mechanical response to BAPN in newly formed bone during normal growth and identified distinctions in response between craniofacial and long bones. I found no significant difference in the Young's modulus or hardness with BAPN treatment (Table 3.3), however, only areas of new bone were compared, not new bone to existing bone. Experiments presented in Chapter 4 sought to introduce rapid bone formation via a sub-critical osseous defect healing model with perturbed bone collagen cross-links. In the sub-critical model, both the femur and maxilla heal via intramembranous ossification. The viscoelastic properties were determined for both newly formed bone in the defect and adjacent intracortical bone. The healing process caused an increase in local LOX compared to adjacent tissue in which LOX was suppressed by BAPN (Figure 4.3). LOX inhibition caused a decrease in Young's modulus in both the femoral and maxillary defects compared to adjacent bone at day 14 (Figure 4.3). Numerous specific changes to the viscoelastic spring constants are described in detail (Figure 4.6). Of particular interest for future work is the increase in the E_2 and η_2 constants in the maxilla compared to the femur (Figure 4.6). The constants could relate to mineral/collagen interaction in the bone matrix, as similar viscoelastic properties have been investigated with filler content in synthetic thermoset nanocomposites[10]. With increasing filler content (similar for modeling purposes to the mineral component of bone) the E_2 and η_2 values increase. The collagen in craniofacial bones is more highly cross-linked (Chapter 3) with mature cross-links (like a 3-D conformation of a thermoset polymer) and therefore the bone may be behaving similarly to thermoset nanocomposites.

While microCT was used to analyze bone in the defect region (Figure 4.7), the resolution is only applicable to the mineral component, but does not give indication of carbonation or

crystallinity of the mineral or changes to the ratio of mineral/collagen at the location that the nanoindentation data was collected. Changes in carbonation (1069 cm^{-1}/960 cm^{-1}) (Figure 3.5)) or crystallinity (1/FWHM 960 cm^{-1}) can alter the slippage of the mineral and collagen during loading[11]. Experiments designed to test the alteration of mineral/matrix, carbonation, and crystallinity compared to the locally extracted spring constants in a controlled way would further the understanding of the compositional regulation of viscoelastic properties of bone during health and disease.

6.5 Serum Detectible Collagen Cross-links Specificity to bone to Translate to a Minimally Invasive Indicator of Bone Quality

In Chapter 5 I sought to identify and quantify the full suite of bone collagen cross-links in serum. While the mature cross-links (pyridinolines) have been described for over 30 years, the immature cross-inks (dihydroxylysinorleucine and hydroxylysinorleucine) have never been measured in serum. Utilizing knowledge gained in Chapter 3 for application of ultra-high performance liquid chromatography with tandem mass spectrometry (LC-MS) to quantify the cross-link profile in mouse bone (Figure 3.3), I was able to modify the preparation of the serum (with protein depletion) (Figure 5.4) to allow for a full cross-link profile quantification in mouse and human serum (Figure 5.6, Table 5.2). While this work is preliminary, it is a fundamentally important step towards using serum derived collagen cross-links as a minimally invasive indicator of bone quality.

The next step in this work is to correlate the collagen cross-link profile in serum to the profile of cross-links measured in bone. Any type I collagen (not only from bone) can contain cross-links. However, the cross-link ratios are tissue specific. Monitoring the ratios (possibly in combination with a separate bone turnover marker such as serum alkaline phosphatase, tartrate-resistant acid phosphatase form 5b (TRAcP 5b) or propeptide of type I procollagen (P1NP)) may augment the utility of these widely used serum assays. Additionally, the processing of the serum required to predictably identify dihydroxylysinorleucine and hydroxylysinorleucine presented here does not allow for analysis of the peptides still covalently bound to fragments of the collagen as a product of tissue degradation.

Assays used clinically for measuring C- and N-terminal telopeptides of type I collagen (CTX and NTX, respectively) are examples of how antibodies can be raised against the whole multi-peptide fragment for translation to a clinical assay. However, the molecular mass (and variability in mass) specific to each cross-link have not been analyzed. Future work should characterize the full proteomic profile of cross-link containing type I collagen fragments in serum. There is likelihood that the mass of the remaining type 1 collagen fragments is due to enzymatic cleavage, which could help in identifying where that cross-link originated within the body (such as cathepsin K from osteoclasts or varying site specificity of the matrix metalloproteases (MMP's))[12]. Experiments could be designed to isolate these cross-link containing fragments and analyze the mass distribution dependent on the enzyme used to degrade the type 1 collagen. Additionally, experiments could be designed to answer several questions. First, what serum detectible cross-links come directly from the skeleton as a whole? This could be answered by creation of and osteoblast specific (osteocalcin Cre) driver with conditional knockout of lysyl oxidase (LOX) or lysyl hydroxylase (LH) animal and analyze the change in the serum enzymatic cross-link profile in response to perturbed collagen cross-linking from either LOX or LH. Second, how do cross-link profiles change between individual bones in the body and how do these direct measures relate to serum levels of bone cross-links? The same animals could then have each bone surveyed to determine the contribution of direct cross-links to serum cross-links. These results would likely be influenced by individual bone cross-link profiles as well as turnover rates. Third, can changes to enzymatic cross-links in a subset of bones be detected and distinguished in serum? This thesis work showed that the cross-link profiles are inherently different between the mandible and femur (Figure 3.3). Therefore, to distinguish the contribution of craniofacial (neural crest derived) bones v. long bones (mesenchyme derived), an additional cross of a neural crest driver (such as Wnt1) could be used to determine the direct contribution of craniofacial bone cross-links to the serum profile. Lastly, can organ specificity of cross-links be determined? Such specificity to other tissues (such as the heart, vasculature, lungs, etc.) could be achieved using other Cre-drivers to attribute the "off target" contribution of bone cross-links in serum, while also opening the possibility of surveying serum cross-link profiles for each organ.

6.6 Assay of Hydroxylation Status and Implications for Serum Detectable Cross-links Profiles in Additional Tissues (Systemic and Local)

It is well understood that the serum detectible collagen cross-links arise from any cross-linked collagen in the body, not specifically bone. However, due to the high turnover rate of bone, a large portion of cross-links in serum originate from bone. Additionally, subsets of cross-links are more specific to bone (including the deoxyprydinoline and the immature HLNL and DHLNL). Tissue specific cross-link profiles and maturation of the cross-links also exist. This maturation process (conversion of immature → mature cross-links) is thought to happen spontaneously, however, the hydroxylation of the mature and immature cross-links is altered with BAPN and exercise [16]. Therefore, this conversion rate could possibly be monitored via serum at a systemic level (e.g. HLNL → DPD and DHLNL → PYD, or PYD/DPD and DHLNL/HLNL) and may apply to all tissues (of which have varied initial cross-links and patterns) if the mechanism of this conversion is genetically or enzymatically controlled.

If systemic hydroxylation rates hold true, then an additional tissue that could contribute to serum cross-links is the vasculature, which has different cross-link ratios than bone. Global loss of LOX during development leads to aortic aneurysms, prenatally. Additionally, in Marfan's syndrome (mutation in fibrillin), the aortic tissues showed have adequate LOX activity and inhibition of LOX induces aortic dissection prematurely[17]. Therefore, assessing systemic LOX activity via the relative cross-link profiles could potentially serve as an early indicator of inadequate cross-linking in a variety of tissues. Furthermore, LOX could be targeted, locally or systemically, as a therapeutic to recover cross-link deficiencies in these tissues.

Lastly, BAPN could be altering additional systemic enzymatic cross-links such as histidinohydroxymerodesmosine (HHMD) and histidinohydroxylysinonorleucine (HHL) in skin, or other cross-links that have not yet been described. A differential proteomic study coupled with mass would determine the sum of cross-links altered in tissue or serum and would be more comprehensive than targeting only the cross-links described in this dissertation. A pitfall to this approach is a lack of standards for many of the cross-links. Therefore, isolation and structural characterization of any potential cross-links would be required. However, due to the harsh processing via hydrolysis that are required for degradation of the covalent bond between the

cross-link and collagen backbone, any structures left after acid hydrolysis are likely a cross-link[18]. Linking the detected masses back to a biological or mechanical function would be critical to verify the role of identified structures as verifiable collagen cross-links. The field of mass spectrometry has developed so much in the last two decades that these sorts of studies are now more accessible and could provide key information to understand the variety of roles that collagen cross-links play.

6.7 Concluding Remarks

The work presented in this thesis details the bone matrix composition differences between craniofacial and long bones during normal growth as well as in response to perturbed collagen cross-linking. These studies also provided evidence of altered healing (mechanical properties and osteoclast number) between the femur and the maxilla. Collectively, this work broadened our understanding of bone-dependent changes to mineralization, collagen cross-linking, and healing, and improves our ability to target collagen cross-linking enzymes or specific subsets of cross-links in development of new therapeutics for improving bone quality and healing. To further the clinical translation of the findings, we sought to identify the full panel of mature and immature serum detectible cross-links for the first time. Establishing the methods to identify and quantify the immature serum detectable cross-links is a critical step in applying these findings to the prediction of bone quality and assessment of disease.

6.8 References

1. Chai Y, Maxson RE. Recent advances in craniofacial morphogenesis. Developmental Dynamics. 2006;235(9):2353–75.

2. Ueki Y, Tiziani V, Santanna C, Fukai N, Maulik C, Garfinkle J, Ninomiya C, doAmaral C, Peters H, Habal M, Rhee-Morris L, Doss JB, Kreiborg S, Olsen BR, Reichenberger E. Mutations in the gene encoding c-Abl-binding protein SH3BP2 cause cherubism. Nat Genet. 2001 Jun;28(2):125–6.

3. Simonds WF, James-Newton LA, Agarwal SK, Yang B, Skarulis MC, Hendy GN, Marx SJ. Familial Isolated Hyperparathyroidism: Clinical and Genetic Characteristics of 36 Kindreds. Medicine. 2002 Jan;81(1):1–26.

4. Chang J, Hakam AE, McCauley LK. Current Understanding of the Pathophysiology of Osteonecrosis of the Jaw. Curr Osteoporos Rep. 2018 Oct 1;16(5):584–95.

5. Boskey AL, Gadaleta S, Gundberg C, Doty SB, Ducy P, Karsenty G. Fourier transform infrared microspectroscopic analysis of bones of osteocalcin-deficient mice provides insight into the function of osteocalcin. Bone. 1998 Sep 1;23(3):187–96.

6. Mubarak S, Masako N, Al-Omari FA, Keisuke H, Katsumi U. Effect of Collagen Cross-Link Deficiency on Incorporation of Grafted Bone. Dent J. 2019 May 1;7(2):1-12.

7. Mendes EM, Irie MS, Rabelo GD, Borges JS, Dechichi P, Diniz RS, Soares PBF. Effects of ionizing radiation on woven bone: influence on the osteocyte lacunar network, collagen maturation, and microarchitecture. Clin Oral Invest. 2020 Aug;24(8):2763–71.

8. Michalski MN, Zweifler LE, Sinder BP, Koh AJ, Yamashita J, Roca H, McCauley LK. Clodronate-Loaded Liposome Treatment Has Site-Specific Skeletal Effects. J Dent Res. SAGE Publications Inc; 2019 Apr 1;98(4):459–67.

9. Chaichanasakul T, Kang B, Bezouglaia O, Aghaloo TL, Tetradis S. Diverse Osteoclastogenesis of Bone Marrow From Mandible Versus Long Bone. Journal of Periodontology. 2014;85(6):829–36.

10. Michalski MN, Seydel AL, Siismets EM, Zweifler LE, Koh AJ, Sinder BP, Aguirre JI, Atabai K, Roca H, McCauley LK. Inflammatory bone loss associated with MFG-E8 deficiency is rescued by teriparatide. The FASEB Journal. 2018;32(7):3730–41.

11. Bi Y, Gao Y, Ehirchiou D, Cao C, Kikuiri T, Le A, Shi S, Zhang L. Bisphosphonates Cause Osteonecrosis of the Jaw-Like Disease in Mice. The American Journal of Pathology. 2010 Jul 1;177(1):280–90.

12. Hayano H, Kuroshima S, Sasaki M, Tamaki S, Inoue M, Ishisaki A, Sawase T. Distinct immunopathology in the early stages between different antiresorptives-related osteonecrosis of the jaw-like lesions in mice. Bone. 2020 Jun 1;135:115308.

13. Faraz MI, Besseling N a. M, Korobko AV, Picken SJ. Characterization and modeling of creep behavior of a thermoset nanocomposite. Polymer Composites. 2015;36(2):322–9.

14. Luo Q, Nakade R, Dong X, Rong Q, Wang X. Effect of mineral–collagen interfacial behavior on the microdamage progression in bone using a probabilistic cohesive finite element model. Journal of the Mechanical Behavior of Biomedical Materials. 2011 Oct 1;4(7):943–52.

15. Fini ME, Cook JR, Mohan R, Brinckerhoff CE. Regulation of Matrix Metalloproteinase Gene Expression. Parks WC, Mecham RP, editors. Matrix Metalloproteinases. 1998 Jan 1;299–356.

16. McNerny EMB, Gardinier JD, Kohn DH. Exercise increases pyridinoline cross-linking and counters the mechanical effects of concurrent lathyrogenic treatment. Bone. 2015 Dec 1;81:327–37.

17. Busnadiego O, Gorbenko Del Blanco D, González-Santamaría J, Habashi JP, Calderon JF, Sandoval P, Bedja D, Guinea-Viniegra J, Lopez-Cabrera M, Rosell-Garcia T, Snabel JM, Hanemaaijer R, Forteza A, Dietz HC, Egea G, Rodriguez-Pascual F. Elevated expression levels of lysyl oxidases protect against aortic aneurysm progression in Marfan syndrome. J Mol Cell Cardiol. 2015 Aug;85:48–57.

18. Naffa R, Holmes G, Ahn M, Harding D, Norris G. Liquid chromatography-electrospray ionization mass spectrometry for the simultaneous quantitation of collagen and elastin crosslinks. Journal of Chromatography A. 2016 Dec 23;1478:60–7.